PHYSICS OF SENSING FOR GRAPHENE SOLUTION GATED FIELD EFFECT TRANSISTORS

A Thesis
Presented to
The Academic Faculty

by

Mauricio D. Bedoya

In Partial Fulfillment
of the Requirements for the Degree
Doctor of Philosophy in the
School of Physics

Georgia Institute of Technology
December 2015

PHYSICS OF SENSING FOR GRAPHENE SOLUTION GATED FIELD EFFECT TRANSISTORS

Approved by:

Professor Jennifer Curtis, Advisor
School of Physics
Georgia Institute of Technology

Professor Elisa Riedo
School of Physics
Georgia Institute of Technology

Professor Phillip First
School of Physics
Georgia Institute of Technology

Professor Hang Lu
School of Chemical & Biomolecular Engineering
Georgia Institute of Technology

Professor Victor Breedveld
School of Chemical & Biomolecular Engineering
Georgia Institute of Technology

Date Approved: 13 November 2015

To my mother Ana Mercedes Saavedra,

my grandmother Rebeca Beltrán de Saavedra,

and my grandfather José del Carmen Saavedra

my unconditional supporters.

ACKNOWLEDGEMENTS

This work wouldn't had been possible with the cooperation, help, and support of many people including friends, family, Georgia Tech faculty, my labmates, and many other grad students. First I would like to acknowledge my advisor Jennifer Curtis for providing me an opportunity to work in her lab and for many intellectual conversations that helped me to clarify my own thoughts and the planning of my research. I also thank her for her help in the edition of this document.

I would like to give special thanks to Peter Metaxas who spent ten months as a postdoc in our lab and was permanently involved in my research intellectually and establishing a cleanroom process workflow for my samples. Without his drive it would had taken a lot longer to get my first reliable devices. I also want to acknowledge other members of my lab: Jan Scrimgeour, Vamsi Kodali, and Keith Carrol. They were available for many technical consultations and Keith helped us with some AFM experiments taking time from his time demanding research schedule. Jan Simon Toro, a MSE undergrad student, was very helpful to refine the device fabrication process for our CVD samples and also conducted several experiments. His attention to detail and his curiosity made him a very helpful assistant.

This work would also not be possible with the support of Professor Walter de Heer lab which provided most of the graphene samples for my research. I am grateful to Claire Berger for being patient with my many requests for samples and for having her office open to any question I could have about epitaxial graphene and graphene basic physics. I also have to thank Rui Dong, John Hankinson, James Palmer, Yike Hu, Jean-Phillipe Turmaud, Andrei Savu, and Yiran Hu for providing me with graphene samples and assisting me in many of my fabrication steps.

I would like to thank Professor Seth Marder for opening his lab for several needs I had during my research. I am very grateful to two members of his lab: Jassem Abdallah who gave me my initial training in spin coating and photolithography, and Siyuan Zhang

provided all the CVD samples used in this project.

Professor Hang Lu also opened her lab to assist me in my spin coating needs. I would like to thank her students Loice Chingoza and Tom Levario for their help with SU-8 processing.

Professor Jiri Janata provided us with a reference electrode through Alex Jonke. I am grateful to them for this and to Professor Janata for opening his office for intellectual discussions.

On a personal level I would like to thank my family and friends for their continuous support over all these years.

TABLE OF CONTENTS

LIST OF TABLES

LIST OF FIGURES

LIST OF SYMBOLS OR ABBREVIATIONS

8OHdG	8 hydroxyguanosine.
$\bar{n}$	Offset carrier density.
BSA	Bovine serum albumin.
BZ	Brillouin zone.
CCS	Confined controlled sublimation.
C_{DL}	Double layer capacitance.
c^{∞}	Density of ions.
CNP	Charge neutrality point.
CNT	Carbon nanotube.
CVD	Chemical vapor deposition.
D	Diffusion constant.
DFT	Density functional theory.
DI	Deionized.
DP	Dirac point.
EDL	Electrical double layer.
E_F	Fermi level.
EG	Epitaxial graphene.
ℓ	Mean free path.
FET	Field effect transistor.
FPGA	Field-programmable gate array.
G	Conductance.
GluD	Glutamate dehydrogenase.
GO	Graphene oxide.
GOD	Glucose oxidase.
GPIB	General purpose interface bus.
g_s	Spin degeneracy factor.
g_v	Valley degeneracy factor.

I_g	Leakage current.
IgE	Immunoglobulin E.
IgG	Immunoglobulin G.
IHP	Inner Helmholtz plane.
IS	Ionic sensing.
KCl	Potassium chloride.
λ_D	Debye length.
MCP	Minimum conductance point.
MEG	Multilayer epitaxial graphene.
MOSFET	Metal-oxide-semiconductor field effect transistor.
n	Density of carriers.
n^*	Residual carrier density.
N_A	Avogadro constant.
n_{imp}	Surface density of impurities.
n^∞	Density of particles.
ν	Density of states.
OHP	Outer Helmholtz plane.
PDMS	Polydimethylsiloxane.
PSA	Prostate specific antigen.
RIE	Reactive ion etching.
RPA	Rotating phase approximation.
r_s	Wigner-Seitz radius.
SCA	Surface charge approximation.
SGFET	Solution gated field effect transistor.
σ	Conductivity.
σ_d	Surface density of charge.
σ_{max}	Surface density of ionizable groups.
σ_{offset}	Surface density of permanently charged groups.
SLG	Single layer graphene.

τ	Mean free time.
v_F	Fermi velocity.
V_g	Gate voltage.

SUMMARY

Graphene is a promising material for chemical sensing applications. It has the largest possible surface area per volume which maximizes the sensitivity of its physical properties to environmental effects, it is biocompatible, and it is possible to use standard fabrication techniques to make devices in a commercial scale. Although many studies have focused on incorporating graphene into sensors, in particular into SGFETs, deeper understanding of how graphene conductivity responds to ionic solutions and charged molecules is necessary in order to engineer an optimized sensor. The purpose of this work is to clarify the physics governing the surface interaction of graphene in SGFETs with ions and charged molecules. With a clearer understanding of how these interactions register in the conductivity of graphene, it then may be possible to design the ultrasensitive sensors that are often predicted to be possible when using graphene.

Epitaxial graphene (EG) and graphene produced by chemical vapor deposition (CVD) were used to fabricate SGFETs that were tested under different ionic strength conditions and under different concentrations of charged proteins. First, we performed a detailed characterization of the performance of graphene SGFETs including reproducibility, reversibility, and device-to-device consistency for ionic strength sensing. To get a clearer picture of the electrostatic gating effect in ionic solutions, we analyzed our data combining two models: the electrical double layer model, which accounts for the distribution of ions inside the solution, and a chemical ionization model that accounts for ionizable groups on the graphene surface. The simultaneous solution of the two models gives us quantitative information about the surface charge ionization under different salt concentrations. This gave us an insight into the influence of charged groups fixed to the surface on the gating effect which is fundamental to the performance of SGFETs as sensors.

Using our experimental data we were able to estimate the density of charged impurities in two carrier density regimes. For high densities, we found a correlation between our

estimated impurities and the surface charge that suggests that the ionizable groups act as impurities. For small carrier densities, we modeled the carriers for the first time using a self-consistent approximation (SCA) that also gives an estimation for the charged impurities. These impurities are uncorrelated to the surface charge. This suggests that the impurities estimated from the SCA model are not related to the ionizable groups and the origin of the conductivity for small density is due to the permanently charged impurities only. The analysis of the conductance data in the two regimes of carrier density provided a first systematic insight into how the charged impurities –permanent and variable– influence the electrical conductivity of SGFETs.

We also performed experiments of charged protein adsorption to graphene to study the role of these molecules as dopants. Our estimation of the charged impurities for the protein experiments showed a relation between the estimated values and the protein concentration. This confirms that the proteins interact with the graphene as charged impurities. Our experiments with ionic strength and charged proteins allowed us to gain fundamental understanding of the interaction of charged particles with graphene. The analysis performed in this work gives a guide for the development of graphene SGFETs sensors by engineering the impurities at the surface to optimize the sensitivity. The design of receptors for specific sensing that do not require charged targets is possible with engineering the charge that the receptor presents to graphene when the analyte concentration changes.

CHAPTER I

INTRODUCTION

Graphene is a two-dimensional one-atom thick hexagonal crystal with extraordinary properties that are interesting for fundamental science studies and engineering applications. In 2003 graphene was produced for the first time [7, 57] and immediately recognized as a very promising material. Graphene's properties had been studied theoretically several decades before its initial standalone production. In particular Wallace [73] established its band structure discovering that its electrons behave as massless Dirac fermions. This makes graphene an interesting material from the point of view of fundamental physics. In particular, it can be used as a platform to study quantum electrodynamics in a tabletop [36, 25].

Some properties that make graphene an interesting material from the point of view of engineering are its high carrier mobility [9], high heat conductivity [76], and the highest strength ever measured [44]. Graphene is also a promising material in sensing and biosensing applications for several reasons. It has the highest surface to volume ratio possible maximizing its exposure to the environment, standard electronic device fabrication techniques are available to make graphene devices, it is biocompatible, and it is flexible. Besides these properties, graphene is an aromatic molecule and it is possible to use aromatic molecular linking molecules to fix proteins, DNA molecules, aptamers, antibodies, and other bioreceptors to graphene making it sensitive to the presence of biochemical agents without changing its electrical properties [40].

There is a need for biosensors for biomedical and environmental applications and electrical based sensors are a viable option for the development of portable, low-cost, real-time devices. In contrast, optical biosensors -based in chemical labeling or label-free- can be extremely sensitive (down to zepto-molar concentrations for some biomolecules [54, 27]) but they require additional optical instrumentation and other components that raise the cost of the device [60]. In the case of fluorescence-based sensors an additional preparation of

the sample is required. Detection limits of biomolecules for current electronic sensors based on carbon nanotubes (CNTs) are in the range $[100\text{pM}, 5\text{mM}]$ depending on the setup and target molecule [41, 15]. CNTs have similar properties to graphene and they were explored as sensing materials before graphene was initially produced. But controlled fabrication of CNTs is currently not possible and so production of sensors based on them is not scalable. Similar detection limits have been reported for graphene [41] (and Appendix B). The lower limit reported is 1pM for DNA detection by [16]. The dynamic range is very variable among reported results. Ranges between two and seven orders of magnitude have been shown for graphene from different fabrication sources (see Appendix B). A clear understanding of the electronic detection mechanism of graphene can give the insight needed to achieve lower detections limits as those already met by optical sensors.

In this work epitaxial graphene (EG) and graphene made with chemical vapor deposition (CVD) are used to make solution-gated field effect transistors (SGFETs) that can be used in liquid solutions to measure the concentration of chemical analytes. The goal of this thesis is to achieve a better physical understanding of graphene SGFETs as sensors in liquid environments. To understand chemical and physical mechanisms of detection in liquids we performed two types of experiments and interpreted them coupling several complementary conceptual models. We present results for the electrical response of SGFETs to ionic strength (IS) change in ionic solutions and also the response to protein adsorption. The experimental results obtained can be understood starting from the basic electrical conductivity model that accounts for the conductivity change under different gating conditions and the doping effect of adsorbed ions. To understand the liquid gating effect in ionic solutions two models are needed. An electrostatic double layer model for the ions inside the liquid and a model that considers the ionizable sites at the graphene surface. These models are put together to calculate the surface charges under different IS conditions.

For the devices studied in this work the conductance is primarily dependent on the concentration of charged impurities. So it is possible to extract information about the impurities from our experimental results. We did estimations for the impurities of our samples using two different theoretical results. One of these estimation methods uses the

data for high carrier density in the device. The second method uses the data for small carrier density. Then we compared these estimates to the surface charges calculated using the electrical double layer model and the surface ionization model. There is some agreement between the impurities obtained using the first method and the surface charges obtained from the gating models. The impurities estimated using the second method disagree with the other two calculations and they require further study. The response of the devices to non-specific protein adsorption is also explored. The proteins adsorbed are charged affecting the doping of the graphene channel.

Chapter 2 reviews some background concepts about graphene: band structure calculations, graphene fabrication methods, SGFETs, and conductivity theory for graphene FETs. In Chapter 3 the SGFETs fabrication and experimental methods are described. Next in Chapter 4 results of ionic sensing (IS) experiments are presented in the context of electrostatic gating. In Chapter 5 an analysis of the surface charge in graphene and its relation with impurities is presented. In Chapter 6 experiments with nonspecific sensing of biomolecules are discussed. Finally in Chapter 7 the conclusions and future perspectives of this work are presented.

CHAPTER II

BASIC GRAPHENE CONCEPTS

In this chapter an overview of graphene structure, basic band structure calculations, and the conductivity coming from its energy structure is provided in Section 2.1. In Section 2.2 the fabrication methods for graphene are described. Then, the concept of a graphene SGFET is introduced in Section 2.3. Finally, a more detailed theoretical calculation of the conductivity for a graphene FET is presented in Section 2.4.

2.1 Electronic Properties of Graphene

In 1947 Wallace [73] derived for the first time the band structure of graphene. The band structure calculation shown here is based on [64] and uses current mathematical notation. This calculation starts considering the 2D crystal structure of graphene as discussed in Section 2.1.1. It follows with the nearest-neighbors tight binding approximation for the calculation of the energy structure as shown in Section 2.1.2. After that, an extension of the calculation to bilayer graphene is outlined in Section 2.1.3. This last calculation is only shown for completeness as for our experiments the graphene properties correspond to those of single layer graphene (see Section 2.2.4). Finally the conductivity expected for this band structure is shown in Section 2.1.4 based on calculations detailed in Section 2.4.

2.1.1 Graphene Lattices

Graphene is a sheet of carbon atoms forming an hexagonal 2D honeycomb structure. Its real space crystal structure can be described using a unit cell with two atoms usually labeled A and B (Figure 2.1). All atoms of type A (or B) form a sublattice named A (or B) and any atom in the A sublattice is located in a position $\mathbf{R} = n_1\mathbf{a_1} + n_2\mathbf{a_2}$. Atoms in the B sublattice are found a distance $a_{cc} = 1.42$Å to the top of the A atoms in the orientation we use for this derivation.

The unit lattice vectors $\mathbf{a_1}$ and $\mathbf{a_2}$ are written as

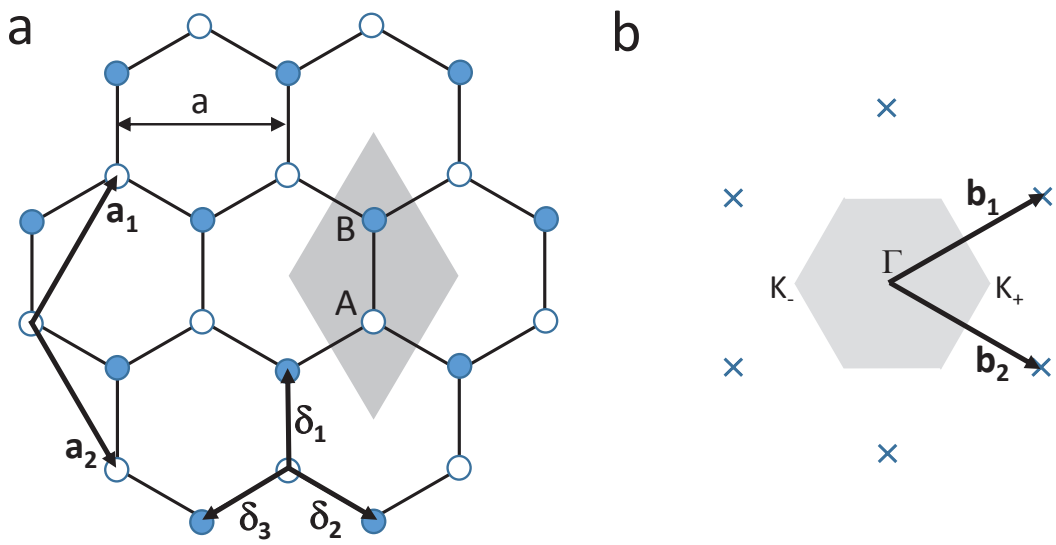

Figure 2.1: (a) Real space structure of graphene (b) Reciprocal lattice with important points labeled

$$\mathbf{a_1} = \frac{a}{2}(\sqrt{3}, 1) \text{ and } \mathbf{a_2} = \frac{a}{2}(\sqrt{3}, -1)$$

where $a = 2.46$Å is the lattice constant. The corresponding unit lattice vectors ($\mathbf{b_1}$, $\mathbf{b_2}$) with $\mathbf{a_1} \cdot \mathbf{b_1} = \mathbf{a_2} \cdot \mathbf{b_2} = 2\pi$ and $\mathbf{a_1} \cdot \mathbf{b_2} = \mathbf{a_2} \cdot \mathbf{b_1} = 0$ in the reciprocal space are (see Figure 2.1(b))

$$\mathbf{b_1} = \frac{2\pi}{a}(\frac{1}{\sqrt{3}}, 1) \text{ and } \mathbf{b_2} = \frac{2\pi}{a}(\frac{1}{\sqrt{3}}, -1).$$

Each carbon atom in the ground state has the electronic configuration $1s^2 2s^2 2p^2$. To maximize the number of bonds that each atom can form it assumes the excited configuration $1s^2 2s^1 2p^3$. In this configuration the four valence electrons occupy the orbitals $2s, 2p_x, 2p_y$, and $2p_z$. The first three are hybridized in a sp^2 configuration and they form σ bonds with their three nearest atoms. So there is an electron per atom in the $2p_z$ orbital (also called a π electron because it can form π bonds). These π electrons are responsible for the electronic properties of graphene at low energies.

As it is shown in Figure 2.1(b) the first Brillouin zone (BZ) is hexagonal. There are two points in the BZ, K_+ and K_-, that we will find to be important in the description of graphene electronic properties and they are called Dirac Points. Their positions are given by

$$K_\pm = \pm(\frac{4\pi}{3a}, 0)$$

2.1.2 Tight Binding Calculation

Before proceeding to the band structure calculation of monolayer graphene a quick review of the tight binding model will be helpful. This method will be immediately applied to the energy structure calculation of graphene.

2.1.2.1 The Tight Binding general model

In the general case there are n atomic orbitals ϕ_j $(j = 1, ..., n)$ in the unit cell and so there are n Bloch functions that depend on the position $\mathbf{r}$ and the wave vector $\mathbf{k}$,

$$\Phi_j(\mathbf{k}, \mathbf{r}) = \frac{1}{\sqrt{N}} \sum_{i=1}^{N} e^{i\mathbf{k}\cdot\mathbf{R}_{j,i}} \phi_j(\mathbf{r} - \mathbf{R}_{j,i}) \tag{2.1}$$

where N is the number of unit cells and $\mathbf{R_{j,i}}$ is the position of the jth orbital in the ith unit cell. An electronic wave function is a superposition of the Bloch functions,

$$\psi_j(\mathbf{k}, \mathbf{r}) = \sum_{l=1}^{n} c_{jl}(\mathbf{k}) \Phi_l(\mathbf{k}, \mathbf{r}) \tag{2.2}$$

where c_{jl} are coefficients to be found. The energy $E_j(\mathbf{k})$ of the j band is,

$$E_j(\mathbf{k}) = \frac{\langle \psi_j | \mathcal{H} | \psi_j \rangle}{\langle \psi_j | \psi_j \rangle} \tag{2.3}$$

where $\mathcal{H}$ is the Hamiltonian. Substituting the expansion of the wavefunction (Equation (2.2)) into the energy (Equation (2.3)) gives

$$E_j(\mathbf{k}) = \frac{\sum_{i=1,l=1}^{n} H_{il} c_{ji}^* c_{jl}}{\sum_{i=1,l=1}^{n} S_{il} c_{ji}^* c_{jl}} \tag{2.4}$$

where the transfer matrix H_{il} and the overlap matrix S_{il} are defined as

$$H_{il} = \langle \Phi_i | \mathcal{H} | \Phi_l \rangle, S_{il} = \langle \Phi_i | \Phi_l \rangle \tag{2.5}$$

Minimizing the energy E_j with respect to the coefficients c_{jm}^* requires setting $\partial E_j / \partial c_{jm}^* = 0$. After some straightforward algebra we obtain,

$$\sum_{l=1}^{n} H_{ml} c_{jl} = E_j \sum_{l=1}^{n} S_{ml} c_{jl}. \tag{2.6}$$

These equations can be written as matrix equations,

$$H\psi_j = E_j S \psi_j \tag{2.7}$$

where H, S, and ψ_j are defined by,

$$H = \begin{pmatrix} H_{11} & H_{12} & \cdots & H_{1n} \\ H_{21} & H_{22} & \cdots & H_{2n} \\ \vdots & \vdots & \ddots & \vdots \\ H_{m1} & H_{m2} & \cdots & H_{mn} \end{pmatrix}, S = \begin{pmatrix} S_{11} & S_{12} & \cdots & S_{1n} \\ S_{21} & S_{22} & \cdots & S_{2n} \\ \vdots & \vdots & \ddots & \vdots \\ S_{m1} & S_{m2} & \cdots & S_{mn} \end{pmatrix}, \psi_j = \begin{pmatrix} \psi_{j1} \\ \psi_{j2} \\ \vdots \\ \psi_{jn} \end{pmatrix} \tag{2.8}$$

Finally, the energies E_j can be found by solving the secular equation,

$$\det(H - E_j S) = 0 \tag{2.9}$$

2.1.2.2 Application to Graphene

For the case of monolayer graphene we have two atoms A and B per unit cell and each one has a $2p_z$ orbital. To have a more descriptive notation we choose $j = A$ and $j = B$ for these orbitals. Now we can build the transfer H and the overlap S matrices.

The diagonal H_{AA} matrix element can be obtained substituting the Bloch Equation (2.1) into Equation (2.5),

$$H_{AA} = \frac{1}{N} \sum_{i=1}^{N} \sum_{j=1}^{N} e^{i\mathbf{k}\cdot(\mathbf{R}_{A,j} - \mathbf{R}_{A,i})} \langle \phi_A(\mathbf{r} - \mathbf{R}_{A,i}) | \mathcal{H} | \phi_A(\mathbf{r} - \mathbf{R}_{A,j}) \rangle \tag{2.10}$$

where $\mathbf{k} = (k_x, k_y)$ is in the graphene reciprocal space plane. Next we assume that the main contribution to H_{AA} comes from the same site ($i = j$ term),

$$H_{AA} \approx \frac{1}{N} \sum_{i=1}^{N} \langle \phi_A(\mathbf{r} - \mathbf{R}_{A,i}) | \mathcal{H} | \phi_A(\mathbf{r} - \mathbf{R}_{A,i}) \rangle. \tag{2.11}$$

Note that the matrix element $\langle \phi_A | \mathcal{H} | \phi_A \rangle$ is independent of the site index i in the summation. We set it equal to a parameter,

$$\epsilon_{2p} = \langle \phi_A(\mathbf{r} - \mathbf{R}_{A,i}) | \mathcal{H} | \phi_A(\mathbf{r} - \mathbf{R}_{A,i}) \rangle \tag{2.12}$$

that corresponds to the energy of the $2p_z$ orbital. The sublattice B has the same structure as A so the matrix element for its diagonal component has the same value as H_{AA}.

$$H_{BB} = H_{AA} \approx \epsilon_{2p}. \tag{2.13}$$

The calculation for the diagonal elements of the overlap matrix S goes the same way. In this case an overlap integral between the orbital $2p_z$ on the same atom is equal to unity,

$$\langle \phi_A(\mathbf{r} - \mathbf{R}_{A,i}) | \phi_A(\mathbf{r} - \mathbf{R}_{A,i}) \rangle = 1. \tag{2.14}$$

And assuming this contribution dominates it can be shown that,

$$S_{BB} = S_{AA} = 1. \tag{2.15}$$

The off diagonal H_{AB} matrix element can be obtained the same way as H_{AA}, H_{BB} substituting the Bloch Equation (2.1) into Equation (2.5),

$$H_{AB} = \frac{1}{N} \sum_{i=1}^{N} \sum_{j=1}^{N} e^{i\mathbf{k}\cdot(\mathbf{R}_{B,j} - \mathbf{R}_{A,i})} \langle \phi_A(\mathbf{r} - \mathbf{R}_{A,i}) | \mathcal{H} | \phi_B(\mathbf{r} - \mathbf{R}_{B,j}) \rangle. \tag{2.16}$$

This element describes hopping between sites in the sublattices A and B and it contains all the elements of each lattice. As in the case of the diagonal elements it can be assumed that the dominant terms in the double sum are the hopping terms between nearest-neighbors. Focusing on the lattice A,

$$H_{AB} \approx \frac{1}{N} \sum_{i=1}^{N} \sum_{l=1}^{3} e^{i\mathbf{k}\cdot(\mathbf{R}_{B,l} - \mathbf{R}_{A,i})} \langle \phi_A(\mathbf{r} - \mathbf{R}_{A,i}) | \mathcal{H} | \phi_B(\mathbf{r} - \mathbf{R}_{B,l}) \rangle. \tag{2.17}$$

The matrix element between neighboring atoms $\langle \phi_A | \mathcal{H} | \phi_B \rangle$ is independent of the indices i and l and can be written as a parameter t. Since $t < 0$ it is customary to define a positive parameter $\gamma_0 = -t$, where

$$\gamma_0 = -\langle \phi_A(\mathbf{r} - \mathbf{R}_{A,i}) | \mathcal{H} | \phi_B(\mathbf{r} - \mathbf{R}_{B,l}) \rangle. \tag{2.18}$$

Using this expression we can find a compact expression for H_{AB},

$$H_{AB} \approx -\gamma_0 f(\mathbf{k}) \tag{2.19}$$

where,

$$f(\mathbf{k}) = \sum_{l=1}^{3} e^{i\mathbf{k}.\boldsymbol{\delta}_l} \tag{2.20}$$

and the relative position vector of atom B_l to atom A_i is denoted as $\boldsymbol{\delta}_l = \mathbf{R}_{B,l} - \mathbf{R}_{A,i}$. As can be seen in Figure 2.1 the three relative vectors are,

$$\boldsymbol{\delta}_1 = \left(0, \frac{a}{\sqrt{3}}\right), \boldsymbol{\delta}_2 = \left(\frac{a}{2}, -\frac{a}{2\sqrt{3}}\right), \boldsymbol{\delta}_3 = \left(-\frac{a}{2}, -\frac{a}{2\sqrt{3}}\right). \tag{2.21}$$

The other off-diagonal element H_{BA} is the complex conjugate of H_{AB}:

$$H_{BA} \approx -\gamma_0 f^*(\mathbf{k}). \tag{2.22}$$

A very similar calculation gives the off-diagonal elements of the overlap matrix,

$$S_{AB} \approx s_0 f(\mathbf{k}), S_{BA} \approx s_0 f^*(\mathbf{k}) \tag{2.23}$$

where $s_0 = \langle \phi_A(\mathbf{r} - \mathbf{R}_{A,i}) | \phi_B(\mathbf{r} - \mathbf{R}_{B,l}) \rangle$ is the overlap integral between orbitals in adjacent atoms.

Putting all the terms for the transfer and overlap matrices together we obtain,

$$H_1 = \begin{pmatrix} \epsilon_{2p} & -\gamma_0 f(\mathbf{k}) \\ -\gamma_0 f^*(\mathbf{k}) & \epsilon_{2p} \end{pmatrix}, S_1 = \begin{pmatrix} 1 & s_0 f(\mathbf{k}) \\ s_0 f^*(\mathbf{k}) & 1 \end{pmatrix}. \tag{2.24}$$

With them the energy E can be determined solving the secular equation $\det(H_1 - E S_1) = 0$ which gives two bands $E_\pm$

$$E_\pm = \frac{\epsilon_{2p} \pm \gamma_0 |f(\mathbf{k})|}{1 \mp s_0 |f(\mathbf{k})|}. \tag{2.25}$$

Two views of the energy landscape in the reciprocal space can be seen in Figures 2.2 and 2.3. The parameter values for these plots are $\gamma_0 = 3.033eV$, $s_0 = 0.129$, and $\epsilon_{2p} = 0$. These values cannot be determined by tight binding. Usually they can be found using density functional theory (DFT) or by experimental fitting. Some observations can be made on these plots:

- The Fermi level is located at $E = 0$.
- There is no band gap: the valence and conductance bands touch at six points in the edge of the BZ.
- You can group these points in two different groups. One point from each group (labeled $\mathbf{K}_\xi$, where $\xi = \pm 1$) is picked in order to analyze the band structure around them, these are usually called Dirac points (DP).
- On the other hand the bands have their wider separation at the Γ point.

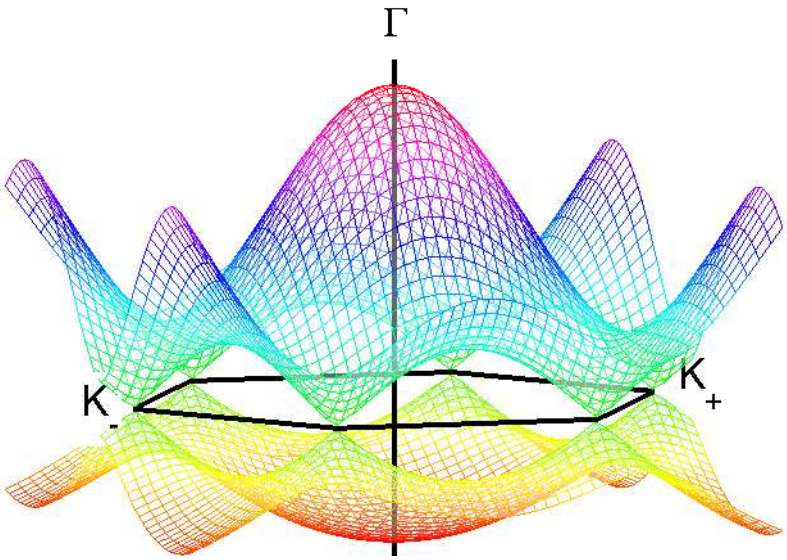

Figure 2.2: Energy bands for monolayer graphene

The electronic properties of graphene can be described focusing on the physics around the Dirac points. For our calculations we will use (see Figure 2.1(b)),

$$\mathbf{K}_\xi = \xi\left(\frac{4\pi}{3a}, 0\right), \xi = \pm 1. \tag{2.26}$$

At $\mathbf{k} = \mathbf{K}_\xi$, the coupling factor $f(\mathbf{k}) = 0$ and there is no interaction between the sublattices A and B. This factor can be approximated linearly around the Dirac points using a momentum vector relative to them. The momentum $\mathbf{p} = (p_x, p_y)$ measured from the center of $\mathbf{K}_\xi$ is,

$$\mathbf{p} = \hbar\mathbf{k} - \hbar\mathbf{K}_\xi. \tag{2.27}$$

The first order expansion of the coupling factor around $\mathbf{p}$ is,

$$f(\mathbf{k}) \approx -\frac{\sqrt{3}a}{2\hbar}\left(\xi p_x - i p_y\right). \tag{2.28}$$

Inserting this expression inside Equation (2.24) and using $\epsilon_{2p} = 0$ the transfer matrix around the $\mathbf{K}_\xi$ points is,

$$H_{1,\xi} = v_F \begin{pmatrix} 0 & \xi p_x - i p_y \\ \xi p_x + i p_y & 0 \end{pmatrix}, v_F = \frac{3a\gamma_0}{2\hbar} \tag{2.29}$$

where v_F is a parameter called the Fermi velocity and $v_F \approx 1.7 \times 10^6 m/s$ for the parameters given above. In general $v_F \sim 10^6 m/s$ for the parameters found in the literature. The overlap

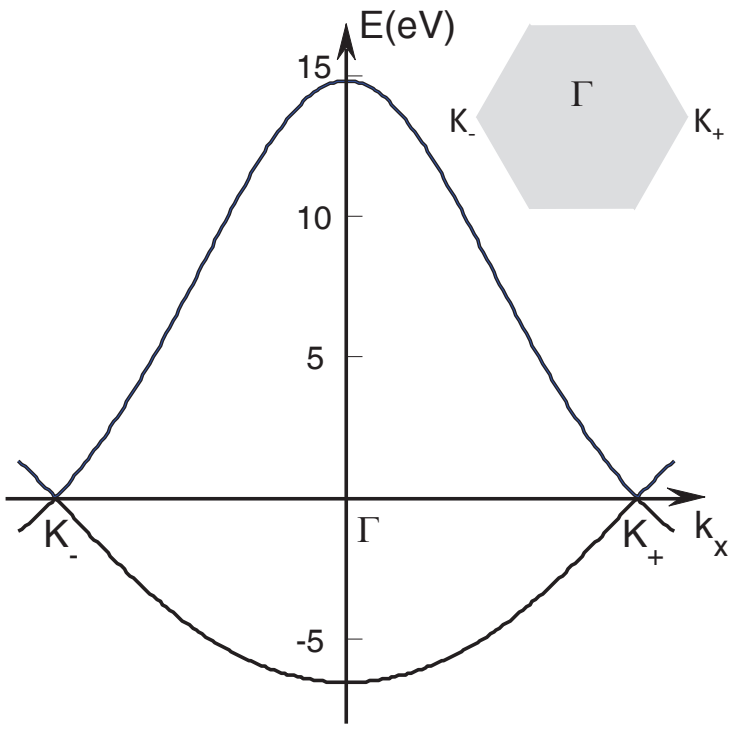

Figure 2.3: Energy bands along the k_x axis for monolayer graphene

matrix contribution to the energy bands is quadratic and so it is the 2-dimensional identity to the first order. After these approximations Equation (2.7) becomes $H_1\psi_j = E\psi_j$, where $H_1 \approx H_{1,\xi}$ is the effective Hamiltonian and can be written as,

$$H_{1,\xi} = v_F\left(\xi\sigma_x p_x + \sigma_y p_y\right) \tag{2.30}$$

where σ_x and σ_y are two of the Pauli matrices. This equation is usually expressed in the form of the massless Dirac equation for $\xi = +1$,

$$H_{1,\xi} = v_F\boldsymbol{\sigma}\cdot\mathbf{p} \tag{2.31}$$

where $\boldsymbol{\sigma} = (\sigma_x, \sigma_y)$ is a compact notation for the Pauli matrices. Finally, the eigenvalues and eigenvectors for the effective Hamiltonian around the Dirac points can be found,

$$E_\pm = \pm v_F p, \psi_\pm = \begin{pmatrix} 1 \\ \pm\xi e^{i\xi\varphi} \end{pmatrix} e^{i\mathbf{p}\cdot\mathbf{r}/\hbar} \tag{2.32}$$

where φ is the polar angle of the relative momentum $\mathbf{p}$ in the graphene plane, $\mathbf{p} = p(\cos(\varphi), \sin(\varphi))$

2.1.3 Bilayer Graphene

To make the energy band structure calculations for bilayer graphene many of the expressions and ideas introduced for monolayer graphene can be reused. For this calculation the so called Bernal or AB stacking will be considered. In this case two graphene monolayers are arranged parallel to each other with a separation $d \approx 2.4a = 0.34nm$ between them. The two layers are oriented in the same direction so the lattice vectors $\mathbf{a}_1$, $\mathbf{a}_2$, and the lattice constant a are the same of the monolayer case.

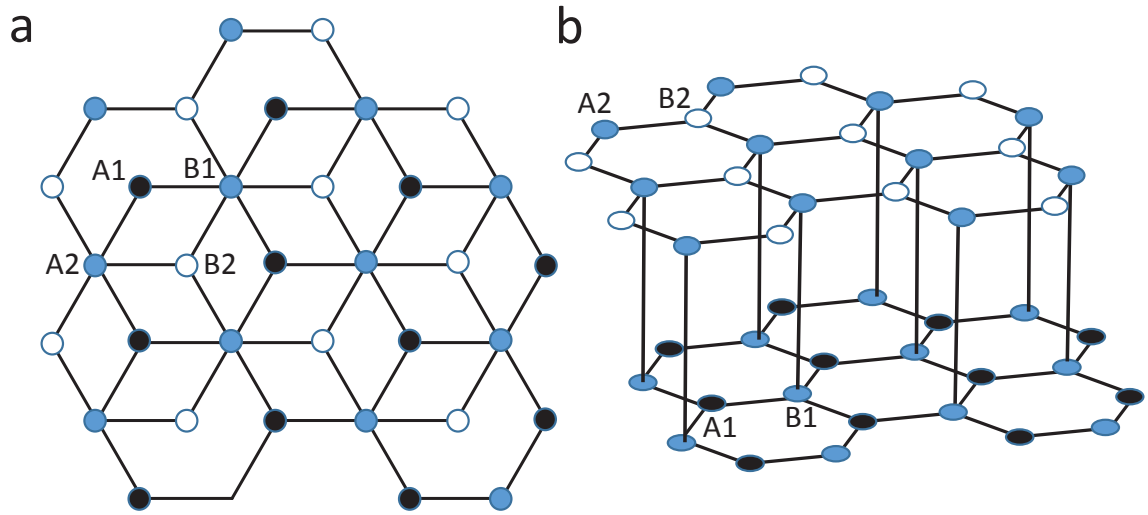

Figure 2.4: (a) Real space structure of Bernal-stacked bilayer graphene (top view) (b) Real space structure of Bernal-stacked bilayer graphene (lateral view)

The A and B sublattice atoms for the lower (upper) sheet are labeled A1,B1 (A2,B2) (see Figure 2.4). In Bernal-stacking the B1 atoms are just below the A2 ones and the nearest neighbor interlayer coupling between them is,

$$\gamma_1 = \langle \phi_{A2}(\mathbf{r} - \mathbf{R}_{A2}) | \mathcal{H} | \phi_{B1}(\mathbf{r} - \mathbf{R}_{B1}) \rangle. \tag{2.33}$$

All other overlap terms between layers are ignored in a first approximation. So the transfer and overlap matrices for the bilayer graphene considering orbitals at (A1,A2,B1,B2)

take the form,

$$H = \begin{pmatrix} \epsilon_{2p} & -\gamma_0 f(\mathbf{k}) & 0 & 0 \\ -\gamma_0 f^*(\mathbf{k}) & \epsilon_{2p} & \gamma_1 & 0 \\ 0 & \gamma_1 & \epsilon_{2p} & -\gamma_0 f(\mathbf{k}) \\ 0 & 0 & -\gamma_0 f^*(\mathbf{k}) & \epsilon_{2p} \end{pmatrix} \tag{2.34}$$

$$S = \begin{pmatrix} 1 & s_0 f(\mathbf{k}) & 0 & 0 \\ s_0 f^*(\mathbf{k}) & 1 & 0 & 0 \\ 0 & 0 & 1 & s_0 f(\mathbf{k}) \\ 0 & 0 & s_0 f^*(\mathbf{k}) & 1 \end{pmatrix} \tag{2.35}$$

.

Solving for the energies along the k_x axis four bands are obtained (Figure 2.5). Two of them touch each other at the DP and there other two are very similar to the previous ones but with a gap between them corresponding to bonding and antibonding of the orbitals for A2,B1.

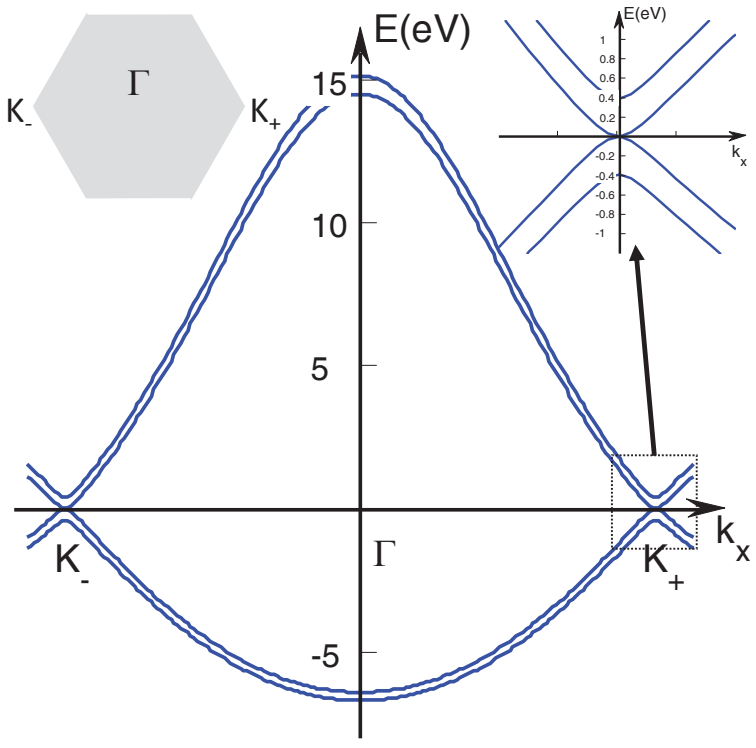

Figure 2.5: Energy band structure for bilayer graphene along the k_x axis

When an approximate value $\gamma_0|f(\mathbf{k})| \approx v_F p$ is used for the intralattice constant around the DP the following expression for the energies is obtained,

$$E_{\pm}^{(-1)} \approx \pm\frac{\gamma_1}{2}\left(\sqrt{1+\frac{4v_F^2p^2}{\gamma_1^2}}-1\right). \tag{2.36}$$

This formula predicts a linear dispersion for large momenta ($\gamma_1 \ll v_F p \ll \gamma_0$) and a quadratic dispersion $E_{\pm}^{(-1)} \approx \pm\frac{v_F^2p^2}{\gamma_1}$ near the DP. Assuming $|E| \ll |\gamma_1|$ and $|\gamma_0 f(\mathbf{k})| \ll |\gamma_1|$ the transfer matrix H (equation 2.34) can be transformed to a two level effective Hamiltonian similar to the one obtained for monolayer graphene,

$$H_{2,\xi} = -\frac{1}{2m}\begin{pmatrix} 0 & (\xi p_x - ip_y)^2 \\ (\xi p_x + ip_y)^2 & 0 \end{pmatrix}, v_F = \frac{3a\gamma_0}{2\hbar}, m = \frac{\gamma_1}{2v_F^2} \tag{2.37}$$

m is the effective mass and $m \approx 0.0119m_e$, where m_e is the electron mass. The effective Hamiltonian can be easily solved obtaining,

$$E_{\pm} = \pm\frac{p^2}{2m}, \psi_{\pm} = \frac{1}{\sqrt{2}}\begin{pmatrix} 1 \\ \mp e^{i2\xi\varphi} \end{pmatrix} e^{i\mathbf{p}\cdot\mathbf{r}/\hbar}. \tag{2.38}$$

These results can be summarized the following way,

- The conduction and the valence bands touch each other at the DP as in the case of monolayer graphene.
- But the dispersion relation is quadratic instead of linear close to the $\mathbf{K}_\xi$ points.
- Other two states, usually labeled as "dimers", appear below and above the usual ones for the monolayer graphene.
- There is a bandgap between the "dimers" equal to twice γ_1 the interaction parameter between nearest neighbors in adjacent planes.

2.1.4 Conductivity in Graphene

The origin of conductivity in graphene for present experiments can be explained by a model discussed by Adam [1] that assumes that the conductivity in graphene is dominated by long-range Coulomb scatterers (charged impurities) rather than by short-range scattering due

to dislocations in the structure. The results obtained by this assumption are in agreement with the experimental literature [1, 12, 71]. The model is based on a semiclassical approach where the transport between scattering events is treated classically as a diffusive process and the scattering events are assumed to be quantum mechanical (where for weak-disorder a Born approximation is used).

The conductivity can be expressed by the Einstein relation $\sigma = e^2\nu(E_F)D$, where the density of states at the Fermi energy is $\nu(E_F) = g_v g_s|E_F|/(2\pi\hbar^2 v_F^2)$, and $D = v_F^2/2$ is the diffusion constant in 2D. So from classical considerations the conductivity is,

$$\sigma = \frac{g_s g_v e^2}{2h} E_F \tau = \frac{g_s g_v e^2}{2h} k_F \ell \tag{2.39}$$

where $g_s = 2$ is the spin degeneracy factor and $g_v = 2$ is the valley ($\mathbf{K}_\xi$) degeneracy. To complete the picture we remember that $\ell = v_F\tau$ is the mean free path and v_F the Fermi velocity. The scattering time τ is calculated quantum mechanically with using a random phase approximation (RPA)-Boltzmann formalism detailed in Section 2.4. Two other parameters are considered for this calculation: the density of impurities n_{imp} that is the number of impurities per unit area, and the the residual carrier density n^* that represents the carriers present when the carriers induced by the gate voltage are zero. For a discussion of the origin of n^* see Section 2.4.

The calculation of the conductivity results can be summarized by the following expression,

$$\sigma(n - \bar{n}) = \begin{cases} \frac{Ce^2 n^*}{h n_{imp}} & \text{if } n - \bar{n} < n^* \\ \frac{Ce^2 n}{h n_{imp}} & \text{if } n - \bar{n} > n^* \end{cases} \tag{2.40}$$

where n is the density of carriers and $\bar{n} = n_{imp}^2/(4n^*)$ accounts for the impurity induced shift in voltage (see Section 2.4). For graphene on SiO_2 the C constant is 20. For epitaxial graphene on SiC the C constant is 25 (see Section 2.4.2 for details about the calculation of C).

The result in Equation (2.40) can be summarized by the following statements: Cleaner samples have

- higher conductivity (mobility)

- narrower minimum plateaus in the conductivity
- smaller Dirac point change
- larger minimum conductivities

2.2 Graphene Fabrication Methods

This section presents an overview of the fabrication processes used to produce graphene. The methods included in this review are: mechanical exfoliation, liquid phase exfoliation, graphite oxidation, electric arc, epitaxial growth on a metal surface, chemical vapor deposition (CVD), and thermal decomposition of SiC (which also produces epitaxial graphene). Graphene produced by CVD and thermal decomposition was used in this work so they will be explained with more detail. Each production method has its own advantages and drawbacks and the resulting graphene's physical characteristics have an imprint of the fabrication method used. CVD and epitaxial graphene are the two preferred methods for its production as they allow large scale fabrication.

2.2.1 Graphene From Graphite: Exfoliation Methods

Some of the first graphene sheets reported in the literature were separated from graphite trough mechanical exfoliation using adhesive tape or rubbing it against a solid surface [57, 58]. The latter process is similar to writing with a pencil over a piece of paper. Both processes give graphene samples of one or multiple layers that can be identified using an optical microscope when the samples are transfered to a Si wafer with a SiO_2 layer. Curiously this identification is highly sensitive to the SiO_2 layer thickness and purity making initial identification attempts before the advent of other identification methods a matter of luck. The graphene flakes obtained by this method are about 10μm in width and 100μm in length. Because of the unpredictability of the shape and location of the final graphene sheets this method is limited in scope to experimental studies.

Another exfoliation method available for the production of graphene is liquid phase exfoliation. This process uses surface-active organic liquids that can access the interlayer space in crystalline graphite reducing the interaction energy keeping them together [30].

Then mechanical action, like ultrasonication or centrifugation, is used to separate flakes of single or few layers. These flakes and then filtered out. This method has the limitations of mechanical exfoliation and so it is unsuitable for large scale fabrication.

When graphite is exposed to chemical oxidizers the oxidized inner layers have a decreased interaction energy [68, 45]. The most popular method to produce graphene oxide GO is the Hummers method [74]. These layers can be separated from the bulk in a liquid phase getting graphene oxide layers of several hundreds of microns in size. The graphene oxide layers can be reduced back to obtain graphene sheets. The main technical difficulty of this method is the separation of graphene samples that tend to deteriorate using methods like ultrasonication. This method is more suitable to produce graphene paper, that is the result of the agglomeration of many individual graphene particles in a thicker material that is not a crystal.

Another way to induce graphene exfoliation from GO produced by the Hummers method is to form an electric arc between two graphite electrodes [75]. In a usual fabrication process two graphite electrodes are used of which one is filled with GO powder. The two electrodes are inside a hydrogen-argon mixture at atmospheric pressure and the distance between them is 2mm. Then an arc of 100-150A is induced between the electrodes that reduces the GO and then exfoliation of graphene can be induced through ultrasonication and centrifugation.

The previous methods exposed relied on the exfoliation of carbon layers from crystalline graphite using different methods to overcome the interlayer energy keeping them together. Now we will introduce two methods that synthesize graphene from basic components and one that makes graphene by subtraction of extra atoms. These later methods have the advantage of allowing the fabrication of larger samples with higher quality and better control over the final graphene placement[3].

2.2.2 Synthetic Methods: Epitaxial Growth on Metals

One of these methods is the epitaxial growth on a metal surface [70, 55]. In this method a well-ordered crystalline metal surface is used as a substrate for epitaxial graphene growth. Transition metals like Ruthenium (0001) [70] and Iridium (111) [55] have been used as

crystal substrates. The fact that the carbon solubility in transition metals is temperature dependent is used in the following manner. When the system is heated to about 1150 °C the carbon solubility is high inside the metal and the metal is saturated with carbon over its entire volume. Slow cooling of the sample to a temperature close to 825 °C results in a sixfold decrease in the solubility and the carbon accumulates on the metal surface in an organized manner forming a film. This film correspond to epitaxial graphene sheets with a moiré structure.

2.2.3 Synthetic Methods: Chemical Vapor Deposition

CVD is a method that has been used for a long time for the fabrication of carbon structures and nanostructures. In particular it has been one of the methods for the production of carbon nanotubes (CNTs) [11]. In this method a mix of precursor gases containing carbon reacts with a transition metal surface to deposit carbon layers on top of the metal. The usual result of the process was to deposit graphitic layers rather than thin layers of carbon. This problem was overcome by depositing thin layers of the transition metal (< 300nm) on a non-metallic substrate and rapidly cooling down the sample after the hot reaction step [39]. In a particular case the samples are heated to 1000°C in an Ar atmosphere. After the sample is hot a flow of a reacting mixture of (CH_4:H_2:Ar) is applied, and after some time the sample is cooled to room temperature at a rate of ~ 10 °Cs^{-1}.

After the sample is cool the graphene can be transferred to its final substrate by pressing a PDMS stamp and etching the metal under the graphene to use the stamp to transfer the film or by direct etching of the metal and transfer of the floating graphene to a substrate by downside contact [39]. The main challenges for this method of production is the synthesis of large graphene samples [5, 39, 46] comparable to the size of a wafer and the quality of the graphene in terms of uniformity and freedom from defects.

2.2.4 Synthetic Methods: Thermal Decomposition on SiC

Along with CVD there is another synthesis method that is suitable for the production of large scale high quality graphene. This is the thermal decomposition (also referred as annealing or sublimation) of silicon carbide SiC. This method yields epitaxial graphene

(EG) and as another advantage the transfer of the graphene can be avoided because SiC is a good substrate for many electronics applications [66, 33]. The graphitization of SiC by sublimation of the Si atoms was known for some decades and has been tailored to produce epitaxial graphene by de Heer [7, 8, 20, 21] and others [23, 32].

The process engineered at de Heer's lab is referred to as confinement controlled sublimation (CCS). In CCS a chip of SiC is heated in vacuum at high temperature in a graphite enclosure that has a leak for the Si to escape. The rate of graphene growth is controlled by the rate at which the Si atoms escape through the leak [66]. Because the interface between the graphene and the SiC is obtained at high temperatures it is free from contaminants and very reproducible.

The CCS process yields graphene structures on both faces of the SiC crystal. The graphene grown in the $(000\bar{1})$ face (also known as the carbon face or C face) is different from the one grown at the (0001) face (or Si face). In this work graphene at the C face is used. The material obtained at the C face is called multilayer epitaxial graphene (MEG). As a result of an unusual rotational stacking MEG has a band structure with Dirac cones like those of single layer graphene (SLG) [28] (with a small pertubation due to the weak interaction between layers). The layers are stacked so they are rotated near 0° and 30° alternatively with respect to the SiC substrate [66].

2.3 Basic Concepts of Solution-Gated Field Effect Transistors

As discussed previously in Chapter 1 SGFETs are a promising platform to build portable electrical chemical and biochemical sensors. In this section the basic operation principles of SGFETs are introduced. An SGFET is essentially a field effect transistor (FET) in which the gate electrode is immersed in a ionic liquid or ionic solution which is in contact with the channel. An introduction to FETs is a logical step to start our discussion.

The basic architecture of a FET consists of three terminals, an electrical conductive channel, and a dielectric (see Figure 2.6a). The terminals are named source, drain, and gate and their operation will be introduced using a p-channel metal-oxide-semiconductor FET (MOSFET) as an example [26]. In a p-channel MOSFET two n-doped islands are immersed

in a p-doped semiconductor. The n-doped islands are connected to metallic contacts and they correspond to the source and the drain terminals. The p-doped region between the source and the drain is called the channel and its conductivity will be modulated by the gate. There is an insulating layer on top of the channel (an oxide in the case of a MOSFET) and on top of it a contact called the gate is added.

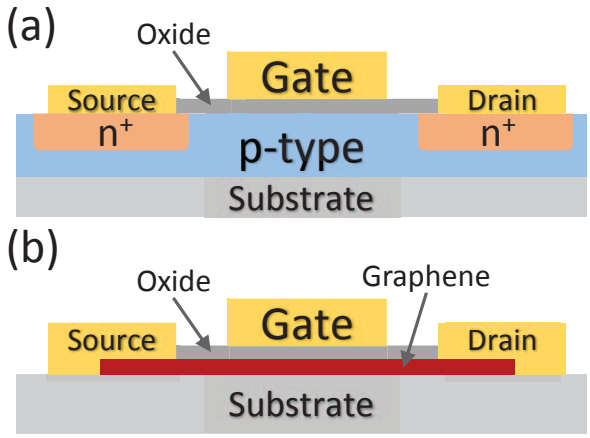

Figure 2.6: (a) Schematic diagram for a p-channel MOSFET (b) Schematic diagram for solid state graphene FET

If a voltage supply is connected between the source and the drain with an open gate the conductance between the first two terminals, G_{SD}, is zero as there are no charge carriers in the channel. If a positive potential with respect to the drain is applied to the gate terminal a layer with negative carriers (electrons) is formed in the channel region and a high current is formed between the drain and the source increasing G_{SD}. For small gate potential values the resistance in the channel is linear with respect to the gate voltage and for higher voltages the current reaches a saturation point where it cannot grow more. For this case the device is in the on state. When the gate potential is negative the channel stays off as more positive carriers are created (holes).

An schematic for a graphene FET is shown in Figure 2.6(b). For this device a very simple architecture is used where graphene is used as the channel. A graphene sheet is connected to two contacts (drain and source) and a gate contact is placed over a very thin oxide layer that is on top of the graphene sheet. A gate can also be connected to the bottom of the

substrate with the same operating principle but with a lower coupling so higher voltages are required to change the conductance in the channel [62]. In a SGFET the graphene channel is immersed in a liquid and an electrode is inserted in the liquid (see Figure 2.7). This electrode can be a bare wire (usually a silver wire coated in AgCl, called an Ag/AgCl electrode) or a reference electrode. A reference electrode is used in pH meters and in it a wire (can be also an Ag/AgCl wire) is inside a glass tube filled with a salt solution of fixed concentration. this tube has a porous end that allows diffusion of small molecules between the electrode solution and the main solution. As it is discussed in Section 4.2.1 there is a thin layer on top of the graphene where ions are depleted forming a dielectric. As a consequence the electrode inside the liquid works like the gate contact works for the case of a solid state graphene FET and the same conductance modulation by the gate is observed.

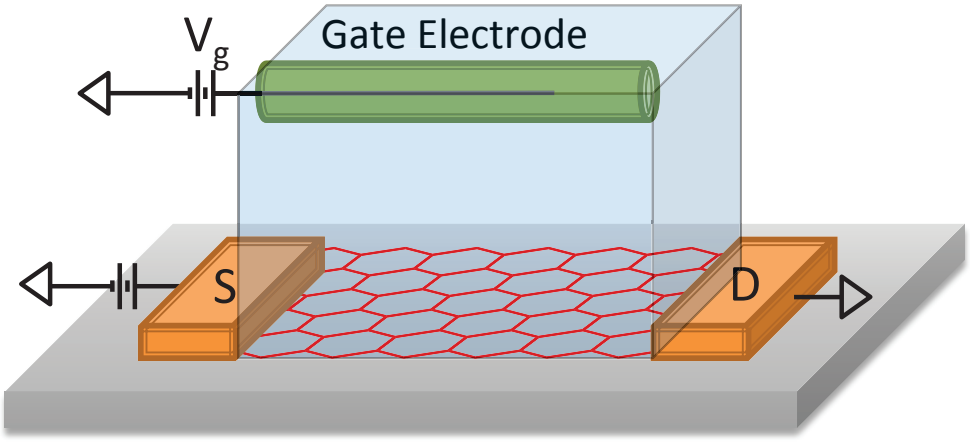

Figure 2.7: Schematic of an SGFET with potential sources (power supplies)

The band structure of SLG (and MEG) does not have a bandgap and so it has two regimes where either electrons or holes are the charge carriers. because of this there is no need for doping in a graphene FET (or SGFET) in order to have a conductance higher than zero in the channel. The carrier density n in the graphene channel is modulated by the gate electrode inside the liquid. The gate voltage effect is to shift the Fermi level inducing

an excess of holes or electrons in the channel. When the gate shifts the Fermi level below the Dirac point (see Figures 2.2, 2.3 and 2.8) the main carriers are holes and when the Fermi level is above the Dirac point the main carriers are electrons. There is a threshold voltage $V_{g,min}$ where there is an equal number of electrons and holes in the channel. When this happens the device is at the so called charge neutrality point (CNP) or the minimum conductance point (MCP) because the conductance is minimum in this condition. As it is explained in Section 2.4 the conductance is minimum at $V_{g,min}$ and it increases linearly in proportion to the carrier density n when the gate is away from $V_{g,min}$. When the gate voltage is such that the graphene is close to the CNP a plateau in the conductance versus carrier density plot is expected in the presence of impurities [1, 64] (see Section 2.4.3).

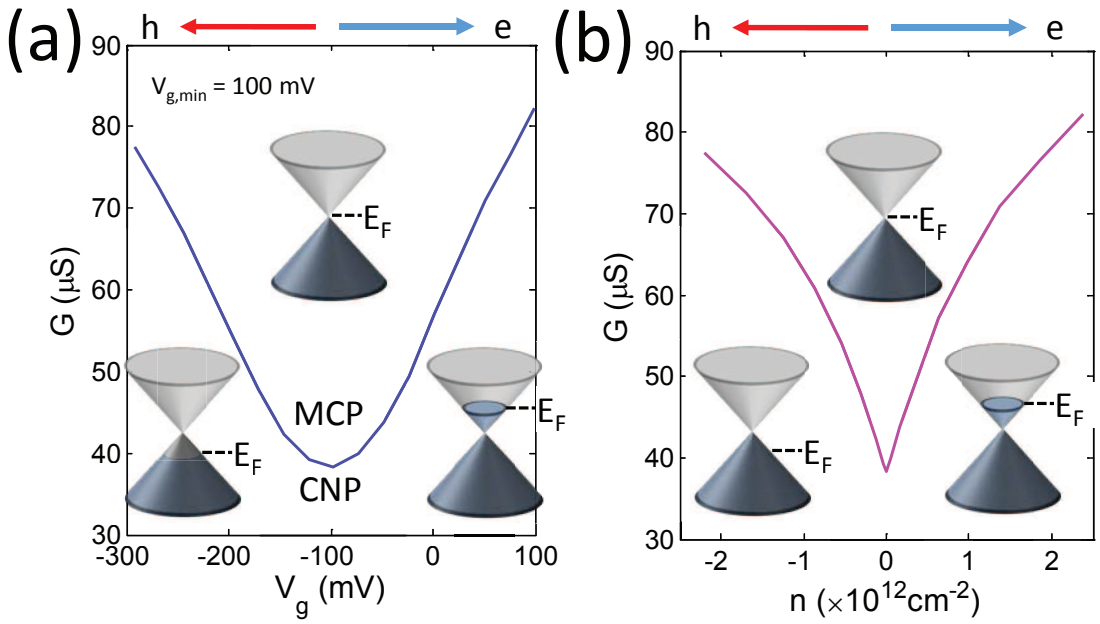

Figure 2.8: (a) Conductance versus gate voltage plot for a CVD SGFET. The solution for this experiment is 500 mM KCl. Annotations added to show the Fermi level and the carrier type at each region of the plot (b) Conductance versus carrier density plot for the same experiment. Same annotations as in (a) added

In Figure 2.8 the plots for conductance G versus gate V_g and G versus n are shown for a particular experiment (with one of our CVD SGFETs in KCl at 500 mM in deionized water). In Figure 2.8(a) a plateau around the MCP is clearly visible. Figure 2.8(b) is derived from the G versus V_g plot using Equation (4.13). The expected plateau for G versus n is difficult

to visualize because the first term in Equation (4.13) is the most significant, but the plateau can be estimated using the G versus V_g plots as will be done later in Chapter 5. In the G versus V_g plot shown in Figure 2.8(a) the MCP is not at $V_g = 0$, this case corresponds to a doped channel.

Doping Influence on the Gating Effect

The effect of doping in the graphene conductance can be understood using the band structure. For a very clean graphene sample the MCP is expected to be at a threshold voltage equal to zero volts. As charged impurities are added intentionally or by accident they move the Fermi level to either the valence or the conduction band. For electron donors (n-doping) the Fermi level is moved up and the opposite happens for acceptors (p-doping). This shift is observed in the conductance plot as a shift of the threshold voltage $V_{g,min}$. For the case shown in Figure 2.8(a) the Fermi level is above the Dirac point for $V_g = 0$ corresponding to n-doping. Both p-type and n-type doping have been observed previously in graphene SGFETs [47]. The origin of this doping is attributed to residues left by the fabrication process [1], but this doping can be also be induced to engineer the device response [14].

2.4 Graphene Conductivity Modeling

In this section the theory for graphene conductivity for both high carrier density and low carrier density (around the MCP) is introduced. The electron transport in graphene is limited by two processes. One is short range scattering by lattice defects that is the main mechanism in the ballistic conduction regime. This conduction is available when the graphene has a very low density of charged impurities, that is a very clean sample. n_{imp} is the density of impurities on the surface and is equal to N_{imp}/A, where N_{imp} is the total number of impurities in the material. When n_{imp} for charged impurities is high enough the scattering due to these impurities becomes significant and limits the conductivity of the material. Theoretical works have considered these main sources of scattering predicting different results for the conductance dependence on the carrier density. The results obtained so far

do not fully agree with the experimental results but there is one approach that makes predictions with better accordance to the current experimental results for SGFETs. Nomura and McDonald [56] studied numerically the conductivity σ dependence on carrier density n for both types of scatterers (see Figure 2.9). They found a nonlinear dependence of σ to the carrier density for short range scatterers with a minimum value $\sigma \approx (1/\pi)e^2/h$. For Coulomb scatterers they found a linear dependence for σ with a minimum value larger than the value projected for short range impurities ($\sigma \approx e^2/h$).

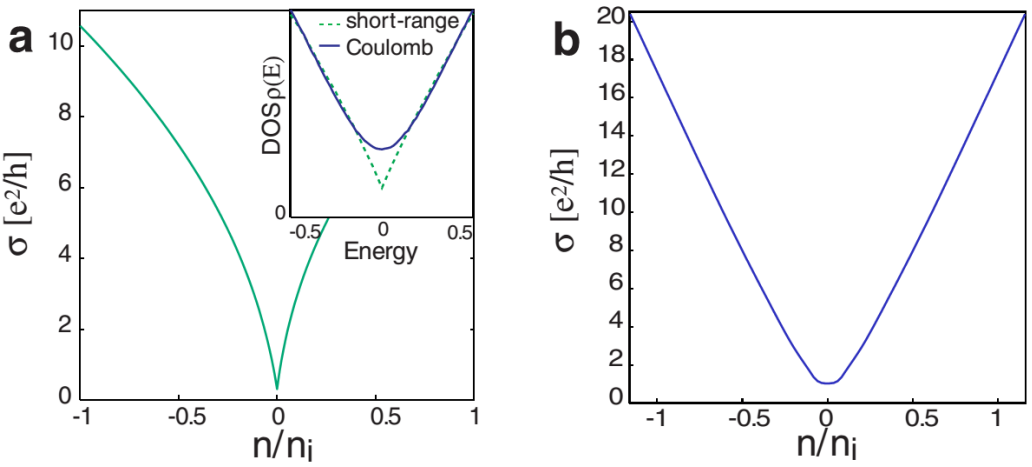

Figure 2.9: Dirac-fermion conductivities for (a) short range scatterers and (b) screened Coulomb scatterers. The inset of (a) compares the densities of states for short range and Coulomb cases. [56]. Adapted with permission from (Physical Review Letters, 98(7), 076602. Copyright (2007) APS).

2.4.1 Conductivity with Coulomb Scatterers

For the case of SGFETs the results obtained are closer to the predictions for the conductivity that consider charged impurities [1, 12, 71]. In order to explain the observed behavior for the conductivity (or conductance) a semiclassical approach is needed. In it the conductivity of graphene around the MCP is explained using Boltzmann transport theory using a quantum mechanical calculation for the electron scattering by charged impurities in the the random phase approximation (RPA) [56].

2.4.2 Conductivity of Graphene for High Carrier Density

Using the Boltzmann transport theory with the RPA [49] an expression for the conductivity in terms of carrier density n, concentration of impurities n_{imp}, and other basic constants and parameters can be obtained [1, 64]. This calculation is called semiclassical as it considers the transport of the carriers to be a classical diffusive process, but the scattering of them by the scattering centers is a quantum mechanical process. For this calculation the carrier density is $n = k_F^2/\pi$ ensuring that only carriers at the Fermi level participate in conduction.

Using the semiclassical Boltzmann formalism for graphene the semiclassical diffusive conductivity $\sigma = e^2\nu(E_F)D$ is obtained (see Section 2.1.4), where $\nu(E_F) = g_s g_\nu |E_F|/(2\pi\hbar^2 v_F^2)$ is the density of states at the Fermi energy [10] and $D = v_F^2\tau/2$ is the diffusion constant in 2D. The result for the conductivity obtained in Equation (2.39) is reproduced here,

$$\sigma = \frac{g_s g_\nu e^2 E_F \tau}{h \quad 2\hbar} \tag{2.41}$$

In the graphene literature σ is the symbol for sheet conductance and in electrochemistry the same symbol is reserved for surface charge. In this document the surface charge is denoted by σ_d.

In the previous expressions $g_s = g_\nu = 2$ are the spin and valley degeneracy factors, v_F is the Fermi velocity, and τ is the scattering time. The next step is to find the scatering time given at T=0 using

$$\frac{\hbar}{\tau(\mathbf{k})} = \frac{n_{imp}}{4\pi}\int d\mathbf{k}' \left[\frac{V(|\mathbf{k}-\mathbf{k}'|)}{\epsilon(|\mathbf{k}-\mathbf{k}'|)}\right][1-\cos^2(\theta)]\delta(E_{k'} - E_k) \tag{2.42}$$

where $V(q) = 2\pi e^{-qd}/(\kappa q)$ is the Fourier transform of the Coulomb potential at the transfer momentum $q = |\mathbf{k}-\mathbf{k}'| = 2k_F \sin(\theta/2)$ as only electrons at the Fermi level participate in conduction. For the static dielectric function $\epsilon(q)$ that accounts for electron screening the following approximation is used [1]

$$\epsilon(q) = \begin{cases} 1 + q_s/q & \text{if} \quad q < 2k_F, \\ 1 + \pi r_s/q & \text{if} \quad q > 2k_F, \end{cases} \tag{2.43}$$

where $r_s = 2e^2/\hbar v_F(\epsilon_1 + \epsilon_2)$ is the dimensionless Wigner-Seitz radius, which quantifies the ratio of the potential to the kinetic energy in an quantum Coulomb interaction. In other

works this constant describes the coupling strength of the dielectric media to graphene [13]. And $q_s = 4k_F r_s$.

After solving the integral for τ analytically we find an expression for $\sigma(n)$

$$\sigma(n) = \frac{e^2\, n}{h\, n_{imp}} \frac{2}{G(2r_s)} \tag{2.44}$$

where for $G(x)$ we have

$$\frac{G(x)}{x^2} = \frac{\pi}{4} + 3x - \frac{3\pi x^2}{2} + \frac{x(3x^2-2)\arccos(1/x)}{\sqrt{x^2-1}}. \tag{2.45}$$

In our case $\epsilon_1 = 10\epsilon_0$ for SiC and $\epsilon_2 = 80\epsilon_0$ for water. Setting $v_F = 1.1 \times 10^6 m/s$, we get $2/G(2r_s) \simeq 25$. $2/G(2r_s)$ is called C in Section 2.1.4.

2.4.3 Conductivity of Graphene Around the Dirac Point

Equation (2.44) is valid as long as the gate voltage is different enough from $V_{g,min}$ to have a carrier density bigger than $n_{imp}/2$ in the graphene channel. In the experiments carried out so far in the literature the samples have charged impurities that are responsible for the graphene's conductivity around the Dirac point too. These impurities induce puddles of electrons and holes (carriers) that will be the main source for the conductivity. The impurities are also responsible for the actual value of the conductivity as they are the main source of scattering. Klein tunneling allows transitions between holes and electrons and it is the way that electrons (holes) cross the boundary between puddles mutating into holes (electrons) in the next puddle so the conductivity is mainly dependent on the physics of the puddles.

An assumption made to calculate the conductivity around the Dirac point is that the same Boltzmann semiclassical approach is valid for small carrier density values. A justification for this guess is that the conductivity value is continuous at the carrier density where the high carrier model breaks down and the conductivity value stays closer to the value at the point where the theory breaks down. As a first approximation the carrier density around the Dirac point is assumed to be constant, this is called the residual carrier density (n^*) and it is related to the root-mean-square fluctuations of the carrier density (n_{rms}). The gist of the calculation is to estimate n^* and to replace it in Equation (2.44). A limitation to this

approach is that the value for the conductivity at the Dirac point will be the same for every carrier density inside the plateau. The next approximation level to get a better shape for the plateau is obtained using the effective medium theory (EMT) that considers a Gaussian distribution for the carrier density close to the Dirac point with width equal to n_{rms} and an appropriate value for its mean (see [64] Chapter 12). But this first approximation is good to understand the origin of the conductivity around the Dirac point.

The calculation for $n^* = n_{rms}/\sqrt{3}$ is a self-consistent ansatz, that is a calculation that can be understood with a mental model where the interaction between their variables lead to mathematical expressions that will be solved self-consistently. The ansatz can be described as follows: if the induced charge density n^* is small, the potential from the impurities will be poorly screened and more charge can be induced. If we initially estimate a value for n^* that is too high it will screen the impurities potential too much that would require a lower estimation for n^*. So the induced charge needs to be just high enough to screen the impurities potential to a final state where the total potential is consistent with the charges induced.

A quantitative approach to the ideas described above can be developed. Assuming that n_{rms} comes from the Thomas-Fermi contribution we have $n_{rms} \approx \sqrt{3}\langle E_F^2\rangle/(\pi\hbar^2 v_F^2)$, where the brackets denote an ensemble average. For this assumption the self-consistent ansatz is

$$\pi\hbar^2 v_F^2 n^* = \langle E_F^2\rangle = \langle V_D^2[n^*]\rangle \tag{2.46}$$

where $\langle V_D^2[n^*]\rangle$ is the disorder potential screened at a carrier density n^*. To calculate this potential assuming uncorrelated random impurities the potential autocorrelation function can be used:

$$\langle V_D(r)V_D(0)\rangle = n_{imp}\int \frac{d^2q}{(2\pi)^2}[\widetilde{\phi}(q,n)]^2 e^{-i\mathbf{q}.\mathbf{r}} \tag{2.47}$$

where each impurity has a disorder potential $\phi(r,n)$ with Fourier transform $\widetilde{\phi}(q,n)$. In this case the Coulomb potential is the same used for the high carrier density calculation,

$$\widetilde{\phi}(q,n) = \frac{2\pi e^2}{\kappa}\frac{e^{-qd}}{q\epsilon(q)}. \tag{2.48}$$

Before proceeding to the calculation a final note is needed. If the autocorrelation for the

impurity potential is postulated to be Gaussian, the following expression is obtained for it,

$$\langle V_D(r)V_D(r')\rangle = K_0\frac{(\hbar v_F)^2}{2\pi\xi^2}e^{-|\mathbf{r}-\mathbf{r}'|/(2\xi^2)}. \tag{2.49}$$

In this expression K_0 is a dimensionless measure of the potential strength and ξ specifies its correlation length. Putting Equations (2.46), (2.47) and (2.49) together the equations for the SCA can be written as:

$$\frac{K_0\hbar^2v_F^2}{2\pi\xi^2} = n_{imp}\int\frac{d^2q}{(2\pi)^2}[\widetilde{\phi}(q,n)]^2 = \pi\hbar^2v_F^2n^*, \tag{2.50}$$

where the correlation length ξ for Coulomb impurities is,

$$\xi = \sqrt{\frac{2}{\pi}}\frac{\int\frac{dq}{2\pi}[\widetilde{\phi}(q,n)]^2}{\int\frac{d^2q}{(2\pi)^2}[\widetilde{\phi}(q,n)]^2}. \tag{2.51}$$

The integrals in Equations (2.50) and (2.51) for n^*, K_0, and ξ can be solved analytically and further approximations cannot be used in the regime found in experiments. The self-consistent solution for n^* is,

$$\frac{n^*}{n_{imp}} = 2r_s^2C_0^{RPA}(r_s, 4d\sqrt{\pi n^*}) \tag{2.52}$$

where $C_0^{RPA}(r_s, 4d\sqrt{\pi n^*})$ is the correlation function from the RPA and d ($\sim$ 1 nm) is the average distance from the impurities to the graphene plane. The auxiliary function $C_0^{RPA}(r_s, z)$ is,

$$C_0^{RPA}(r_s,z) = -1+\frac{4E_1(z)}{(2+\pi r_s)^2}+\frac{2e^{-z}r_s}{1+2r_s}+(1+2zr_s)e^{2zr_s}(E_1(2zr_s)-E_1(z(1+2r_s))), \tag{2.53}$$

and

$$E_1(x) = \int_x^\infty t^{-1}e^{-t}dt \tag{2.54}$$

2.4.4 Final Results

Putting together the results of the two previous sections we get the following expression for graphene conductivity in the presence of Coulomb impurities,

$$\sigma(n-\bar{n}) = \begin{cases} \frac{e^2\,n^*}{h\,n_{imp}}\frac{2}{G(2r_s)} & : n-\bar{n} < n^*, \\ \frac{e^2\,n}{h\,n_{imp}}\frac{2}{G(2r_s)} & : n-\bar{n} > n^*. \end{cases} \tag{2.55}$$

To estimate the impurities density n_{imp} from an estimated value for the residual carrier density n^* or viceversa, the following expression can be used

$$\frac{n^*}{n_{imp}} = 2r_s^2 C_0^{RPA}(r_s, 4d\sqrt{\pi n^*}). \tag{2.56}$$

From these calculations we also can get an expression for the carrier density that is associated to the shift of the threshold voltage from zero $\bar{n}$ [1, 19]

$$\bar{n} = \frac{n_{imp}^2}{4n^*}. \tag{2.57}$$

CHAPTER III

EXPERIMENTAL METHODS

3.1 Graphene Sources

Two types of graphene were used in this work: epitaxial graphene (EG) fabricated in the de Heer lab at Georgia Tech by CCS, and CVD graphene provided by Marder's lab at Georgia Tech. The EG was MEG on the C-face of a SiC wafer and thus its energy bands correspond to those of single layer graphene (SLG) [66] (see Section 2.2.4). The CVD SLG was transferred to an undoped Si wafer with a thin oxide layer of 300nm on top. This layer provides electrical insulation and it is also useful for graphene visualization purposes as graphene is optically visible over SiO_2. The device fabrication process and experimental details are the same for both graphene types as their substrates were rigid and of similar thickness. EG was provided on $3.5mm \times 4.5mm$ chips. CVD samples were deposited over a $2.5cm \times 2.5cm$ Si/SiO_2 wafer that was diced into $4.5mm \times 4.5mm$ chips using a dicing saw.

3.2 Device Fabrication

Two epitaxial graphene SGFETs were fabricated per chip (Figure 3.1(a)). The wafers had an average number of graphene layers between 1.5 and 6 layers. The graphene thickness was determined from ellipsometry measurements yielding values ranging from 5-20 Å and the numbers of layers was found assuming a thickness of 3.3 Å per layer. Starting with a 3.5 mm × 4.5 mm SiC chip with EG on the C face, two rectangular 300 μm × 1500 μm EG strips were produced per chip via oxygen plasma etching (flow = 20 sccm, power = 20W in a Oxford End-point RIE) for 15 seconds to remove the graphene outside the channels using Futurrex NR9-1500PY photoresist as an etching mask (developed using RD6). After removal of the photoresist using acetone, metallic contacts (Ti/Pd/Au, 1 nm/20 nm/50 nm) were deposited at each end of the strip using electron beam evaporation together with a second photoresist mask (NR9-1500PY). The contacts covered part of the edges of the

graphene strips (250 μm) to ensure good electrical contact (see Figure 2.6b). Lastly, a 1.5 μm thick layer of SU-8 was added to electrically insulate the contacts, leaving a 300 μm $\times$ 500 μm 'active' region of each EG strip exposed to the gating solution.

Figure 3.1(b) shows a side-view schematic of the device which demonstrates the use of a plastic well is attached to the sample using vacuum grease (Dow Corning High-Vacuum Grease) after the wire bonding of the graphene strips to a chip carrier (Practical Components). A photo of the completed device including the chip carrier and custom-made well to contain the solution is shown in Figure 3.1(c). The well was 3D printed by Fineline Prototyping in ABS-like photoplastic (Acrylonitrile butadiene styrene, commercial name: Somos(R) WaterShed XC 11122).

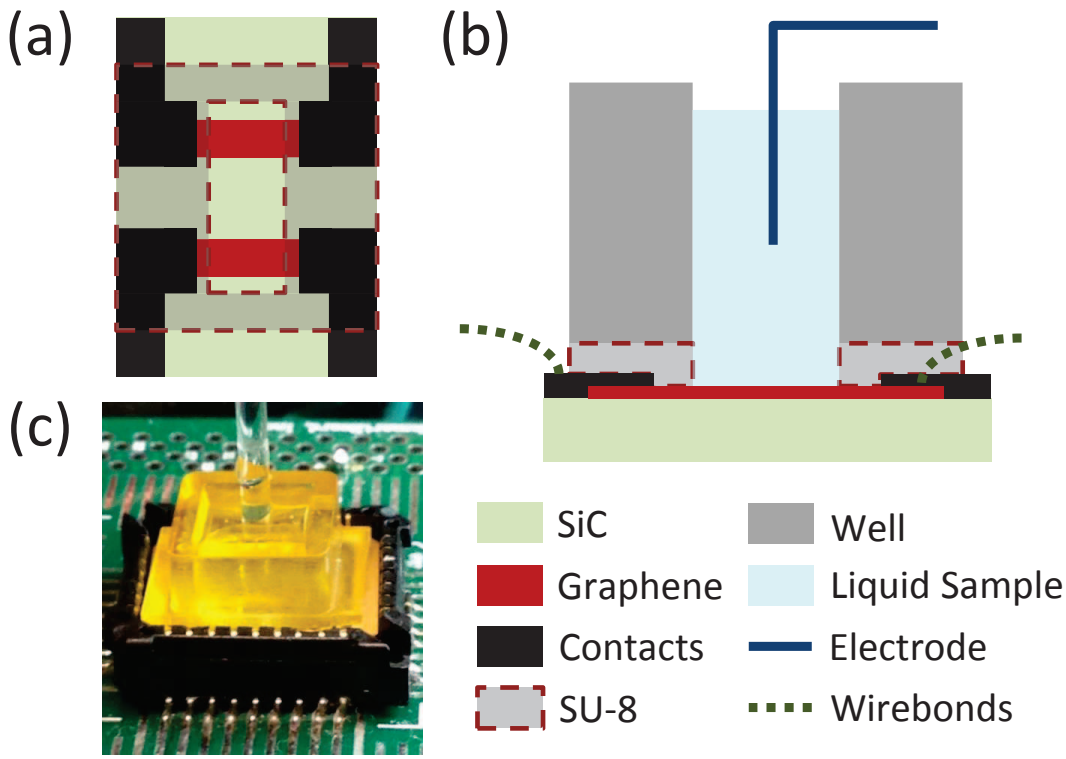

Figure 3.1: Schematic of epitaxial graphene SGFET. (a) Top view showing openings in the SU8 passivation layer for graphene strip access (center) and contact wire bonding (chip ends). (b) Side view showing liquid well, electrode and wire bonds. (c) Photo of a device complete with liquid well, electrode and chip carrier

3.3 Electrical Measurements

Different types of liquid samples (see Chapters 4 to 6) were placed in contact to the graphene channel inside a well as it is shown in Figures 3.1 and 3.2. After this, the gate electrode was placed inside the sample. This electrode was connected to an Agilent E3631A DC power supply. Two types of electrodes were used: a bare electrode consisting of a silver wire coated in AgCl (Ag/AgCl wire) and a fluid filled reference electrode which consisted of an Ag/AgCl wire in a 1M KCl solution with a porous glass provided by the laboratory of Dr. Jiri Janata at Georgia Tech.

Gate leakage current, $I_g = V_s/R_s$, was calculated by monitoring the voltage drop across a $R_s = 1$ MΩ resistor connected in series with the gate electrode (see Figure 3.2) using a HP34401A Multimeter. The voltage drop across the resistor (V_s) was taken into account in the determination of the effective V_g. V_s is only a few mV having a negligible impact on V_g.

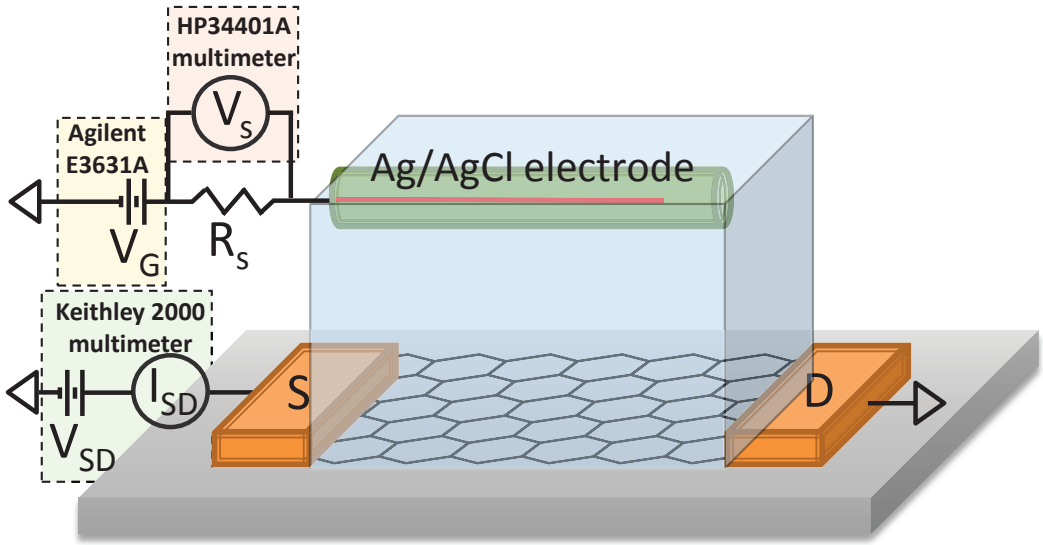

Figure 3.2: Schematic of an SGFET with laboratory instruments and a reference electrode.

The conductance across the source and drain contacts is obtained with a Keithley 2000 multimeter the following way: the current between source and drain I_{SD} is measured with a fixed source voltage V_{SD} for a given time. The final expression for the conductance is,

$$G = \frac{I_{SD}}{V_{SD}}. \tag{3.1}$$

All the readings from the instruments were performed automatically in a desktop computer using the GPIB ports for each multimeter. The power supply was also controlled via GPIB. The data capture was automated using a custom graphical user interface (GUI) built in Matlab. The devices and the gate electrode were connected to the multimeters and power supplies by digital multiplexers (Texas Instruments SN74CB3Q3251). These automatic switches have a very low on resistance ($r_{on} = 4\Omega$ typically).

These electrical connections were controlled automatically from a desktop computer using an Opal Kelly XEM3001 FPGA integration module. A very simple logic program was implemented in the card so that the multiplexers could be controlled from Matlab. This architecture provided the possibility of addressing the two devices in a chip without rewiring the setup.

CHAPTER IV

IONIC STRENGTH SENSING WITH GRAPHENE SOLUTION GATED FIELD EFFECT TRANSISTORS

4.1 Introduction

The goal of this chapter is to present a complete characterization of time dependent electrical conductance, device performance, and gate leakage effects under ionic strength changes in epitaxial graphene strips acting as conductive, solution gated channels in a SGFET device. Some preliminary results with recently developed CVD graphene SGFETs are also presented. First we present the conductance response to ionic strength for one epitaxial graphene device and we find its threshold voltage sensitivity to salt concentration. Then we report threshold sensitivity values for more than a dozen devices to examine device performance and variability. We also examine the reversibility of the graphene conductance and the graphene response to different ionic strengths at a fixed gate. Finally, we analyze the relation between sample degradation and leakage current.

Few studies have been carried out with EG-SGFETs and two of these studies have focused on pH detection [2, 65] (see Appendix A). The other was focused on specific biosensing [72]. There have been only a few experiments focused on salt concentration (ionic strength or IS) sensing using exfoliated graphene SGFETs [29, 12]. Results for ionic sensing present a shift in the Dirac voltage $V_{g,min}$ (also called threshold voltage) when the ionic strength is changed. A summary of the results is in Table 4.1. Chen [12] presents results for sodium fluoride NaF and sodium perchlorate $NaClO_4$ and analyzes his results using the electrical double layer (see Section 4.2.1) model. Using Equation (4.4) (Grahame equation) the surface charge σ_d is fitted to match the dependence of the threshold voltage on the ionic concentration. This approach is limited by requiring a fixed surface charge for every ionic strength case.

Heller [29] presents results for potassium chloride solutions at pH 7 and pH 3. He

introduces a more complete theoretical model to analyze his results. This is the model introduced in this chapter and used to analyze of our results. This model has several parameters that consider the experimental conditions and two parameters that can be used to fit the experimental data. These are the surface concentration of ionizable groups σ_{max} and an offset charge σ_{offset} that accounts for permanently ionized groups that are not sensitive to the solution. To analyze his results, Heller assumes two different types of ionizable groups at different pH values ($\sigma_{max} = \pm 0.5e/nm^2$, σ_{offset} unreported) and does not report the surface charge for different ionic strength and pH values. We found that his modeling approach does not require to assume different charge types under different conditions (σ_{max} can be assumed to be of the same polarity, and so of the same nature, for both pH values) and that we can use it to estimate the surface charge for the ionic strengths used experimentally.

In this chapter and the next, we provide a complete analysis using a numerical computation to fit the surface charge parameters σ_{max} and σ_{offset} for several EG and CVD SGFETs. We also use the values for the surface charge projected by the model to further analyze and understand the surface charge change at different conditions (pH and ionic strengths).

Table 4.1: Experimental results for ionic strength sensing

Publication	Graphene source	Salt	IS range	Sensitivity (mV/decade)
Chen2009 [12]	Exfoliated	NaF, $NaClO_4$	10mM-1M	-50
Heller2010 [29]	Exfoliated	LiCl, KCl	10mM-1M	-42.7 (pH 7)
			10mM-1M	18.9 (pH 3)

4.2 Modeling Ionic Strength Effect on Threshold Voltage

In solid state graphene FETs the gate is coupled to the channel by a dielectric (usually an oxide) that has a fixed capacitance. This capacitance can be calculated using the parallel plate formula when the thickness of the oxide, its relative permittivity, and its area are known. In SGFETs the electrical double layer induced at the graphene surface in contact

with an ionic solution works as a gate capacitance. This capacitance is tuned by the concentration of ions in the solution as it is explained in Section 4.2.1. But this effect alone is not enough to explain the shift in the Dirac voltage with the change in ionic strength. A fraction of the charge in the graphene surface can be attributed to ionizable chemical groups adsorbed in its surface [29]. A chemical ionization model that allows for heterogeneity in the ionizable species and the possibility of permanent charges that are independent of the ionic solution in contact with the surface is introduced in Section 4.2.2. These two models can be used together to model the shift of the Dirac voltage with the change of salt concentration.

4.2.1 The Electrical Double Layer

The basic model for the electrical double layer (EDL) includes two regions called the compact (Stern) and the diffuse layer.

When a charged surface is in contact with an ionic solution it attracts ions in the solution of opposite charge (counter-ions) and repels ions of the same charge (co-ions). The ions attracted to the surface come as close as possible to the surface forming a layer of charges parallel to the surface. Each ion inside a polar solvent (like water) has a solvation sheath formed by dipolar molecules surrounding the ion. The distance of closest approach is limited by the solvation sheath. The charge at the surface may be from dissociated surface groups, tightly adsorbed ions, or charge induced (coming from the substrate) by a potential applied to the bulk of the solution. In our case the origin of the surface charge is a combination of all these types of charge.

The double layer formed by the surface charge and the layer of counter-ions at the distance of closest approach is called the Stern layer or the compact double layer. The layer of ions in the liquid closer to the surface is called the outer Helmholtz plane (OHP) (see Figure 4.1). If there are tightly adsorbed ions they are closer to the surface than the free ions in the liquid. These ions form another layer called the inner Helmholtz plane (IHP). In reaction to the compact double layer the charge inside the liquid reorganizes forming the diffuse double layer. In the bulk of the liquid the net charge is zero because the concentration of co-ions and counter-ions is equal. In the OHP there is an excess of

counter-ions and a depletion of co-ions so there is a diffusion of counter-ions from the OHP and of co-ions into the OHP due to osmotic pressure. The region between the OHP and the bulk is called the diffuse layer. The thickness of this region is called the Debye length (λ_D).

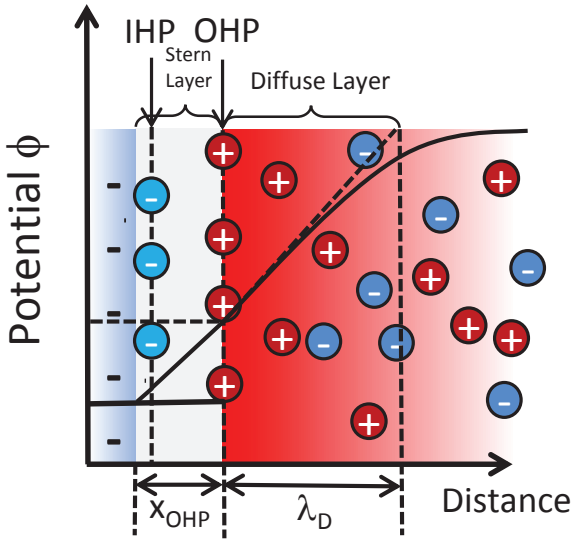

Figure 4.1: Electrical Double Layer diagram

The net charge in the diffuse layer is maximum at the OHP and decreases until is zero in the bulk. The thickness of this layer depends on the concentration of ions in the bulk. As the ionic concentration increases there is an increasing osmotic pressure and the excess ions near the OHP cannot go too far into the bulk. This makes the diffuse layer thinner and λ_{D} decreases. The EDL can be viewed as a capacitor and its capacitance increases at higher ionic strength as λ_{D} decreases. The process described above is mathematically described for the case of a flat surface (1D) by the Poisson-Boltzmann equation,

$$\frac{d^2\psi(x)}{dx^2} = -\frac{e}{\varepsilon_r \varepsilon_0} \sum_i z_i n_i^{\infty} \exp\left(-\frac{z_i e \psi(x)}{kT}\right) \tag{4.1}$$

where $\psi(x)$ is the electric potential at a distance x from the surface, n_i^{∞} is the concentration of ions of type i in the bulk solution, z_i is the valence of the i^{th} ion, e the charge of the electron, ε_0 the vacuum permittivity, ε_r the dielectric constant of the medium, k the Boltzmann constant, and T the temperature. This equation comes from the Poisson equation

using the Boltzmann distribution for the charge density inside the solution,

$$\begin{aligned} n_i(x) &= n_i^{\infty} \exp\left(-\tfrac{z_i e\psi(x)}{kT}\right) \\ \rho(x) &= e\textstyle\sum_i z_i n_i(x). \end{aligned} \tag{4.2}$$

An expression for the first derivative of $\psi(x)$ with two ionic species of opposite charges ($z_1 = \pm z, n_1^{\infty} = n^{\infty}$) can be obtained from Equation (4.1),

$$\frac{d\psi(x)}{dx} = \left(\frac{2kTn^{\infty}}{\varepsilon\varepsilon_0}\right)^{1/2} \left[\exp\left(-\frac{ze\psi(x)}{kT}\right) - \exp\left(\frac{ze\psi(x)}{kT}\right)\right]. \tag{4.3}$$

From this equation an expression for the interfacial charge at the OHP σ_d in terms of the potential there ψ_d and the ionic concentration n^{∞} can be obtained.

$$\sigma_d = \left.\frac{d\psi}{dx}\right|_d = (8kT\varepsilon\varepsilon_0 n^{\infty})^{1/2} \sinh\left(\frac{ze\psi_d}{2kT}\right). \tag{4.4}$$

This expression is called the Grahame equation. An alternative version of this expression will be useful later,

$$\sigma_d = \frac{2\varepsilon_r\varepsilon_0}{\beta e\lambda_d} \sinh\left(\frac{\beta e\psi_d}{2}\right). \tag{4.5}$$

In this expression $\lambda_D = (2\beta n^{\infty} e^2/\varepsilon_r\varepsilon_0)^{-1/2}$ is the Debye length and $\beta = 1/kT$.

In an SGFET an EDL is expected to form at the graphene surface and at the gate electrode (see Figure 4.2). The gate electrode is immersed in a very high ionic solution with constant ionic strength. Therefore, the EDL at the gate is independent of the liquid solution in contact with the device.

4.2.2 The Basic Stern Model for Ionization of a Surface

A second expression relating the interfacial charge and the OHP potential can be derived by using the Langmuir-Freundlich adsorption isotherm [4]. The mechanism of ionization of the surface functional groups can be described by the chemical equation,

$$\mathrm{AH} \rightleftarrows \mathrm{A}^- + \mathrm{H}^+ \tag{4.6}$$

where A^- and H^+ represent the ionized groups and the hydrogen ions (protons) respectively. Defining Γ_{A^-} as the surface concentration of ionized groups, the surface charge density is given by

$$\sigma_d = -e\Gamma_{A^-} \tag{4.7}$$

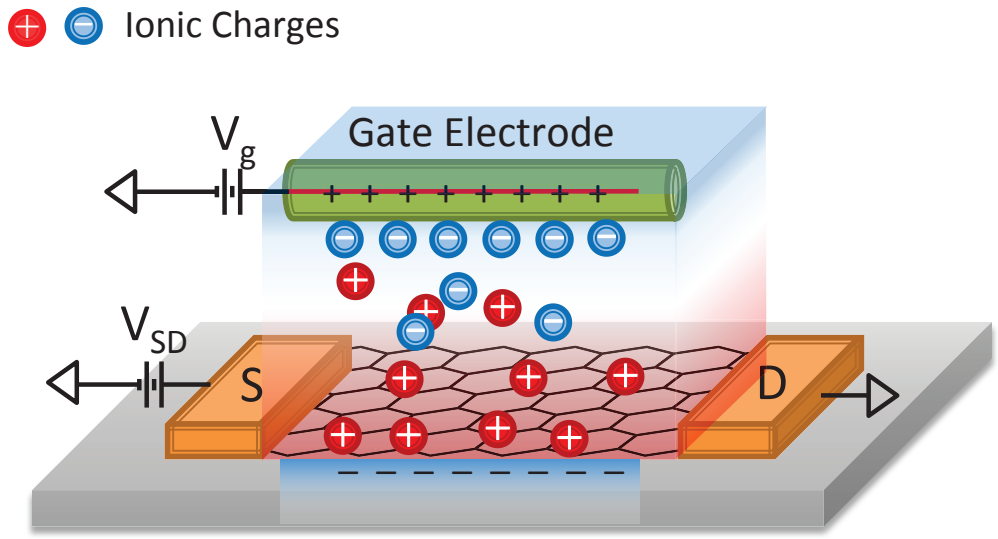

Figure 4.2: Schematic of an SGFET with potential sources (power supplies) and charge distribution

where e is the electron charge. The subindex d has been added to the surface charge symbol to differentiate it from the conductance. The surface density of ionizable groups (corresponding to the density of ionizable groups at the surface) is,

$$\Gamma = \Gamma_{A^-} + \Gamma_{AH}. \tag{4.8}$$

where Γ_{AH} is the surface density of non-ionized groups.

So the maximum charge density possible is $\sigma_{max} = -e\Gamma$. With these definitions the mass action law in the Langmuir-Freundlich model is,

$$\frac{[H^+]_0^m \Gamma_{A^-}}{\Gamma_{AH}} = 10^{-mpK} \tag{4.9}$$

where $[H^+]_0$ is the surface concentration of protons in the OHP and $m = 1/2$ is a parameter that takes into account the heterogeneity of the charged species [29]. From the Boltzmann distribution, the relation between hydrogen ion concentration at the surface and hydrogen concentration in the bulk is,

$$[H^+]_0 = [H^+]_b e^{-\beta e \psi_0}, \tag{4.10}$$

where $[H^+]_b = 10^{-pH}$. The potential drop in the Stern layer is modeled using a phenomenological capacity [6],

$$C = \frac{\sigma_d}{\psi_0 - \psi_d}, \tag{4.11}$$

where $C = \epsilon_r \epsilon_0 / x_{OHP}$ and $x_{OHP} = 4\mathring{A}$. Solving Equations (4.7) to (4.10) for the OHP potential ψ_d we obtain,

$$\sigma(\psi_d) = \frac{\sigma_{max}}{1 + 10^{m(pK-pH)} e^{-m\beta e \psi_{OHP}}} + \sigma_{offset} \tag{4.12}$$

where σ_{max} is the charge at 100% ionization and σ_{offset} corresponds to charges that do not change with ionic concentration. A self-consistent solution of Equation (4.4) and Equation (4.12) gives the potential at the OHP and the surface charge (σ_d and ψ_d). To obtain the potential at the surface Equation (4.11) can be used [29].

4.3 SGFET conductance response for different ionic strength solutions

As was explained in Section 2.3 the conductance G in an SGFET has a minimum conductance at the threshold voltage $V_{g,min}$ (also called the Dirac voltage) and increases when the gate voltage V_g is set away from $V_{g,min}$. The gate induces carriers that can be electrons (when $V_g > V_{g,min}$) or holes (when $V_g < V_{g,min}$). Both types of carriers have very similar mobility so the G versus V_g plot is almost symmetrical. It has been shown theoretically in Section 2.4 that the conductivity (and so the conductance) depends linearly on the induced carrier density n when V_g is away from $V_{g,min}$ and has a plateau in the presence of impurities near $V_{g,min}$.

In our experiments we measure the G versus V_g response of our devices. To analyze our experimental results using the theoretical framework laid out in Section 2.4 we need to convert our gate voltages to their corresponding effective carrier densities [19]. Considering a potential difference between the graphene and the gate electrode the following relationship can be obtained between the gate voltage and the carrier density,

$$|V_g - V_{g,min}| = \frac{\hbar v_F \sqrt{\pi n}}{e} + \frac{ne}{C_{DL}}, \tag{4.13}$$

where $v_F = 1.1 \times 10^6$m/s is the Fermi velocity, e is the electron charge, and C_{DL} is the double layer capacitance. This capacitance is given by $C_{DL} = (\epsilon_r \epsilon_0)/\lambda_D$, where λ_D is the

Debye lenght ($\lambda_D = (2\beta n^{\infty} e^2/\varepsilon_r \varepsilon_0)^{-1/2}$, see Section 4.2.1). The first term in this equation correspond to the quantum capacitance and the second term to the gate capacitance. In this case the gate capacitance is the double layer capacitance as seen in Section 4.2.1. For our ionic sensing experiments we used salt solutions with concentrations c^{∞} in the range [10 mM, 1000 mM]. To calculate the ionic concentration n^{∞} we use the expression $n^{\infty} = c^{\infty} N_A$, where c^{∞} is in mM and N_A is the Avogadro constant. Using $\varepsilon = 80$ (for water) we obtain the following values for λ_D and C_{DL} (see Table 4.2).

Table 4.2: Debye lengths and double layer capacitances for several salt concentrations

c^{∞} (mM)	λ_D (nm)	C_{DL} $(\mu F\, cm^{-2})$
10	3.071	23.1
20	2.171	32.6
50	1.373	51.6
100	0.971	73.0
200	0.687	103.2
500	0.434	163.1
1000	0.307	230.7

Figure 4.3 shows the carrier density versus gate displacement from the Dirac voltage $|V_g - V_{g,min}|$ for several salt concentrations. The quantum capacitance is dominant for the concentrations considered so the plots are very similar for all concentrations. The dependence of n on $|V_g - V_{g,min}|$ is semi-parabolic (as the second term in Equation (4.13) is almost negligible).

In this section we begin our presentation of the basic ionic sensing results for epitaxial graphene SGFETs with bare and reference electrodes. Nineteen devices were used in these experiments. We characterized the shift of the MCP when the devices were exposed to potassium chloride (KCl) solutions of different ionic strengths (10 mM to 1000 mM). The KCl salt was dissolved in deionized water with no buffer. The pH for the salt solutions was measured and a value of pH around 5.2 was obtained for all the solutions (except for 10 mM where the pH was 5.8). The gate leakage current I_g was monitored during our measurements as indicated in Section 3.3.

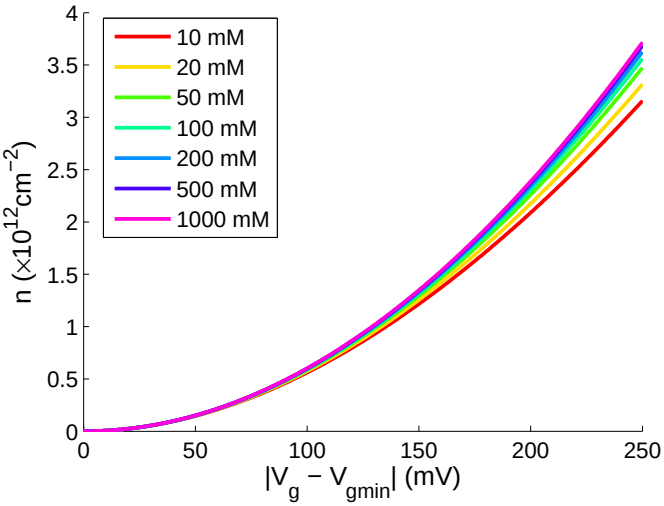

Figure 4.3: Carrier density versus gate voltage calculated for salt concentrations in the range [10 mM, 1000 mM].

4.3.1 Shift of the Dirac Voltage with Ionic Strength Change

Figure 4.4(b) shows the measured conductance of an epitaxial graphene SGFET as a function of gate voltage for several KCl salt solutions [20, 50, 100, 200, 500, 1000 mM]. The $G(V_g)$ curves display a high degree of symmetry around $V_{g,min}$ over the measured V_g range. The $V_{g,min}$ shifts towards zero as the ionic strength is increased. The observed shift with increasing KCl concentration is consistent previous experimental observations [12, 29] and can be explained using the models discussed in Sections 4.2.1 and 4.2.2 (see also [29, 6]). The positive $V_{g,min}$ at low ionic strength indicates that the processed graphene is p-doped. At the Dirac voltage graphene carries an additional negative charge in the aqueous solution (to bring the Fermi level to the Dirac point). The observed shift indicates that this negative charge increases in magnitude as gating solutions with higher concentrations of salt are used. In other words, the effect of increasing the salt concentration is to n-dope the sample. This observations are consistent with the calculations for the charge presented in Section 5.2.

The conductance $G(V_g)$ data in Figure 4.4(b) were extracted from time-dependent measurements of the graphene conductance obtained while stepping V_g like those shown in Figure 4.4(a). Each gate voltage was applied for 30 seconds, more than enough time for the

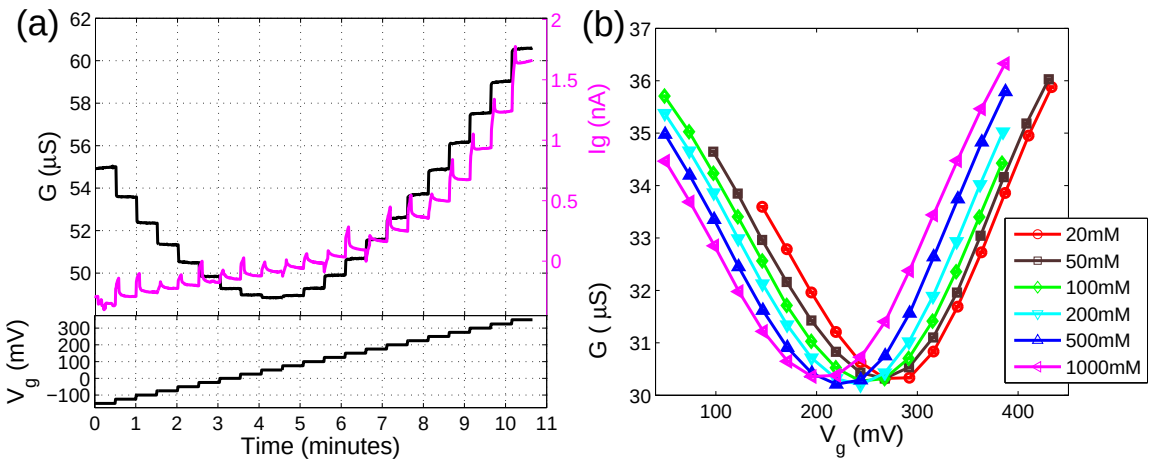

Figure 4.4: (a) Leakage current and graphene strip conductance as a function of time as the gate voltage (V_g) is stepped with KCl at 500mM. For this experiment the value of the gate is held for 30 seconds in steps of 20 mV. (b) Graphene strip conductance versus reference electrode gate voltage, V_g, measured for different KCl solution concentrations.

conductance value to stabilize. The corresponding conductance G for each gate voltage was calculated averaging the final 15 seconds of data (the conductance's transient state lasts about 5 seconds). After changing the gate voltage in steps of 20 mV the conductance changes almost instantaneously and there is a spike in the leakage current. After a few seconds the leakage current reaches an steady state value that depends on the gate voltage.

Although at a first glance the conductance plots look identical for every ionic strength there is small variation of the conductance plot for different ionic strength values. This is expected as it can be seen in Figure 4.3 the carrier density is very similar for small gate displacements from $V_{g,min}$ for the salt concentrations used. The divergence between the carrier densities is not very big even for gates 250 mV away from the Dirac gate voltage. As it will be analyzed in a later section these small differences can be analyzed to extract information about the surface charge for each ionic strength value.

In Figure 4.5, we show the dependence of the Dirac voltage ($V_{g,min}$) on the salt concentration in the solution as measured with bare and reference electrodes. The slope of these data is often referred to as the 'sensitivity' of the graphene device [38] and it is reported to characterize its performance. To implement the models discussed in Sections 4.2.1 and 4.2.2 first we do a semi-logarithmic linear best fit (in a least-squares sense) of $V_{g,min}$

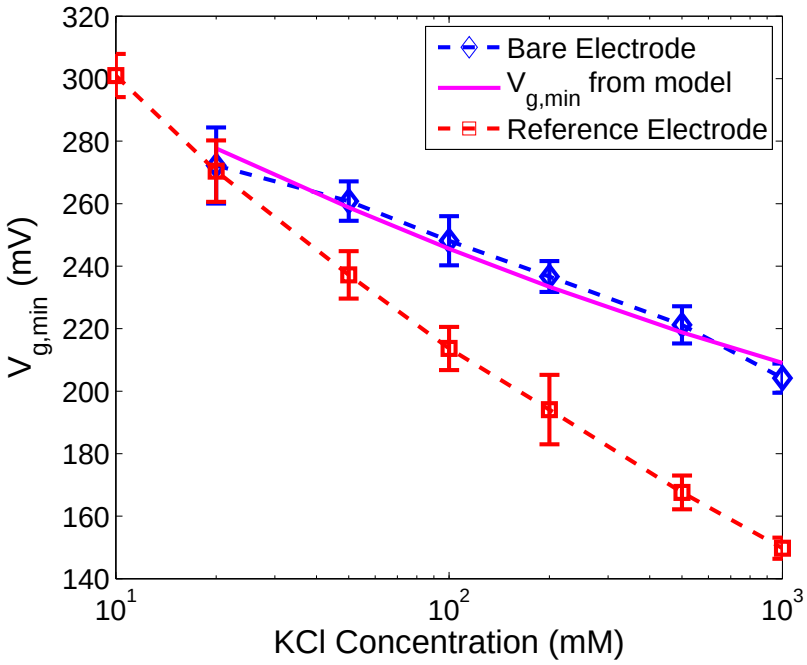

Figure 4.5: Threshold gate voltage ($V_{g,min}$) versus KCl concentration for an EG SGFET. Results for a bare and a reference gate electrode. A line showing the results fitting the experimental results to the models introduced in Sections 4.2.1 and 4.2.2 is also shown

versus the salt concentrations c^{∞}. From this fit we find a sensitivity $dV_{g,min}/d(log_{10}(c^{\infty}))$ and the projected value for $V_{g,min}$ at $c^{\infty} = 10\ mM$ ($V_{g,min}(10mM)$). In Equations (4.4), (4.11) and (4.12) $V_{g,min}$ correspond to ψ_0, and the salt concentration $c^{\infty}N_A$ to n^{∞}, we use a pKa value of 4.5 [29]. To solve them simultaneously we use a numerical algorithm that searches for the values of σ_{max} and σ_{offset} that produce values for ψ_0 for the n^{∞} used experimentally that have the same best fit parameters ($dV_{g,min}/d(log_{10}(c^{\infty}))$ and $V_{g,min}(10mM)$) found for the experimental results. From this calculation we also get values for σ_d for each salt concentration. In Figure 4.5 the values obtained for ψ_0 by this procedure are shown (magenta line). As it can be seen these values are very close to the experimental values and satisfy the sensitivity found experimentally. The values obtained for the concentration of ionizable groups and the permanent ionized groups are $\sigma_{max} = -269\ \times 10^{10} cm^{-2}$ and $\sigma_{offset} = -182\ \times 10^{10} cm^{-2}$.

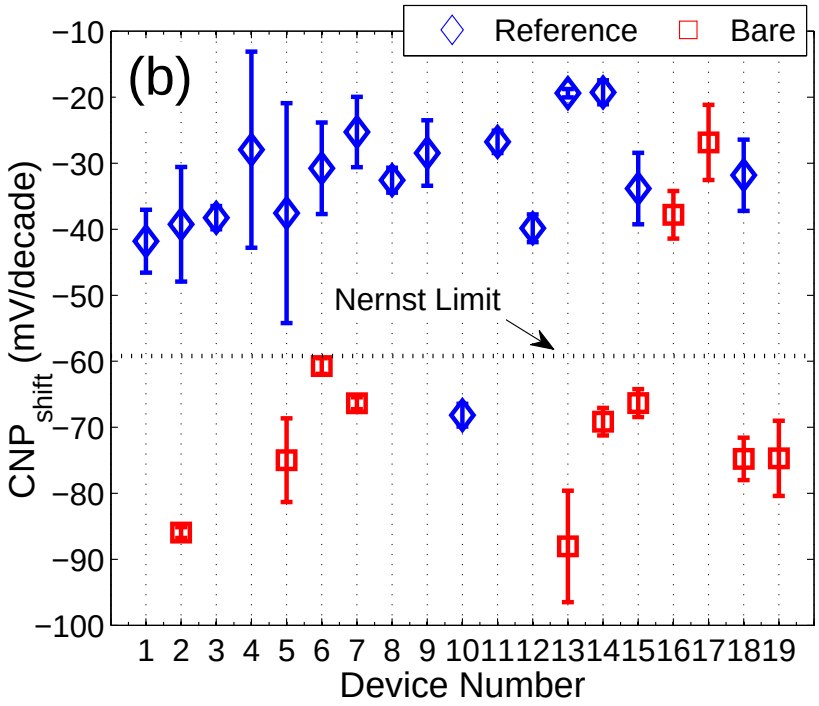

Figure 4.6: Sensitivity of the threshold gate voltage ($V_{g,min}$) for KCl concentration for other devices. These results were obtained using a bare and a reference electrode

Sensitivities are reported for several EG devices in Figure 4.6, demonstrating the consistency from device to device. The use of the reference electrode ensures a stable electrochemical environment at the gating electrode, producing sub-Nernstian sensitivities which can be explained by the basic Stern model [43]. In contrast, the sensitivities measured using the bare electrode show more variability and predominantly super-Nernstian responses (-33.8 ± 12.2 mV/decade for the reference electrode versus -66.0 ± 12.3 mV/decade for the bare electrode). This response signals a sensitivity for the interface between the bare electrode and the solution, the semi-saturated KCl solution in the reference electrode provides an stable environment for the electrode wire and the sub-Nerstian sensitivity is dependent on the graphene surface only.

Results for CVD SGFETs

A similar result for the shift of the threshold voltage with KCl concentration is obtained with CVD graphene SGFETs. Figure 4.7 shows the conductance versus gate voltage plots

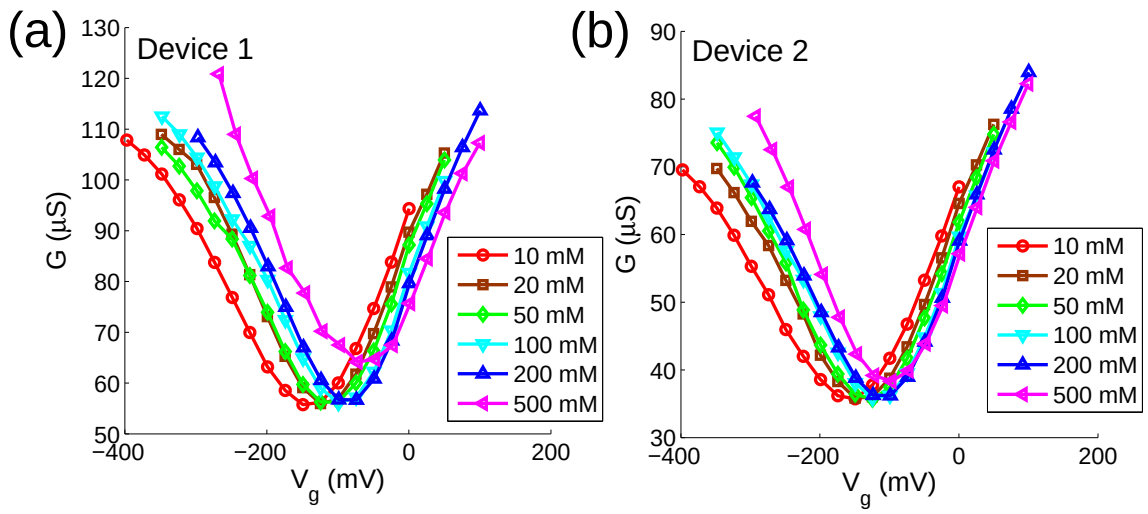

Figure 4.7: Channel conductance G versus gate voltage measured for several KCl concentrations for two CVD devices (a) Device 1, (b) Device 2.

for two devices. Figure 4.8 shows the $V_{g,min}$ shift for the CVD devices where the KCl concentration was in the range $[10mM, 500mM]$ with pH 3.2. The sensitivity of the threshold voltage is positive for this case (41.6 mV/decade and 33.3 mV/decade) but consistent with the sensitivity for EG SGFETs. This sensitivity is still sub-Nerstian consistent with the assumption that only the graphene surface is sensitive to the change in ionic strength. The difference in the direction of the shift can be attributed to the pH of the solutions used. For these samples the negative $V_{g,min}$ values correspond to n-doping. We still assume proton giving (pKa 4.5) ionizable groups at the surface that now supply less negative charge as the salt concentration increases (less n-doping for higher KCl concentration). This behavior will be discussed in Section 5.2 in terms of the surface charge calculated from the model.

4.3.2 Device performance and reversibility

After establishing the sensitivity of $V_{g,min}$ versus salt concentration, it is clear from the shift in the conductance curves that a way to do real time sensing is to set the gate voltage at an appropriate value and measure the conductance for different ionic solutions. Sensing will be facilitated by selecting a gate voltage which (a) generates low leakage currents and (b) is sufficiently far from the CNP. Low leakage currents ensure a fast and stable response to environmental changes (see Section 4.3.3) and a well chosen gate voltage ensures distinct

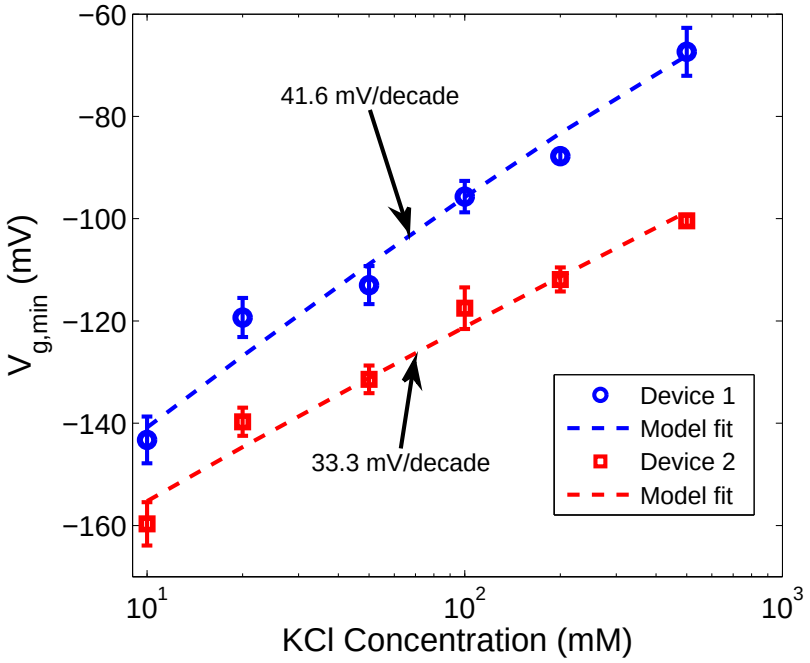

Figure 4.8: Threshold gate voltage ($V_{g,min}$) versus KCl concentration for two CVD SGFETs. A line showing the results fitting the experimental results to the models introduced in Sections 4.2.1 and 4.2.2 is also shown

conductance values and can provide a sensor whose response is linear in $\log_{10}(c^{\infty})$. This linear dependence is expected as the shift of $V_{g,min}$ is linearly proportional to $log_{10}(c^{\infty})$ as was reported in Section 4.3.1. If we work at a gate voltage that is outside the plateau for every salt solution the shift in G for a change in c^{∞} should be semi-logarithmic too.

An important factor in sensing devices is the reusability of the device. Figure 4.9(a) shows the change in a graphene device's conductance as a function of V_g for two KCl concentrations (these $G-V_g$ curves have a small $\sim$0.2 μS offset in G which is ascribed to sample aging drift). In Figure 4.9(b,c) we show the device conductance when cycling the KCl concentration. The difference between the conductances for the two solutions used exhibit reasonable consistency with the ΔG values expected from Figure 4.9(a). The differences between the values projected and measured for ΔG can be partially explained by the drift in the minimum G between the two KCl plots. If a "working" V_g is chosen which is far from $V_{g,min}$ for the desired concentration range, then a response which is semi-logarithmic in c^{∞} can be obtained as it is shown in Figure 4.10 (V_g=0). The values of $V_{g,min}$ for this

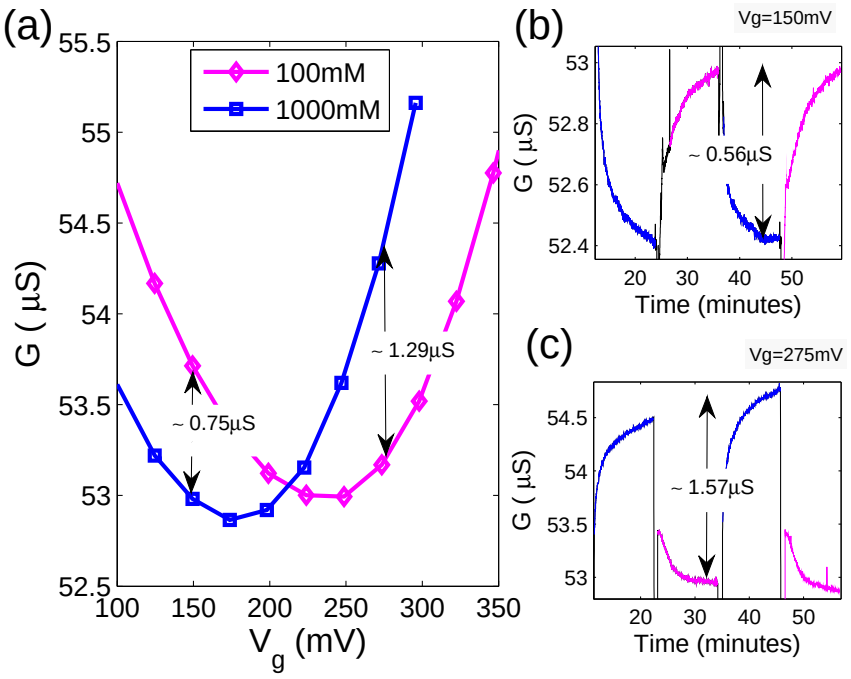

Figure 4.9: (a) Graphene conductance change versus V_g for 100nM and 1000nM KCl solutions using a bare electrode. Side panels show conductance changes under cycling the KCl solution [rather than stepping V_g as in (a)] at gate voltages below and above the minimum conductance point: (b) $V_g = 150$ mV and (c) $V_g = 275$ mV.

particular sample were in the range $[160\ mV, 320\ mV]$ so we are working away from the MCP plateau for every KCl concentration.

These results establish that the conductance of the devices are reversible when c^∞ is increased and decreased in succession and that the conductance value has a predictable dependence on c^∞ once the Dirac voltage has been established for at least two KCl concentrations and a calibration curve for G versus V_g has been obtained for a given KCl concentration.

4.3.3 Leakage Current Correlation with Device Stability

During our conductance measurements, we also simultaneously measured the gate leakage current I_g (see Section 3.3) which should be minimal for an electrostatically gated FET (<1-10nA [53]). The leakage current shows a short transient upon changing V_g, but it stabilizes in less than 30 seconds for well performing devices. The final leakage current

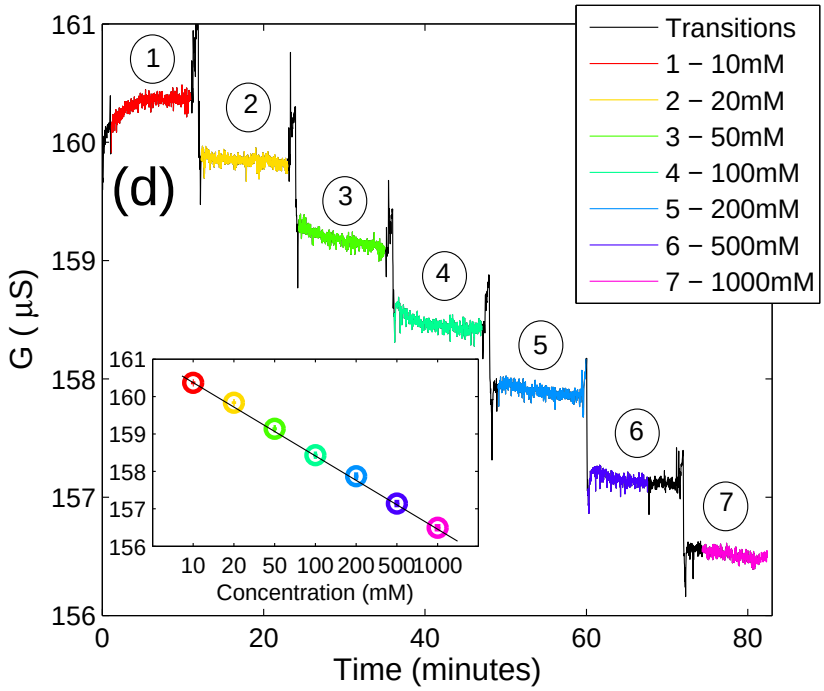

Figure 4.10: Conductance data measured in a second device at a V_g value far from the CNP ($V_{g,min} = [160 - 320]$ mV) as the KCl concentration is changed using a reference electrode. Inset shows steady values as a function of KCl concentration where the solid line is a semilog fit ($-1.94\mu S/mM$).

dependence on V_g is shown for several different devices in Figures 4.4, 4.11 and 4.13. This current is very close to zero at $V_g = 0V$ and increases non-linearly for other gate values. This increase is non-symmetric being very small for negative gate voltages and noticeable larger for positive gate values.

In our measurements, $|I_g|$ shows no clear correlation with the graphene conductance and consistently has a minimum value near $V_g \approx 0$. Furthermore, I_g versus V_g is independent of KCl concentration (Figure 4.11). The observation that leakage current is largely independent of ionic strength implies that salt concentration does not indirectly change the conditions for graphene sensing by reducing device performance. We did observe a general correlation between poorly performing devices and larger and/or unstable leakage currents. Those devices failed to stabilize quickly (or ever) in measurements of the conductance G. Indeed leakage current was a good first test to predict the performance of an newly assembled SGFET.

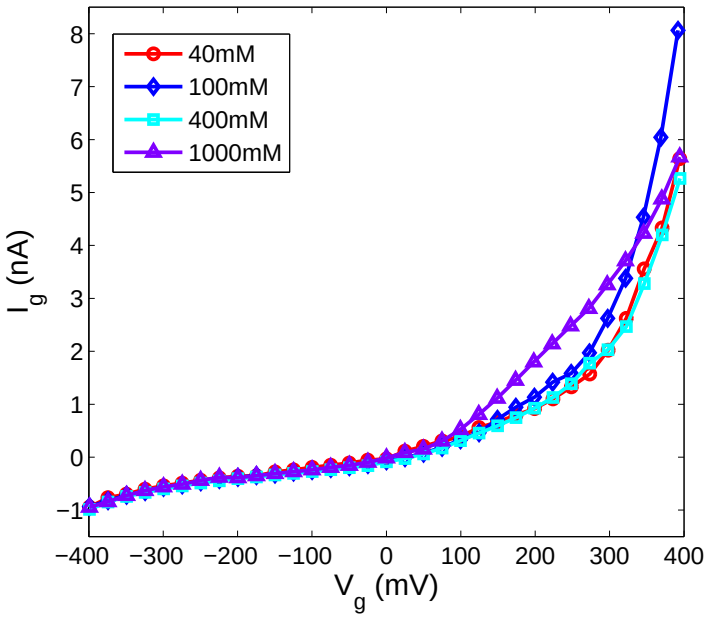

Figure 4.11: Gate leakage current for a single device at different IS values

To characterize poorly performing devices a set of experiments was carried out in a device that had increased leakage due to aging. A usual mode of failure for a device involves an aging period in which the leakage current increases gradually until it doesn't work any longer when a contact breaks. Usually the current does not increase enough to affect the performance of the device before it breaks, but a few devices last longer than usual and their performance suffers. We have been able to connect this performance loss to the leakage current.

In Figure 4.12 the leakage current time evolution is shown for a well performing device and a device with higher leakage current for several time delays between gate voltage changes. Figure 4.12(a) shows the leakage time response for a low-leakage-current (low-leak) device with a delay of 20 seconds between gate changes and a high-leakage-current (high-leak) device for several delay times (30, 60, and 120 seconds). The gate voltage was swept between $-200\ mV$ and $300\ mV$ in steps of $25\ mV$. To have a clearer picture of the difference in the leakage behavior between low-leak and high-leak devices Figure 4.12(b) shows two extracted plots taken with similar delay times. It is apparent that the high-leak device takes a longer time to reach an steady current. The same gate voltages were used

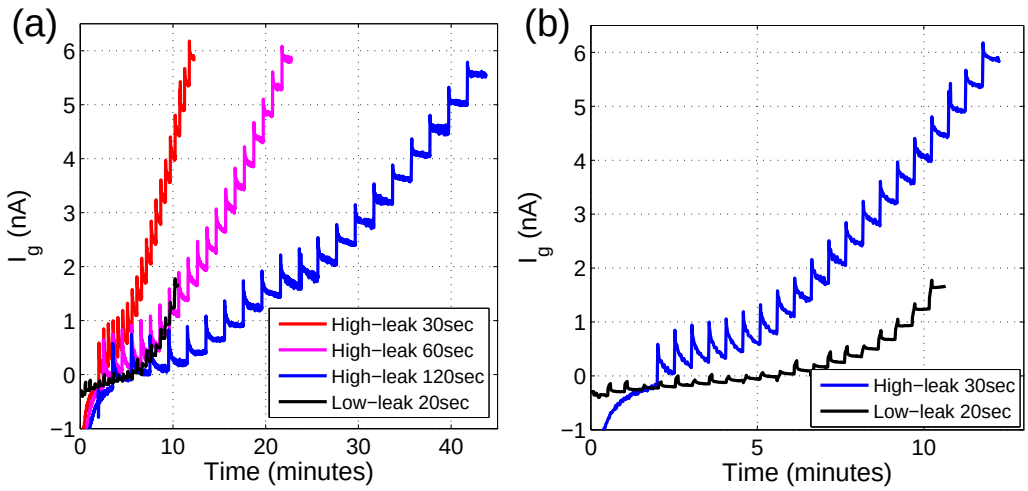

Figure 4.12: Gate leakage current time evolution for devices with small leakage current (low-leak) and with bigger leakage current (high-leak) (a) Using different delay times between gate changes. (b) Selection of two plots from (a) with similar delay times

for the high-leak device in its three cases (30, 60, and 120 seconds) and we see that the final leakage currents are very reproducible. But in the high-leak device the waiting time before reaching a steady state is longer (larger than 120 seconds). The final values for a low-leak and a high-leak device are shown in Figure 4.13. For the high-leak device the final leakage is very close to its final value for 30 seconds and it is slightly smaller for 60 and 120 seconds. But as it will be seen in the following analysis this higher leakage leads to a slower convergence for the conductance.

There is also a longer stabilization time for the value of the conductance for the high-leak device. In order to estimate this times the following treatment have been done to the conductance time evolution. The data for each transition has been shifted to start at zero and its has been scaled so that the final value for the conductance is ± 1. After these transformations the time evolution of the conductance after changing the gate can be grouped in two regimes (see Figure 4.14). When the gate voltage is below $V_{g,min}$ (holes regime) the sample takes a longer time to get to an stable conductance. The averaged time behavior is shown in the black (dash and continuous) lines. When $V_g > V_{g,min}$ (electron regime) the transient is shorter for both the high-leak and the low-leak sample with respect to the transient for holes. It can be seen from these data that for each regime the transient for

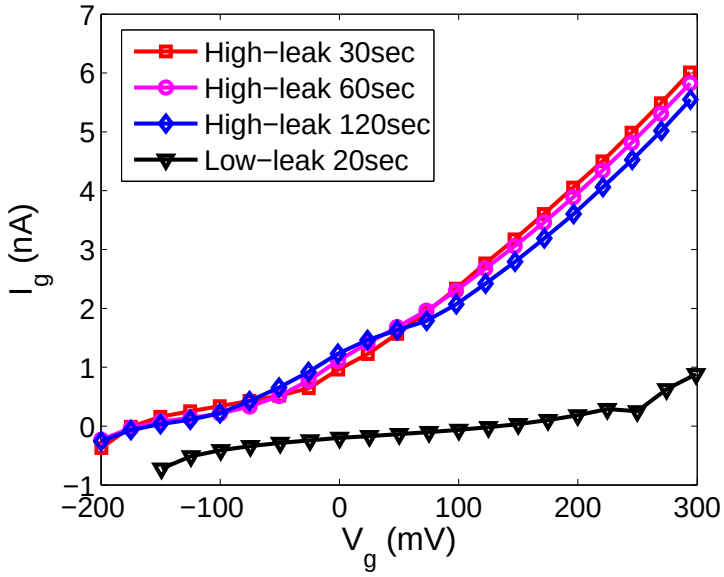

Figure 4.13: Gate leakage current for devices with small leakage current (low-leak) and with bigger leakage current (high-leak)

the low-leak sample is shorter than the transient for the high-leak one. This in conjunction with the data in Figures 4.11 and 4.13 shows that a sample with high current leakage will have longer transient times after a change in the gate value.

To further explore the transient time for the high-leak sample some experiments were carried out using the same KCl concentration (10mM) and the same range of gate voltages to monitor the change in conductance while keeping the gate voltage constant for different times: 30, 60, and 120 seconds. For these experiments the same two regimes (electron and hole dominated conductance) were found to give different behaviors. The same adjustments were made to the conductance versus time data to estimate the transient times. For this case only the average curve is plotted for each case. For the hole conductance region (see Figure 4.15) the transient time is longer than 120 seconds while the transient seems to be close to 60 seconds for the electron regime.

4.4 Conclusions

For the first time, we have characterized the electrical response of EG and CVD SGFETs to changes in the ionic strength with KCl in DI water for two pH values. Starting from EG and CVD wafers of similar dimensions, the same fabrication process was used for EG and

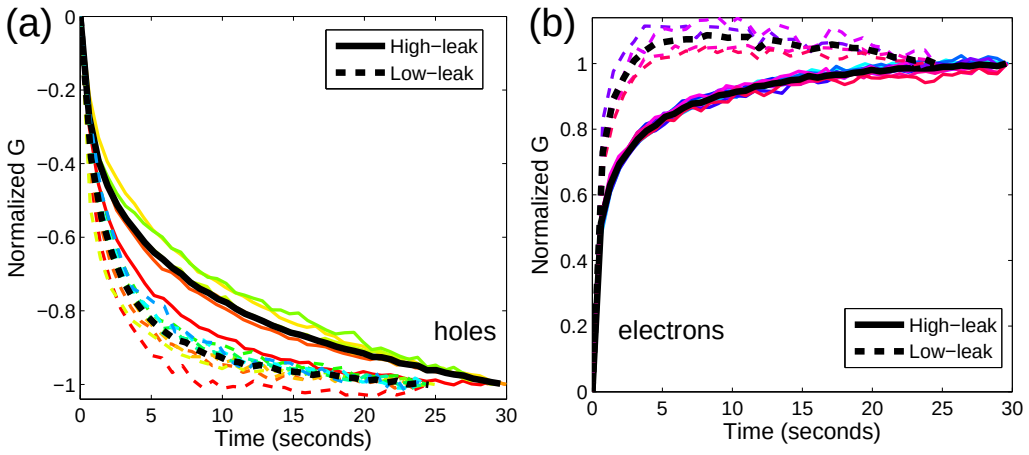

Figure 4.14: Comparison of a device with small leakage current (low-leak) with a device with bigger leakage current (high-leak). Normalized and shifted conductance versus time for (a) gate voltages in the hole dominated conductance (b) gate voltages in the electron dominated conductance. The averaged time evolution is plotted in black lines.

CVD devices. We found that EG and CVD s have very similar response to ionic strength changes indicating that graphene's properties are reproducible across different substrates and synthesis methods.

The results for the shift of $V_{g,min}$ with the change in c^{∞} can be explained with a model that couples the physics of the EDL with a ionization of surface groups present at the graphene. The model also gave us an estimation of the density of ionizable groups σ_{max} and the density of charges that are not affected by the salt solution σ_{offset}. For the calculation of these values we assumed the same type of ionizable groups for both pH values and corroborated that they give values for the surface charge consistent with the experimental results as will be explained in Chapter 5. The attribution of the origin of the ionizable groups to the device fabrication process is confirmed by the fact that the same type of group can be assumed in our models for graphene of different synthetic origin (EG or CVD).

The EG devices have reversible conductance when the salt concentration is increased or decreased. The conductance versus V_g curves provide a guide for the calibration of the device. They also give information about the optimal choice for the gate voltage in a device. It is apparent that a gate voltage that induces holes is preferable as the leakage

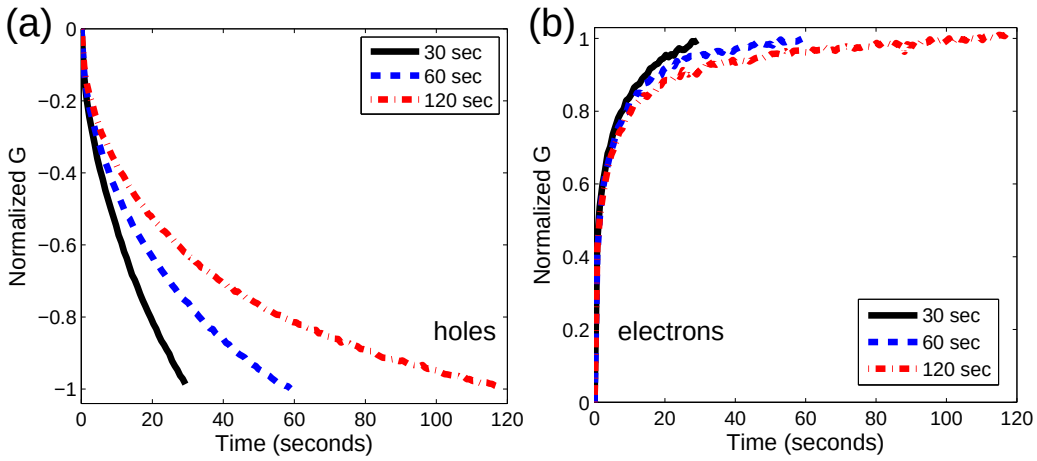

Figure 4.15: Comparison of high-leak sample for different delay times between gate changes. Normalized and shifted conductance versus time for (a) gate voltages in the hole dominated conductance (b) gate voltages in the electron dominated conductance. The averaged time evolution is plotted in black lines.

current is smaller in this regime for well and poorly performing devices. The sensitivity of the conductance versus ionic strength for a fixed gate voltage is consistent with the conductance versus V_g experimental curves.

The leakage current I_g is a good indicator for the device quality. Devices with a low I_g value show a faster response after the gate voltage is changed. For poor performing devices the response is slower despite the fact that the leakage current reaches its steady-state value fast. The different behavior for the leakage current in general and the steady-state response of the conductance for the electron and the hole regimes in EG need further exploration.

For EG devices the sensitivity of the Dirac voltage to the ionic strength is supra-Nerstian when a bare electrode is used as a gate. This can be explained considering that an electrical double layer (EDL) that is dependent of the salt concentration c^{∞} is present at the gate electrode when this electrode is in direct contact with the solution. This has to be accounted when the use of a reference electrode is not possible. The sub-Nerstian sensitivity found when a reference electrode is used for gating is consistent with the EDL model as in this case only the EDL at the graphene is sensitive to the solution.

CHAPTER V

ROLE OF SURFACE CHARGE AND IMPURITIES IN GRAPHENE SGFETS

5.1 Introduction

The physics of sensing for SGFETs relies on the surface charge. This surface charge is a superposition of permanently charged impurities and other impurities that correspond to ionizable groups. How they may work together to influence the conductivity of the devices is not fully understood and it has been suggested that they may be correlated [1, 12]. In this chapter we continue our analysis of the data reported in Chapter 4. In that chapter we presented our experimental results and focused on the performance and reliability of graphene SGFETs in ionic solutions. This chapter will focus first on what the models we use to analyze our data tell us about the surface ionization dependence on the ionic concentration and the pH of the solution.

Using the electrical double layer and the surface ionization models introduced in Sections 4.2.1 and 4.2.2 we estimate the surface charge for several salt concentrations for several experiments with EG and CVD devices in Section 5.2. These estimated values provide a clear picture about the contributions of the ionizable groups and the permanent charges to the net surface charge. We also calculate the fraction of the total ionizable groups that are ionized at each ionic strength.

Then, we use two theoretical approaches to estimate the concentration of charged impurities n_{imp} for our samples. One is the self-consistent approximation (SCA) introduced by Adam [1]. This calculation estimates the impurities of a given sample from the conductance data and it has not been used before for SGFETs. Tan [71] and Chen [12] have used the conductance versus carrier density curve to estimate the impurities in their samples using Equation (2.44). Chen obtains values for SGFETs for the concentration of impurities

n_{imp} spanning two orders of magnitude from $\sim 10^{12}\ cm^{-2}$ to $\sim 10^{13}\ cm^{-2}$. These estimations were performed in an ionic liquid providing one estimated value for each device. We use the same approach to calculate values for the impurities at several salt concentrations. Tan gets impurities for graphene FETs in the range $[2,5]\times 10^{11}\ cm^{-2}$.

An estimation of the impurities at different salt concentrations for a particular sample using the SCA is presented in Section 5.3. In Section 5.4 the impurities for the same case considered in the two previous sections is calculated from the conductance versus carrier density curves. The values obtained for the net surface charge and the impurities are compared in Section 5.5.

5.2 Estimation of Ionizable Surface Charges Using Solution Gating Model

Two models, one for the electrical double layer, that describes the ion distribution inside the liquid solution, and another for the protonation of surface functional groups, that describes the ionizable groups in the graphene surface, have been introduced in Sections 4.2.1 and 4.2.2. The implementation details to get information about the surface charge from them was explained in Section 4.3.1. Starting from the experimental Dirac voltages $V_{g,min}$ for every salt concentration c^{∞}, the numerical self-consistent solution of Equations (4.4), (4.11) and (4.12) gives the values for σ_{max}, σ_{offset}, and the values for the total surface charge σ_d for every concentration. The values obtained from the models for $V_{g,min}$ are close to the actual experimental values (see Figures 4.5 and 4.8).

The experimental results given in Section 4.3.1 show results for two different pH values and devices with different doping levels. For the case of the EG device, the sample is p-doped and the Dirac voltage shift towards zero suggests that the surface charge decreases for increasing ionic strength. The calculations from the models gave values for the concentration of ionizable groups ($\sigma_{max} = -269\ \times 10^{10} cm^{-2}$), and the concentration of permanent ions that are independent of the solution ($\sigma_{offset} = -182\ \times 10^{10} cm^{-2}$). The total possible concentration of ions in the surface is $\sigma_{total} = \sigma_{max} + \sigma_{offset} = -451\ \times 10^{10} cm^{-2}$. The ionic surface concentration for each KCl concentration value for the EG experiment is given in Table 5.1.

Table 5.1: Calculated total surface charge and charge from ionizable groups for an EG device

KCl conc (mM)	σ ($\times 10^{10} cm^{-2}$)	σ_{ion} ($\times 10^{10} cm^{-2}$)	$\sigma_{ion}/\sigma_{max}$ (%)
20	-196.9	-15.1	5.62%
50	-204.1	-22.3	8.31%
100	-211.4	-29.5	11.00%
200	-220.3	-38.5	14.33%
500	-234.9	-53.1	19.76%
1000	-248.0	-66.2	24.63%

In Table 5.1 the fraction of the charge that corresponds to ionizable groups ($\sigma_{ion} = \sigma - \sigma_{offset}$) is given and the percentage of ionized groups is given. The projected negative charges increase with higher salt concentration. This is consistent with the picture given in Section 4.3.1 where higher negative charge is needed to add n-dopants to an already p-doped sample to bring a positive Dirac voltage closer to zero. The percentage of ionized species suggests that the sample can be sensitive to KCl concentrations outside the range tried experimentally. For example, for a KCl concentration of 1mM the estimated fraction of ionized groups is 1.40%. And for 2M, 30.1% of the groups are expected to be ionized.

For the two CVD devices (see Figure 4.8) the same calculation process can be applied. These samples were n-doped (negative $V_{g,min}$) for the lower ionic strength and $V_{g,min}$ shifted to zero for increasing KCl concentration. This indicates a lower n-doping level (or higher extra p-doping, but the other case makes more sense in the current situation) and so a less negative surface density is expected when the salt concentration increases. This expectation matches the result obtained for the two devices as it is seen in Table 5.2. For the device 1, $\sigma_{max} = -32.1 \times 10^{10} cm^{-2}$ and $\sigma_{offset} = 62.8 \times 10^{10} cm^{-2}$. Because σ_{offset} is positive and bigger than σ_{max} all the surface charges at $V_{g,min}$ are positive. This is consistent with p-doping. But there is always a fraction of ionized charges and their fraction decreases from $\sim 71\%$ to $\sim 35\%$.

For device 2, $\sigma_{max} = -97.9 \times 10^{10} cm^{-2}$ and $\sigma_{offset} = 122.4 \times 10^{10} cm^{-2}$. This device has a very similar behavior to the other CVD device. The higher magnitude of the projected charges is consistent with higher doping, but the percentage change in the ionized charge is

similar to the other device.

Table 5.2: Calculated total surface charge and charge from ionizable groups for two CVD devices

CVD	Device 1			Device 2		
KCl conc (mM)	σ ($\times 10^{10} cm^{-2}$)	σ_{ion} ($\times 10^{10} cm^{-2}$)	$\sigma_{ion}/\sigma_{max}$ (%)	σ ($\times 10^{10} cm^{-2}$)	σ_{ion} ($\times 10^{10} cm^{-2}$)	$\sigma_{ion}/\sigma_{max}$ (%)
10	40.01	-22.78	70.95%	49.06	-73.34	74.92%
20	42.04	-20.75	64.63%	53.91	-68.49	69.96%
50	44.92	-17.87	55.67%	61.01	-61.39	62.71%
100	47.11	-15.68	48.83%	66.77	-55.63	56.83%
200	49.20	-13.59	42.34%	72.67	-49.73	50.79%
500	51.60	-11.19	34.87%	80.31	-42.09	42.99%

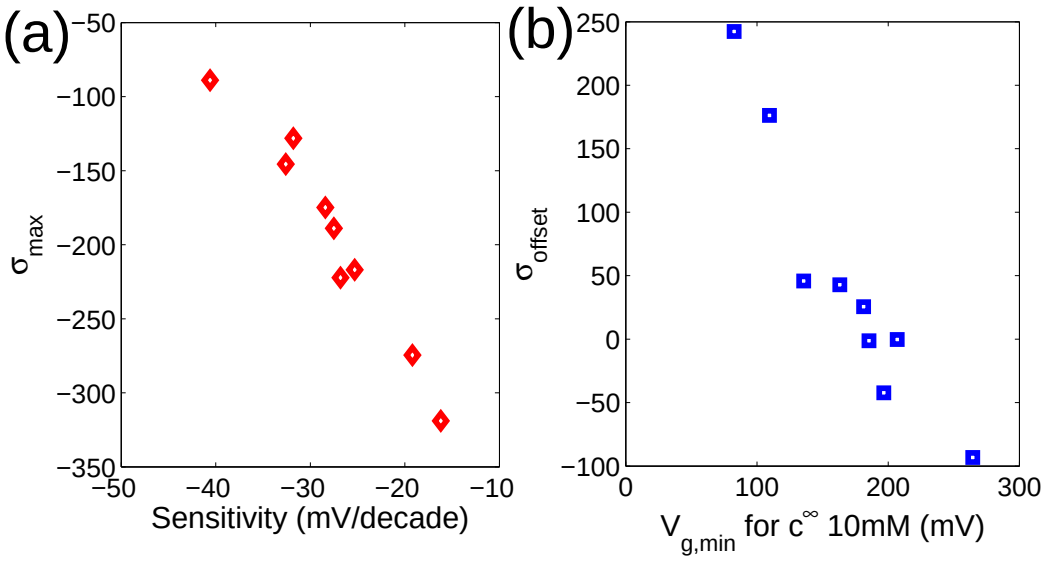

Figure 5.1: (a) Comparison of the values for sensitivity with concentration of ionizable groupsσ_{max} (b) Comparison of $V_{g,min}$ with σ_{offset}

Table 5.3 shows the estimated values for σ_{max} and σ_{offset} for other EG devices with different sensitivities and $V_{g,min}$ values at 10mM. σ_{offset} depends on the position of $V_{g,min}$ being more negative for higher $V_{g,min}$ values. σ_{max} appears to be more related to the sensitivity being smaller for higher sensitivities (see Figure 5.1). Having less ionizable groups seems to be the key for higher sensitivity.

Table 5.3: Surface charge model results for several EG devices

Sample No.	σ_{max} ($\times 10^{10} cm^{-2}$)	σ_{offset} ($\times 10^{10} cm^{-2}$)	$V_{g,min}$ (mV) at 10mM	Sensitivity (mV/decade)
1	-88.9	-42.2	196.7	-40.6
2	-188.9	25.6	181.3	-27.5
3	-216.9	-0.24	206.9	-25.3
4	-145.6	-1.33	185.4	-32.6
5	-174.8	42.8	163.2	-28.4
6	-222.3	-93.2	264.5	-26.8
7	-318.9	242.3	82.6	-16.2
8	-274.5	176.2	109.6	-19.2
9	-128.0	45.7	135.6	-31.8

5.3 Estimation of Impurities Using the Self Consistent Approximation

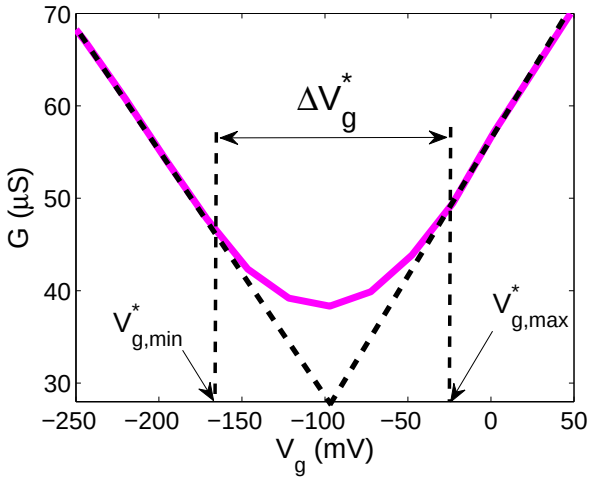

Figure 5.2: Illustration for the estimation of the residual carrier density from experimental data.

It has been shown in the literature that the conductivity values obtained in most of the experiments with graphene can only be explained by the presence of charged impurities [1] (see Section 2.4). For a small quantity of impurities (also referred to as long-range scatterers) the relation between conductance and carrier density is expected to be linear for all carrier densities. In most experiments, a semi-parabolic plateau is observed around the MCP like the data shown in Figure 4.4(b). It has been predicted theoretically [1] and verified experimentally [14] that impurities are responsible for this plateau in the conductance curve.

Using the plateau width in a conductance versus gate voltage plot the residual carrier density n^* can be estimated as half of the width of the plateau. n^* was introduced in Section 2.4.3 as the carrier density present near the Dirac voltage that is induced by the impurities n_{imp} in the graphene. The plateau estimation is illustrated in Figure 5.2. The two gate voltages ($V^*_{g,max}$,$V^*_{g,min}$) where the conductance is not linear any longer are identified. Then $\Delta V^*_g = V^*_{g,max} - V^*_{g,min}$ is calculated as the width of the plateau. Then $\Delta V^*_g/2$ is used as $|V_g - V_{g,min}|$ in Equation (4.13) to obtain n^*.

The self consistent approximation (SCA) formalism explained in Section 2.4.3 [1, 64] is used to obtain an expression that relates the residual carrier density n^* to the concentration of impurities n_{imp} on the sample.

$$\frac{n^*}{n_{imp}} = 2r_s^2 C_0^{RPA}(r_s, 4d\sqrt{\pi n^*}) \tag{5.1}$$

where $C_0^{RPA}(r_s, 4d\sqrt{\pi n^*}$ (see Equation (2.53)) is the correlation function from the random phase approximation (RPA) used to calculate the conductivity and d ($\sim$ 1 nm) is the average distance from the impurities to the graphene plane.

Table 5.4: Estimated impurities for different KCl concentrations using the SCA. These results correspond to the EG device analyzed in Section 5.2

KCl conc (mM)	n^* ($\times 10^{12}$ cm^{-2})	n_{imp} (SCA) ($\times 10^{12} cm^{-2}$)
20	0.327	1.604
50	0.430	2.317
100	0.429	2.310
200	0.462	2.558
500	0.399	2.097
1000	0.410	2.175

For the data shown in Figure 4.4(b) the values estimated for the densities are $n^* = 0.327 \times 10^{12}$ cm^{-2} and $n_{imp} = 1.604 \times 10^{12}$ cm^{-2} at 20 mM. n_{imp} scales roughly as n^{*2} so the estimated density of impurities will be higher for wider plateaus. We had a few samples with wider plateaus in their G versus V_g plot. For a sample with $n^* = 1.42 \times 10^{12}$ cm^{-2} we obtain $n_{imp} = 12.4 \times 10^{12}$ cm^{-2}. On average for ten samples we get $n_{imp} = 6.15 \times 10^{12}$ cm^{-2} which corresponds to charged impurity levels typical for current standard microfabrication

processes [1] and is very close to the value obtained by [12] using a different approach.

Table 5.5: Impurities estimated using the SCA for some EG SGFETs for a particular KCl concentration

Sample No	KCl concentration (mM)	n^* ($\times 10^{12}$ cm^{-2})	n_{imp} ($\times 10^{12}$ cm^{-2})
1	40	0.860	6.035
2	40	0.966	7.116
3	40	0.588	3.557
4	20	1.254	10.345
6	20	0.786	5.317
6	20	0.221	0.955
7	20	0.327	1.604
8	20	0.949	6.942
9	20	1.421	12.404
10	100	1.046	7.967

For a given device there is some variation in the plateau width for different KCl concentrations and impurities can be estimated for each case. In Table 5.4 the estimated impurities in the sample considered are shown for all ionic strength values for the EG device analyzed in Section 5.2. There impurities calculated increase with increasing ionic strength. These values will be compared with the estimated surface charge values and other calculation of the impurities in Section 5.5. The estimated values of n^* and n_{imp} for some samples are shown in Table 5.5 for a low ionic strength.

5.4 Estimations of Impurities from The Conductance at High Carrier Density

The conductance model for high carrier density described in Section 2.4.2 also gives a prescription for a calculation of the impurities. In Section 2.4.2 an equation for the conductivity is obtained assuming that the dominant process for carrier conduction is the scattering by Coulomb impurities. We reproduce this result here for convenience. The conductivity is

$$\sigma(n) = \frac{e^2\, n}{h\, n_{imp}} \frac{2}{G(2r_s)} \tag{5.2}$$

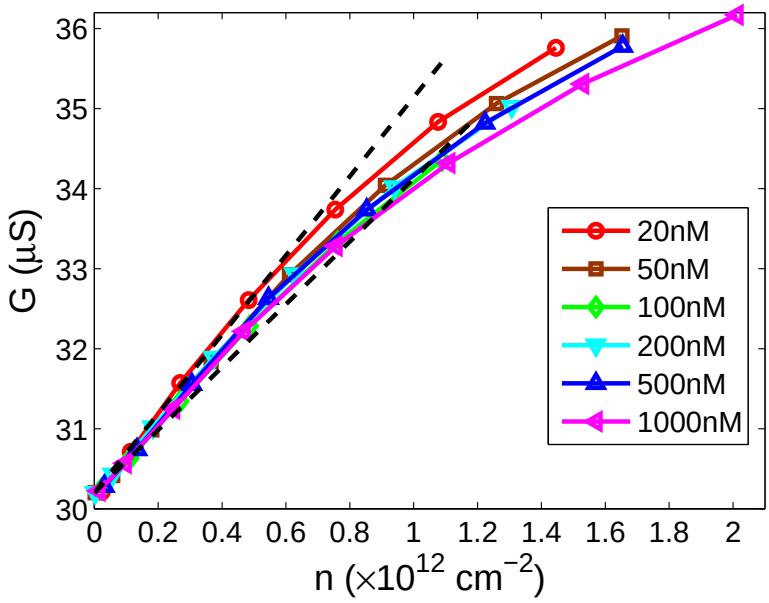

Figure 5.3: Conductance versus carrier density plots obtained from the data in Figure 4.4(b).

where n is the surface carrier density and n_{imp} is the density of impurities. If we have a good estimation for the Wigner-Seitz radius r_s we can calculate the factor $2/G(r_s)$ (see Equation (2.45) and the discussion after them in Section 2.4.2 to see how this factor is calculated). For graphene over SiO_2 this factor is 20 and for EG over SiC its value is 25. The conductivity obtained in the calculation corresponds to the inverse of sheet resistance. For a rectangular sample the conductance G is related to the sheet resistance by,

$$G = \sigma(n)\frac{W}{L}, \tag{5.3}$$

where L,W are the length of the rectangle along the current direction and the width.

Equations (5.2) and (5.3) give an expression for the conductance

$$G(n) = \frac{e^2\, n}{h\, n_{imp}} \frac{2}{G(2r_s)} \frac{W}{L}. \tag{5.4}$$

For our EG and CVD samples we have $W/L = 0.3$. Inserting all the known values in Equation (5.4), we get the following numerical expressions for the conductance

$$G(n) = \begin{cases} 290\mu S \times \frac{n}{n_{imp}} & : \text{for EG}, \\ 232\mu S \times \frac{n}{n_{imp}} & : \text{for CVD}. \end{cases} \tag{5.5}$$

And for the impurities we get,

$$n_{imp} = \begin{cases} \frac{290\mu S}{dG(n)/dn} & : \text{for EG,} \\ \frac{232\mu S}{dG(n)/dn} & : \text{for CVD} \end{cases} \tag{5.6}$$

with $G(n)$ given in μS.

To estimate n_{imp} using our experimental results (see Figure 4.4(b)) we need plots of G versus the density of carriers n. The G versus V_g plots for different KCl concentrations can be transformed into G versus n plots using Equation (4.13). Using this equation the plots in Figure 5.3 were calculated. In these plots there is a linear region for small carrier densities ($n < 0.4 \times 10^{12} cm^{-2}$). This region can be analyzed to get an estimation of n_{imp}.

5.5 Comparison of Estimated Impurities with the Surface Charges Calculated from the Shift in the Dirac Voltage

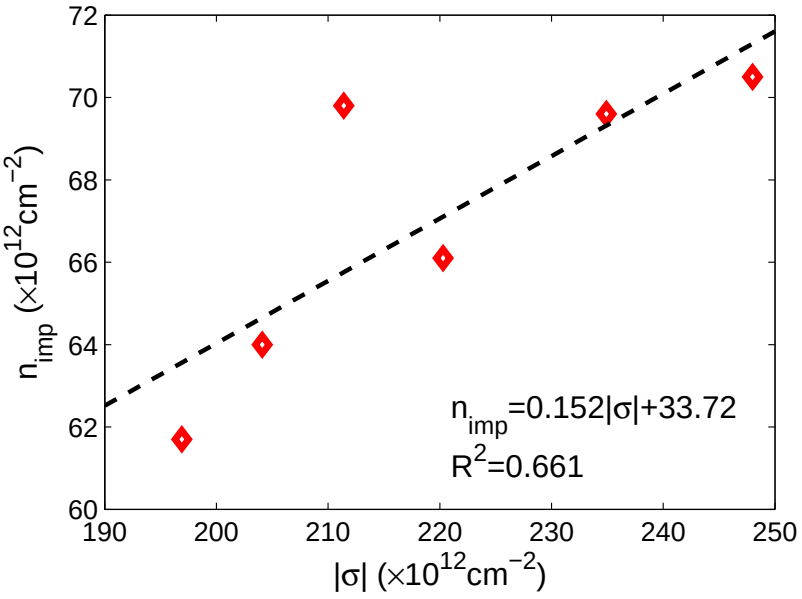

Figure 5.4: Impurities calculated from dG/dn for all ionic strengths versus the surface charge obtained from the surface charge model using the G versus V_g data

The estimated impurities, from the data shown in Figure 5.3, are shown in Table 5.6. In the same table the surface charges estimated from the same data and the impurities estimated using the SCA are shown. In Figure 5.4 the impurities estimated from the

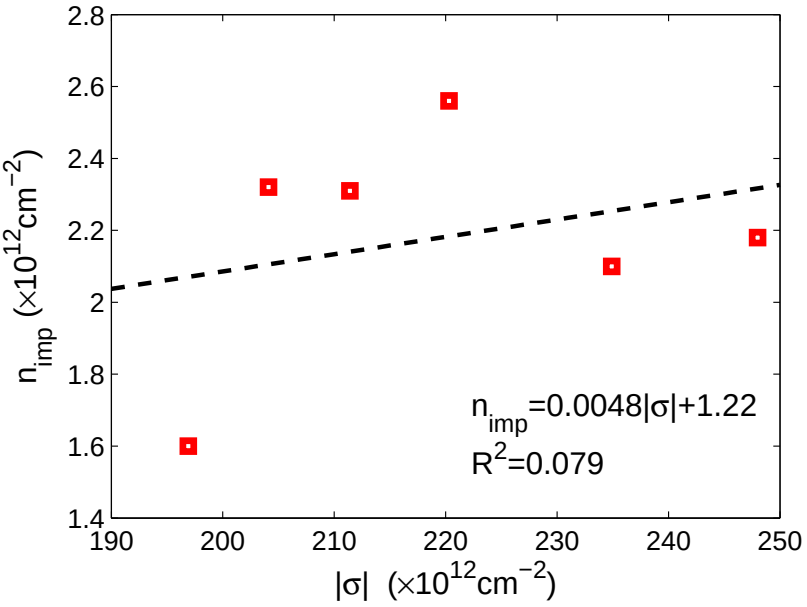

Figure 5.5: Impurities calculated from the SCA for all ionic strengths versus the surface charge obtained from the surface charge model using the G versus V_g data

G versus n plots are shown versus the surface charge obtained from the EDL-surface-ionization model for all the KCl concentrations. The two charges have a certain amount of proportionality to each other. They are not perfectly proportional as the fitted line does not cross the y-axis at the origin so there is not a one-to-one correspondence between them. But the change in the estimated impurities with ionic strength suggests that the new impurities come from the surface charges that work as charged scatterers.

Table 5.6: Estimated surface charges and impurities for different KCl concentrations. The impurities were estimated using the SCA and G versus n plots. These results correspond to a particular EG device

KCl conc (mM)	$\lvert\sigma\rvert$ ($\times 10^{12} cm^{-2}$)	n_{imp} (SCA) ($\times 10^{12} cm^{-2}$)	n_{imp} (G vs n) ($\times 10^{12} cm^{-2}$)
20	196.9	1.604	61.7
50	204.1	2.317	64.0
100	211.4	2.310	69.8
200	220.3	2.558	66.1
500	234.9	2.097	69.6
1000	248.0	2.175	70.5

In Figure 5.5 the impurities estimated with the SCA are shown versus the surface charge

obtained from the EDL-surface-ionization model. These impurities are uncorrelated to the surface charge. This suggests that the impurities estimated from the SCA model may not be related to the ionizable groups and the origin of the plateau in the G versus V_g (and G versus n) plots are permanently ionized impurities. In this scenario only the permanently charged impurities would be responsible for the induction of the electron and hole puddles at the Dirac point.

5.6 Conclusions

Assuming acidic ionizable groups (pKa 4.5) at the graphene surface for EG and CVD SGFETs the surface charge densities were estimated using the EDL model that explains the electrostatic configuration of ions in the bulk of the liquid and a ionization model that covers the behavior of the charged groups at the graphene's surface. The experiments analyzed covered two pH values (5.2 and 3.2). For pH 5.2 the total ionized negative charge grows with increasing salt concentration and the shift of $V_{g,min}$ corresponds to a higher n-doping. The opposite effect is observed for pH 3.2 corresponding to a decrease of the n-dopants for increasing ionic strength. The experiments considered CVD and EG devices made with the same fabrication method (see Section 3.2) justifying the assumption of the same type of ionizable groups. For the two CVD devices at the same pH the magnitude of the charges were different and consistent with n-doping. But the fraction of ionized groups of the total ionizable groups was similar for both cases that had similar sensitivity.

From an analysis done over nine devices (see Table 5.3) it appears that the values of the permanent charge σ_{offset} are related to the doping of the graphene. The surface concentration of ionizable groups σ_{max} is smaller for higher sensitivity devices and viceversa. It seems that a smaller density of ionizable groups leads to higher sensitivity of $V_{g,min}$ to the ionic strength. This result can be applied to the design of future graphene sensors in liquids where the sensitivity of a device can be adjusted by the control of the impurities added to the graphene channel.

There is an apparent relation between the total ionized charge for each concentration and the impurities estimated from the G versus n curve. This correlation suggests that the

ionized surface groups in the graphene play a role in its conductivity for high carrier density values. There is no correlation between the total ionized charge for each concentration and the impurities estimated using the SCA approximation. This indicates that the impurities responsible for the plateau in the conductance curves do not correspond to the ionizable groups. The SCA impurities had values that were an order of magnitude smaller that those estimated by the analysis of the conductance curves and the projected surface charges. This also indicates that the impurities estimated by those methods are of different nature.

CHAPTER VI

ROLE OF ELECTROSTATICS AND CHARGE IN PROTEIN SENSING WITH SGFETS

6.1 Introduction

Ultimately our investigations into graphene-based SGFETs are aimed to understand how to take advantage of graphene's unique physical properties in order to optimize sensing. In particular, liquid sensors of chemical species and biomolecules are of great interest. In this chapter, we take a step back to fundamentals from the experimental engineering of sophisticated graphene-based SGFETs that others are pursuing in order to test our understanding of how proteins interact with graphene SGFETs and how they alter the measured conductance.

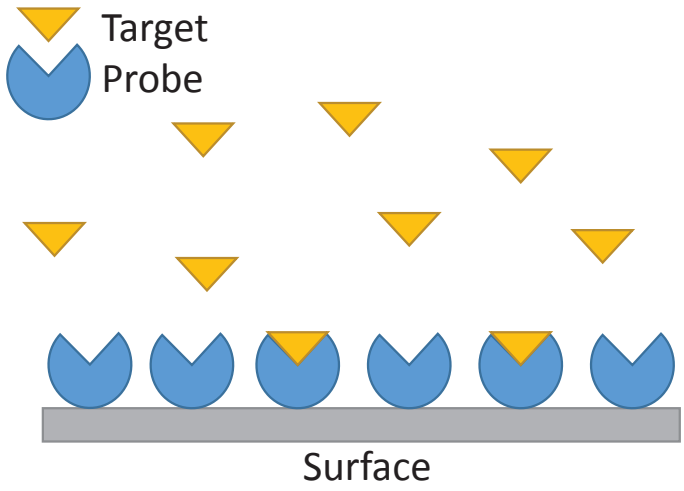

Figure 6.1: Schematic for sensing in a surface using a target-probe pair

An optimal SGFET biosensor is designed to be specific, meaning that it only gives a response when it detects a targeted biomolecule of interest. To achieve this, a common strategy is to functionalize the sensor surface with probe molecules that bind specifically to the target (see Figure 6.1). The remaining space between the probes is then backfilled with a molecule that minimizes the interaction of the solution with the surface (e.g. BSA or

PEG). The Curtis lab has demonstrated methodologies to attach probes to graphene tightly, but non-covalently in order to preserve the electronic properties of graphene [40], and others have followed with schemes to covalently bind the probes [69, 72]. While ultimately, we are capable of moving in the same direction of specific sensing, we found it critical to take a step back to investigate some fundamental questions about the mechanisms of sensing. For example, what is the effect of a protein interacting directly with graphene, like in the case of the anchored protein or even non-specifically? Do charged proteins that adhere to graphene dope the surface like any other impurity? What is the effect of oppositely charged proteins? Are there any considerations to be taken into account when backfilling with BSA or PEG? Here we aim to answer some of these questions in order to build a foundation to address more difficult problems like that of a target molecule anchored a few nanometers from the graphene surface by the probe molecule, possibly interacting but in a more complex manner. Indeed, exactly how the sensing would work in those scenarios is not clear at all. This study provides a first step in filling the gap to reach those goals.

Several mechanisms for biomolecular detection in SGFETs have been suggested [48]. For some small molecules -like DNA- the probe can be simply adsorbed to the graphene altering its conductivity by doping. For this case the target molecules -bound to the probes- also work as doping molecules [22, 16]. In order to achieve specific biosensing, other probe molecules can be attached to the surface using small linking molecules that are covalently bound to the probe at one end and, covalently or non-covalently, bound to graphene at the other end [15, 69, 40, 72]. Two sensing mechanisms have been suggested for this second type of probe attachment. When the probes are enzymes (i.e. biomolecular catalysts) that react with the target, they generate charges like electrons or protons that contribute to the carriers in the channel changing the value of its conductivity. In other cases the probe and target correspond to a ligand-receptor pair. These pair have steric and electrostatic complementarity that makes them specific to each other. For this case the mechanism for detection has been attributed to doping [61]. There are also two other mechanisms that can explain the conductivity sensitivity to charged biomolecules: change of the local electrostatic environment, that is a change in the local dielectric constant that modulates

the double layer thickness (Debye length λ_D) and charge screening, that is effectively an electrostatic gating effect [48].

In this chapter we will present results for protein adsorption. A few basic studies have been performed with non-specific adsorption of charged biomolecules on graphene SGFETs. Dong [22] and Chen [16] have performed experiments with DNA adsorption in CVD SGFETs. Dong used a silver (Ag) wire as the gate electrode and Chen used three types of wire: silver, graphite, and platinum (Pt). Ohno [62, 60] performed adsorption experiments of bovine serum albumin (BSA) with an exfoliated graphene device. He used a reference electrode as the gate and he monitored the conductance at a fixed gate while changing the concentration of BSA. We conducted our experiments using a reference electrode to avoid protein interactions in the electrode wire. A few more studies have been performed (see Appendix B) using SGFETs as specific biosensors.

In order to get a clearer picture on the nature of adsorption of charged proteins on graphene we conducted experiments using small proteins with opposite charge and measured the conductance response to gate voltage. This will help our understanding of the doping mechanism for each molecule and its relationship to their respective charge. Additional information will be obtained from an estimation of the impurities similar to the one carried out in Section 5.4 at high carrier density.

6.2 Non-Specific Protein Adsorption to Graphene

For our experiments we used two oppositely charged proteins of similar size: histones (from calf thymus Type III-S, Sigma Aldrich) and bovine serum albumin (BSA, fraction V, Calbiochem). Both molecules are globular, charged at physiological pH, and very small. Histones have a positive charge and a radius $r \approx 3.2$ nm. BSA molecules have a negative charge and a radius $r \approx 4$ nm. For all experiments the proteins were dissolved in 10mM phosphate buffer (PB) at pH 7.0 where their respective charges are known.

6.2.1 Dirac Voltage Shift in EG and CVD Devices for Positively Charged Histone Solutions

Several devices were used to study the effect on the conductance of histone adsorption to graphene SGFETs. Histones were diluted in 10mM PB at pH 7.0 to concentrations in the range [1ng/mL, 1mg/mL] (corresponding to the range [65pM, 65mM]). Figure 6.2(a) shows the conductance versus V_g plots for all the histone concentrations for a given EG device. For these solutions $V_{g,min}$ shifts to the right (toward higher voltage) when the histone concentration increases. To get a clearer picture of this shift Figure 6.2(b) shows a plot of the sensitivity of $V_{g,min}$ to concentration. The observed shift of the Dirac point corresponds to p-doping, consistent with the expected adsorption of positive charge onto the graphene surface. For complete transparency in reporting, for 2 out of 8 histone experiments, the Dirac point shift was in the opposite direction of that expected (see Figure C.3 and Table 6.1). We suspect that these arose due to faulty devices and other issues. However, ideally a few more devices would be tested before we can absolutely eliminate some other possibility.

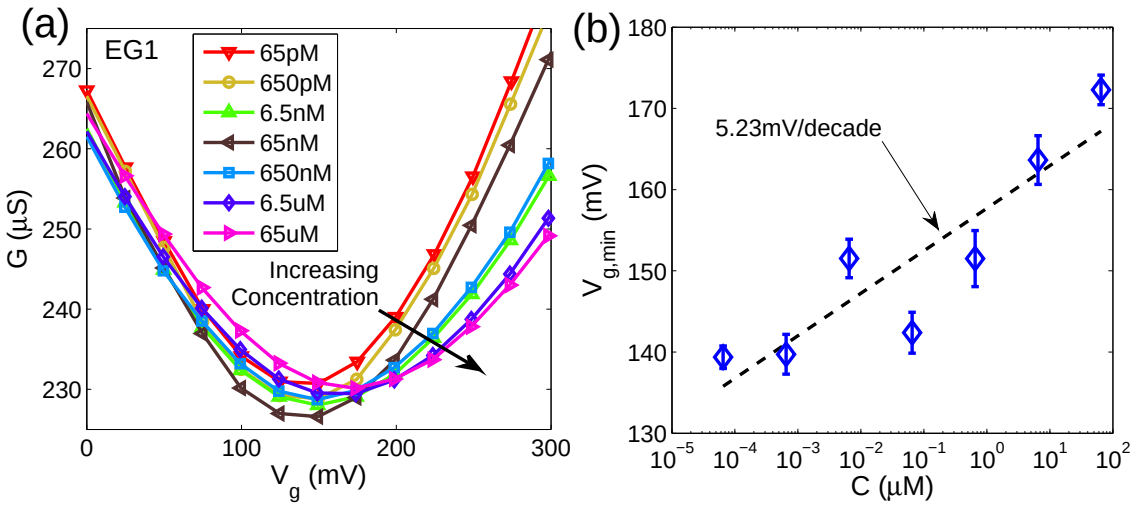

Figure 6.2: (a) Conductance versus V_g at several histone concentrations in an EG sample, (b) Dirac voltages versus histone concentration for the plots in (a)

The results for the same experiment for other CVD and EG devices are similar. In Figure 6.3 (EG devices) and Figure 6.4 (CVD devices) the same plots shown in Figure 6.2 are shown for other devices. Table 6.1 shows semi-logarithmic fitted values for the sensitivity for the Dirac voltage shifts shown in Figures 6.3 and 6.4. For all of the devices we find that

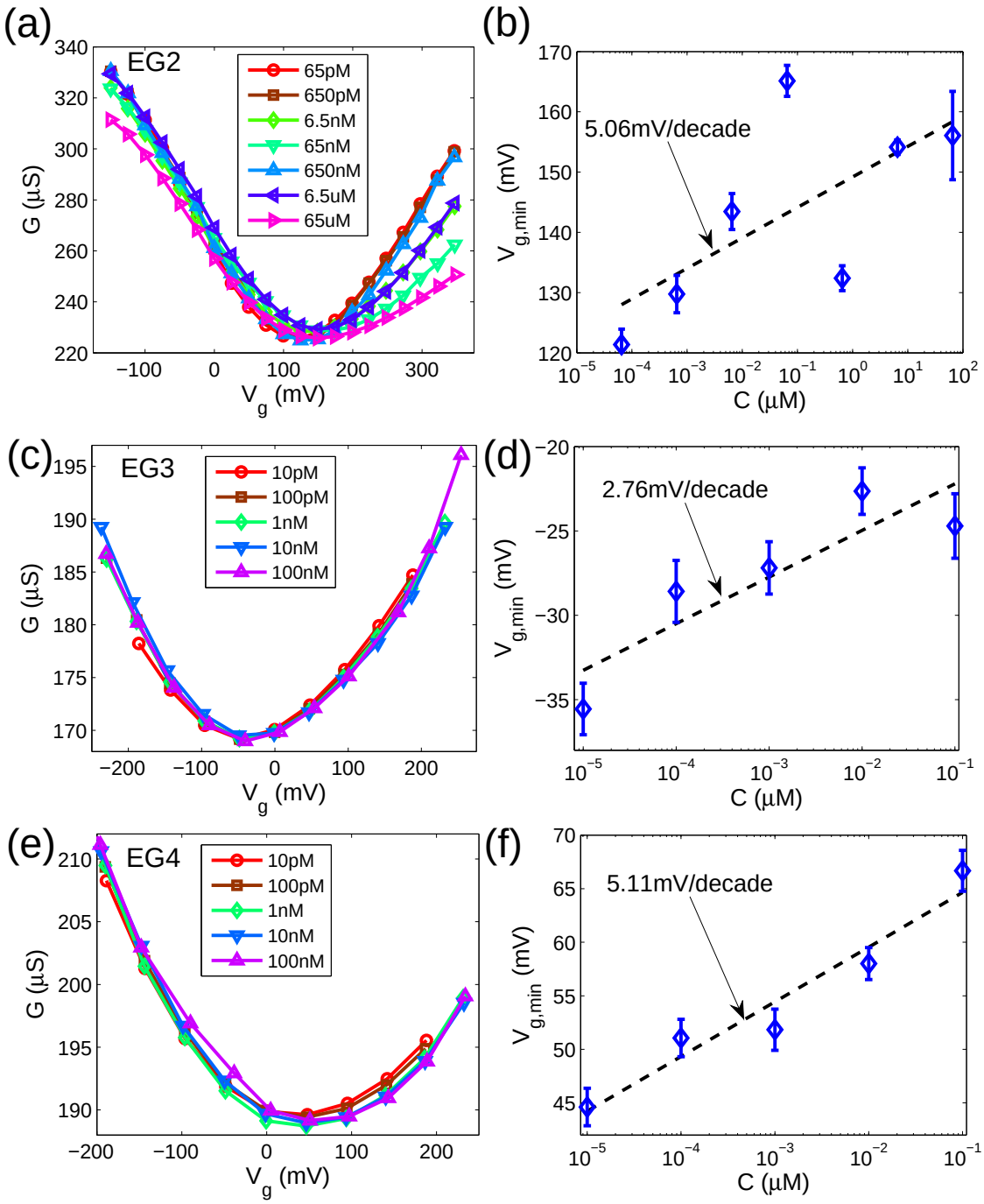

Figure 6.3: (a,c,e) Conductance versus V_g at several histone concentrations for three EG samples, (b,d,f) Dirac voltages versus histone concentration for the plots in (a,c,e). The slope of the curve is the sensitivity, which is between 2-5 mV/decade for histones interacting with EG SGFETs

the sensitivity is small compared to that measured for ionic sensing (see Chapter 4), and as we will see later, compared to BSA. The average sensitivity for histones is $< S_{hist} > = 3.94$

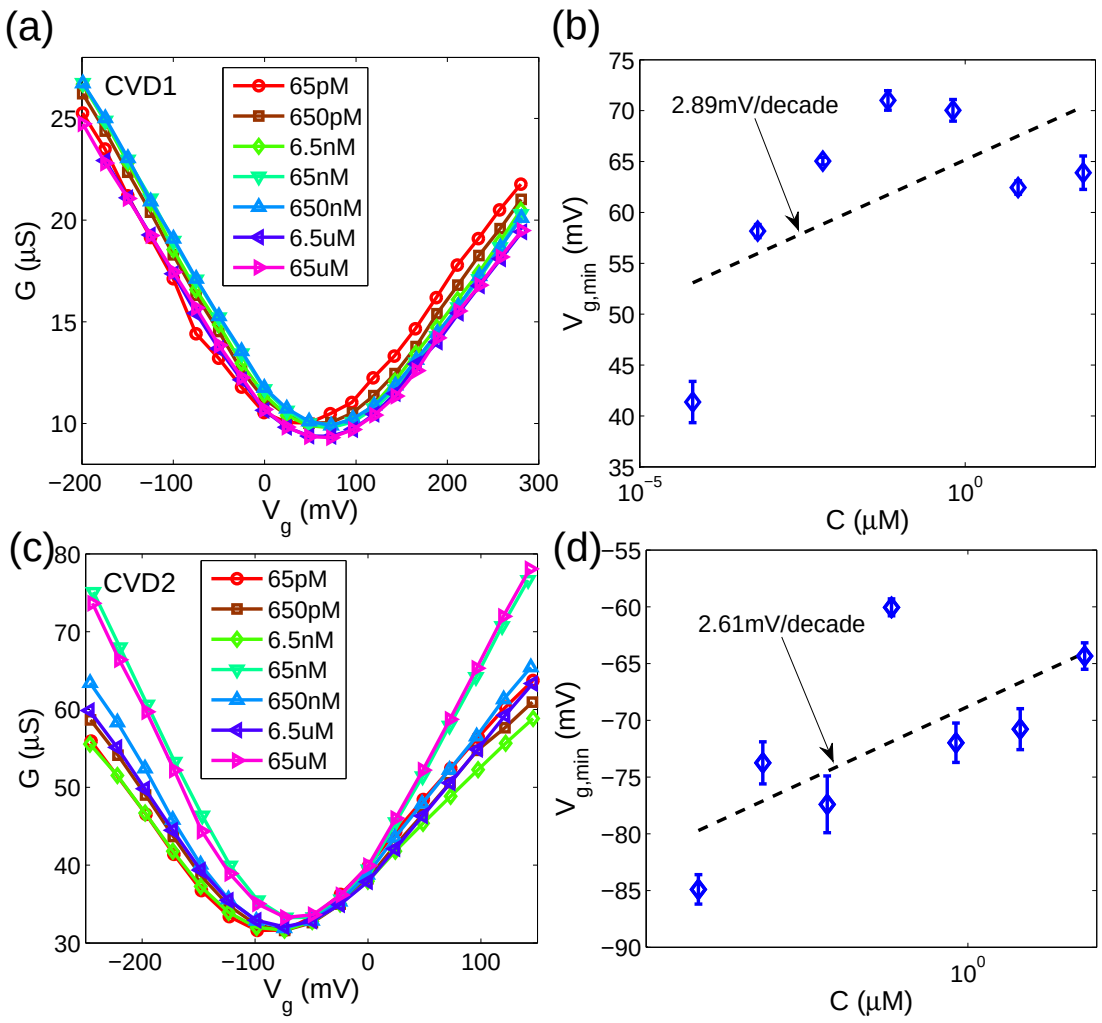

Figure 6.4: (a,c) Conductance versus V_g at several histone concentrations for two CVD samples, (b,d) Dirac voltages versus histone concentration for the plots in (a,c). The slope of the curve is the sensitivity, which is around 2 mV/decade for histones interacting with CVD SGFETs

mV/decade compared with $< S_{IS} >$ = -33.8 mV/decade for ionic sensing and $< S_{BSA} >$ = -43.6 mV/decade for BSA. This suggests that the interaction of the highly charged histone proteins with the graphene is for some reason, incapable of achieving a strong doping effect needed to achieve a high sensitivity. This will have an effect on the magnitude of the change of the conductance for a change in histone concentration with a fixed gate voltage as will be seen in Section 6.2.4.

Table 6.1: Sensitivity of the Dirac voltage to the histone concentration for the samples in Figures 6.3 and 6.4

Sample	Sensitivity (mV/decade)
CVD1	2.89
CVD2	2.61
CVD3	-5.75
EG1	5.23
EG2	5.06
EG3	2.76
EG4	5.11
EG5	-12.54

6.2.2 Dirac Voltage Shift in EG Devices for Negatively Charged BSA Solutions

BSA is negatively charged at pH 7 and, therefore, it is expected that it will have an n-doping effect when adsorbed into graphene. BSA solutions in the range [40ng/mL, 400μg/mL] (corresponding to concentrations in the range [600pM, 6μM]) were prepared in 10 mM PB at pH 7. Figure 6.5 shows the conductance versus V_g plots and the shift in $V_{g,min}$ with BSA concentration for a device. The observed shift in $V_{g,min}$ is consistent with our interpretation of the doping effect. The sensitivity is higher for this case and similar to the sensitivity for ionic sensing. This suggests that distribution of the surface charge of BSA facilitates the doping of graphene. A higher change in conductance at a fixed gate is also expected (see Figure C.2). The shape of the conductance curves changes more than for the case of ionic sensing or histone adsorption. We had almost identical effects with another device in the same wafer (see Figure C.1). These results require confirmation using additional devices.

6.2.3 Estimation of Impurities from the High Carrier Density Conductance

Using the same method introduced in Section 5.4, we estimated the impurities using the conductance versus V_g curves for all the histone concentrations from the data in Figure 6.2 (EG device). This method relies on the conductance dependence on the carrier density. The conductance versus carrier density plots are shown in Figure 6.6. The data where the carrier density is either dominated by holes (h-side) or electrons (e-side) was used to perform the

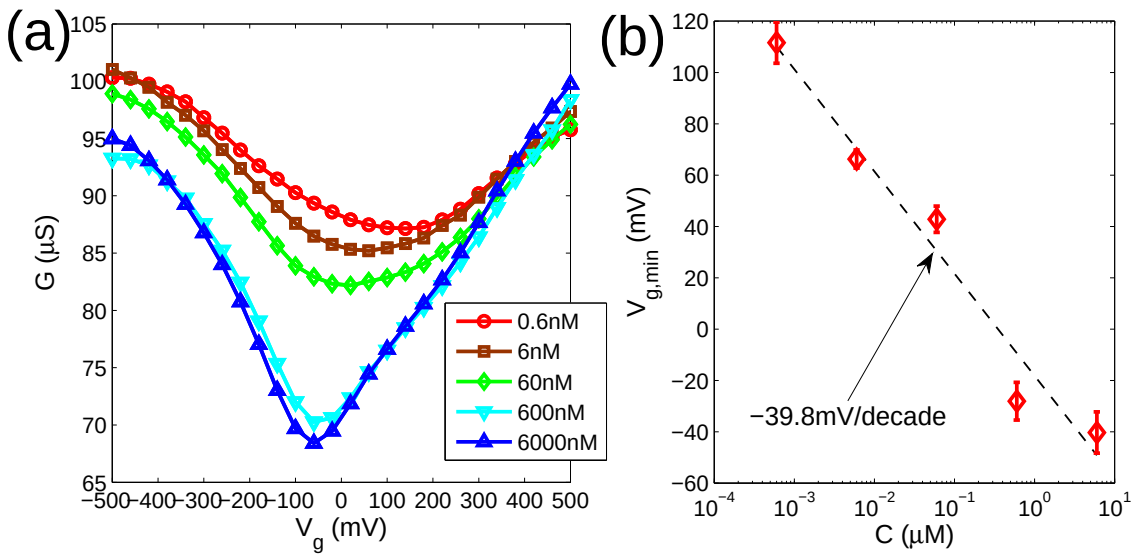

Figure 6.5: (a) Conductance versus V_g for several BSA concentrations (b) Dirac voltage for data in (a)

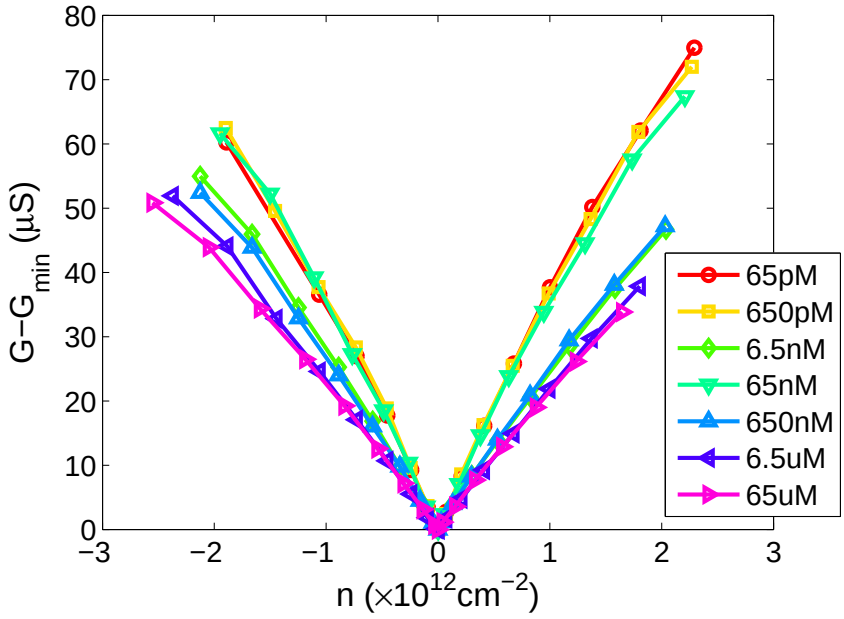

Figure 6.6: Conductance versus carrier density plots obtained from the data in Figure 6.2(b).

estimation of the impurities. The results from these estimations are shown in Figure 6.7(a) and Table 6.2 for every protein concentration. A glance at Figure 6.7(a) and Figure 6.2(b) suggest a relationship between the impurities and the Dirac point shift that is expected for dopants [1]. To get a second look on this we plot n_{imp} versus $V_{g,min}$ in Figure 6.7(b). In

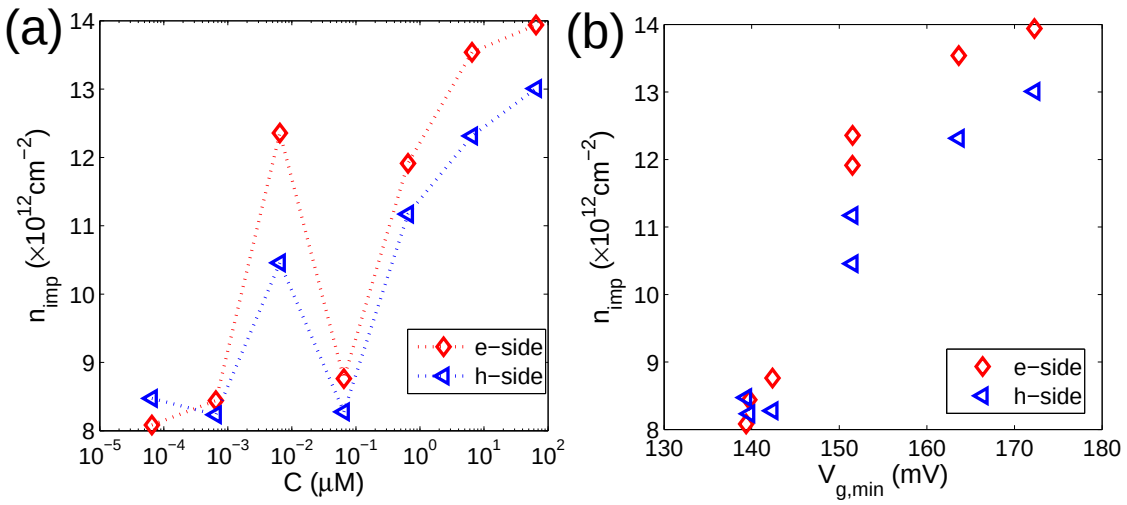

Figure 6.7: (a) Impurities calculated from conductance at high carrier density versus histone concentration (b) Impurities calculated from conductance at high carrier density versus $V_{g,min}$

this case, as in the case for ionic sensing, there seems to be an effect of the charge on the conductivity. The histones adsorbed to the surface seem to behave as charged impurities that participate in the scattering of carriers.

Table 6.2: Dirac voltages and impurities estimated using the data in Figure 6.7

Histone Conc.	$V_{g,min}$	n_{imp} e-side ($\times 10^{12}$cm^{-2})	n_{imp} h-side ($\times 10^{12}$cm^{-2})
65 pM	139.4	8.08	8.47
650 pM	139.7	8.44	8.23
6.5 nM	151.5	12.36	10.46
65 nM	142.4	8.76	8.28
650 nM	151.5	11.91	11.17
6.5 μM	163.6	13.54	12.32
65 μM	172.3	13.94	13.01

6.2.4 Time Dependent Conductance Change in a Histone Experiment

As in Section 4.3.2 experiments keeping the gate voltage at a fixed value while changing the concentration of histones were performed with an EG SGFET. Figure 6.8(a) shows the conductance versus time behavior of an SGFET with histone concentrations in the range [50pM-500nM]. The Dirac voltages where below zero volts for that particular device so the

decrease in conductance was expected as the sample acquired acceptors and $V_{g,min}$ shifts to the right. The change in the conductance when the gate potential is changed is similar to the change observed in KCl solutions. Therefore, the small change of the conductance with increasing histone concentration (-0.3 μS/decade, see Figure 6.8) is expected because of the smaller sensitivity of the Dirac voltage to the concentration.

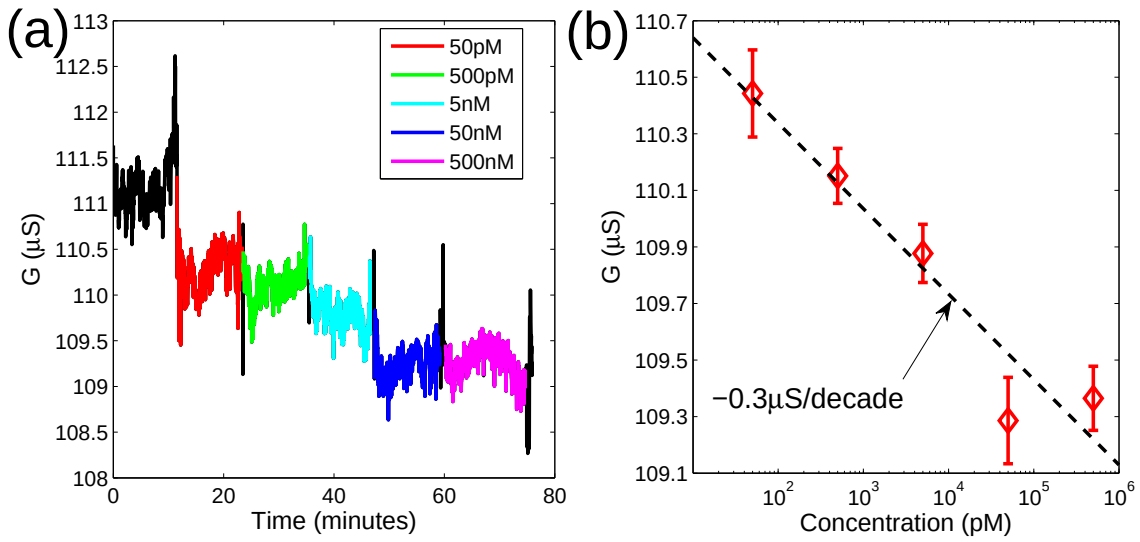

Figure 6.8: (a) Time evolution for the conductance with changing histone concentrations at a fixed gate voltage ($V_g = 0V$) (b) Device conductance for several histone concentrations at a fixed gate voltage ($V_g = 0V$)

6.3 Conclusions

The experimental results shown in this chapter indicate that the adsorption of charged biomolecules to graphene have an effect in the Dirac voltage and in the conductance that can be attributed to having an interaction with the graphene as charged impurities. The doping type is dependent on the charge polarity of the molecule and this effect is also consistent with the assumption of their impurities-like interaction with the graphene channel. For the histones we also estimated the impurities from the experimental data. This estimated densities were also dependent on the histone concentration confirming their role as charged impurities.

The sensitivity of the Dirac voltage of graphene to BSA is higher than its sensitivity to histones. BSA also has a higher effect on the shape of the conductance versus V_g plots that

may be related to this higher sensitivity. In contrast, we achieved a lower detection limit for histones (10 pM) with a dynamic range of six decades. For BSA the limit was 600pM with four decades of dynamic range. These values are in the range of the best values achieved so far with graphene SGFETs [41] (and Appendix B).

In future experiments with specific sensing, where the charges are farther away from the graphene surface, the role of charged probes and targets as donors or acceptors can be quantified using the estimation of impurities from the conductance response to the gate. The design of receptors for specific sensing that do not require charged targets (or where their charge does not matter) is possible with engineering on how the charge that the receptor presents to the graphene channel changes with the analyte concentration.

CHAPTER VII

CONCLUSIONS AND OUTLOOK

We performed experiments to characterize the electrical response of EG and CVD SGFETs to changes in the ionic strength in KCl aqueous solutions and to adsorption of charged proteins. Our analysis of the ionic strength response of these devices indicates that the groups close to the graphene surface which a variable charge play a similar role than permanent charged impurities. The shift of the Dirac point ($V_{g,min}$), the change of the ionizable charge, and the estimated impurities for several ionic concentrations are consistent with this picture. The proteins adsorbed to the surface also show a relation between protein concentration, the shift of the Dirac point, and the estimated density of impurities. Therefore, it is apparent that the mechanism of interaction for molecules close to the graphene plane is the scattering of carriers in the graphene by the charged particles.

This deeper understanding of the physics of ionic sensing in liquids can be leveraged for the design of specific sensors. Controlled application of impurities, and in particular ionizable impurities for the case of ionic solutions, can be used to calibrate the sensitivity of the device. To minimize the leakage current additional n-doping can be useful to displace the Dirac voltage to negative values where the leakage is smaller. Another avenue to make new sensors based on graphene is the design of probes with electrostatic properties that change after binding a neutral target species. If the value of the charge that the probe presents to the graphene is dependent of the target, there will be a change in the conductance of the device making it sensitive to the target itself. This approach also works for charged targets when their charge is not strong enough to have a clear influence in the channel conductance.

In future specific sensing experiments, where the charges may be farther away from the graphene plane, the same data analysis performed here can be used to discern the mechanism of detection. The analysis framework used in this work can be improved by multiphysics simulations now that we have established its usefulness.

The long term goal of achieving ultra low detection limits in electronic sensors based on graphene will be conquered by a careful consideration of what type of charge and in what amount is needed to modulate the conductance of the channel above the noise level. Our work provides a framework that can be useful to plan and analyze future experiments on graphene SGFETs.

APPENDIX A

PH SENSING WITH SGFETS

In pH measurement experiments two main strategies are used to adjust the pH values. One way to change the pH is to start with a regular buffer solution of known pH and add a strong acid (HCl) or a strong base (KOH, NaOH) to change the pH of the buffer. Another way to obtain solutions of several pH values is to start with buffers at their standard pH values and mix them to get solutions at pH values in between the original ones. The most common used buffers are: 10mM phosphate buffer (pH 7.0-7.5), 10mM phthalate buffer (pH 4.0), and borate buffer (pH 9.3).

To characterize the devices as pH sensors the conductivity of the graphene channel in an SGFET is measured for different gate voltages with different pH solutions. As described in Chapter 4 and Section 2.4, the conductivity of graphene has a minimum value at the Dirac Point where the carriers are in electron and hole puddles [1] induced by the charged impurities. Then when the gate potential is increased the conductivity rises as electrons carriers are induced and when the gate is decreased hole carriers are dominant and the conductivity rises too. This behavior is observed both in solid and in liquid gating.

In the majority of experiments a different gate voltage is required to reach the minimum conductance point (MCP) and the conductivity versus V_g curves shift to the right with increasing pH value. An example of this can be observed in Figure A.1. The inset shows a plot of the gate potential at which the MCP is reached (called threshold voltage) versus pH value. This plot is fitted to a line to get the sensitivity for the threshold voltage to the pH, in this case the sensitivity is 98.8mV/pH. The sensitivities found by different groups are summarized in Table A.1.

Some of these experiments have explored the reversibility in the device conductance value after changing the pH value and returning it to a previous value.

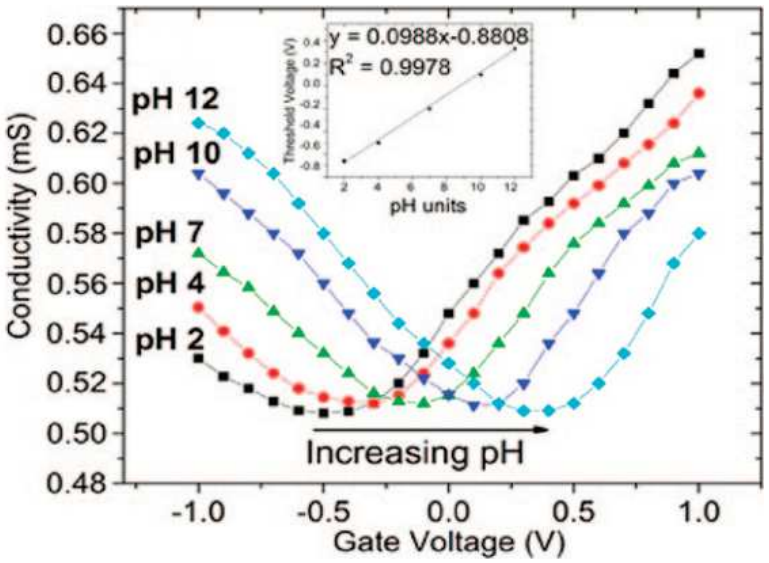

Figure A.1: Representative curve of Conductivity versus Gate Voltage for different pH solutions [2]. Reprinted with permission from (J. Am. Chem. Soc., vol. 130, no. 44, pp. 14392–14393, 2008). Copyright (2008) American Chemical Society).

Table A.1: Summary experimental results of pH sensing

Publication	Graphene source	pH range	Sensitivity (mV/pH)	V_{DS}(mV)
Ang2008 [2]	EG	2-12	97.8 (1-2 layers)	-1000
			98.8 (3-4 layers)	-1000
Ohno2009 [62]	Exfoliated	4-7.8	21.7	
Ristein2010 [65]	EG	3-12	19	-50
Cheng2010 [17]	Exfoliated	6-9	14.7	-50
Fu2011 [24]	CVD	5-10	6 (untreated)	10-50
			0 (organically passivated)	
			17 (inorganically passivated)	
Mailly-Giacchetti2011 [50]	CVD	4.3-7.5	24	50
Mailly-Giacchetti2013 [51]	CVD	4.3-8.11	22 (clean-on SiO_2)	50
		4.7-8.2	21 (with residues-on SiO_2)	50
		4.2-8.2	22 (on PEN)	50
		4.4-8.3	18 (on OTS)	50
Sohn2013 [67]	GO	6-9	29.2	100

APPENDIX B

BIOSENSING WITH SGFETS

Unfunctionalized graphene has been used as an electrical sensitive surface for the recording of cellular electrical activity. Cohen-Karni [18] recorded signals from cardiomyocytes for different gate voltages at both sides of the Dirac point (MCP). They found that the polarity of the measured signal was swapped when the carriers changed from electrons to holes and the maximum sensitivity was obtained 50mV tp 100mV apart from the MCP. Similar results were obtained by Hess [31] with cardiomyocyte-like cells (HL-1) where the gate potential was adjusted to the point of maximum trasconductance in order to maximize the sensitivity.

In other cases, the graphene channel in a graphene SGFET based biosensors is functionalized with a bioreceptor that is specific to the target biomolecule. These bioreceptors can be classified into four categories independently of the scheme used to bind them to graphene: DNA probes, antibodies, aptamers, and enzymes. DNA probes are specific to their complementary DNA (cDNA), antibodies and aptamers are specific in general to proteins, and enzymes can be specific to proteins and small molecules as well. It is also possible to use an antibody to give the sensor specificity for a single cell organism (E. Coli [34]). A summary of graphene SGFET based bioreceptors is shown in Table B.1.

As in the case of pH and ionic sensing there are two ways of characterizing the device: measurement of the conductivity for several gate voltages including the MCP and real-time measurements at a fixed gate while the biomolecule concentration is increased. For the case of biosensing it is usual to find a shift in the minimum conductivity as well as a shift of the threshold voltage (see Figure B.1). The buffer concentration also plays a role in the sensitivity. A lower concentration of the buffering ions increases the width of the double layer (see Chapter 4) and so a higher sensitivity is expected as found by Chen [16].

The real-time response for graphene SGFETs has been tested at a fixed gate while changing the analyte to be detected. The signal obtained is the source-drain current (I_{SD}).

Table B.1: Summary of graphene based SGFET biosensors

Publication	Graphene source	Functionalization scheme/Receptor class	Bioreceptor	Target
Dong2010[22]	CVD	Au-NP/DNA probe	DNA probe	cDNA (0.01nM-100nM)
Huang2010[35]	CVD	PYR-NHS/Enzyme	GOD[1], GluD[2]	Glucose (0.1mM-10mM), glutamate (5μM-0.4mM)
Stine2010[69]	RGO	EDA linker/DNA probe	DNA probe	cDNA (10nM-1μM)
Ohno2010-11[61, 59]	Exfoliated	PYR-NHS/Aptamer	IgE[5] Aptamer	IgE (0.29nM-340nM)
Mao2011[52]	RGO	Au-NP/Ab	Anti-IgG[4]	IgG (0.2ng/mL-0.2mg/mL)
Huang2011[34]	CVD	PYR-NHS/Ab	Anti-E. Coli	E. Coli (10cfu/mL-10^6cfu/mL)
Kwak2012[42]	CVD	PYR-NHS/Enzyme	GOD	Glucose (0.1mM-10.9mM)
Chen2013[16]	CVD	DNA probe adsorption	DNA probe	cDNA (1pM-100nM)
Kim2013[37]	RGO Network	PYR-NHS/Ab	Anti-PSA[3]	PSA-ACT complex (100fg/mL-1μg/mL)
Ohno2013[63]	Exfoliated	PYR-NHS/DNA probe	DNA probe	cDNA (200nM)
Sohn2013[67]	RGO Network	PYR-NHS/Enzyme	Acetylcholine esterase	Acetylcholine (0.10mM-10mM)
Tehrani2014[72]	EG	Diazotization/Ab	anti-8OHdG[6]	8OHdG (0.01-40ng/mL)

In general the time response of the biosensors shows some erratic behavior before reaching a steady state value (see Figure B.2 [35]) or the signal is still not clearly stable after some reasonable time, but with a clear change after increasing the analyte concentration (see Figure B.3 [61]). After the signal is stable enough the final value averaged over some

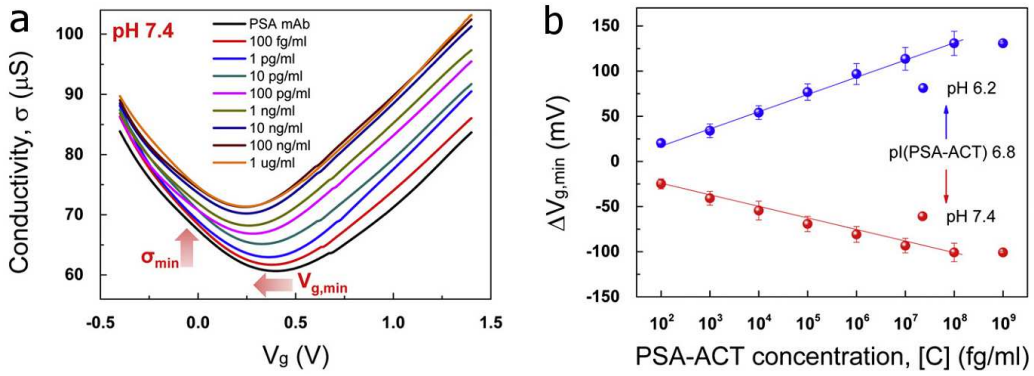

Figure B.1: Detection characteristics of R-GO FET immunosensors. (a) ??Vg plot of R-GO FET at a V_{sd} of 0.6 V with various concentrations of PSA-ACT complex in the analyte solutions at pH 7.4. (b) Shift in the minimum conductivity point ($\Delta V_{g,min}$) with the concentration of PSA-ACT complex in the pH 7.4 and pH 6.2 analyte solutions. The $\Delta V_{g,min}$ value was obtained by calculating the difference in $V_{g,min}$ as a reference for the device with no binding of PSA-ACT complex [37]. Adapted with permission from (Biosens. Bioelectron., vol. 41, pp. 621–6, Mar. 2013. Copyright (2013) Elsevier).

time window can be obtained and a plot of change in current versus analyte concentration (see Figure B.3(b)) can be used to estimate the dissociation constant (K_D) using the Langmuir adsorption isotherm given by,

$$\Delta I_D = \frac{\Delta I_{D,max} C}{K_D + C} \tag{B.1}$$

where ΔI_D is the change in current for a given concentration C and $\Delta I_{D,max}$ is the change in current at the saturation point.

[1]Glucose oxidase
[2]Glutamate dehydrogenase
[3]Prostate specific antigen
[4]Immunoglobulin G
[5]Immunoglobulin E
[6]8 hydroxyguanosine

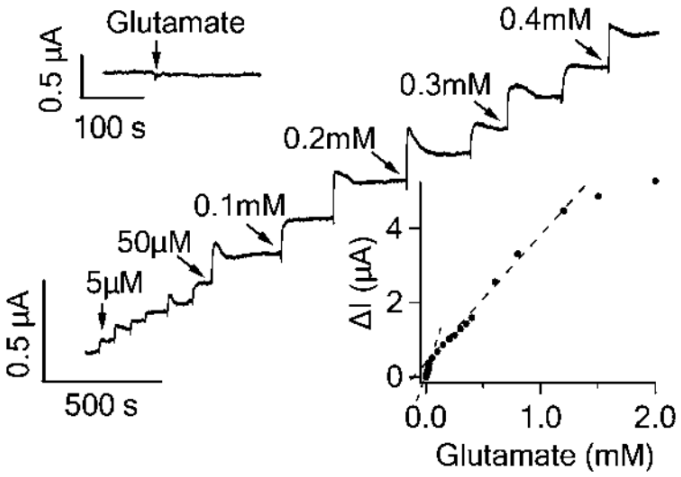

Figure B.2: Current responses of GluD functionalized graphene FET to the addition of glutamate to various concentrations. The upper inset shows that GluD free graphene FET is not responsive to 1 mM glutamate. The lower inset shows the response curve of the graphene FET to glutamate with two fitting lines indicating the two linear response regions [35]. Adapted with permission from (Nanoscale, vol. 2, pp. 1485–8, Aug. 2010. Copyright (2010) RSC Publishing).

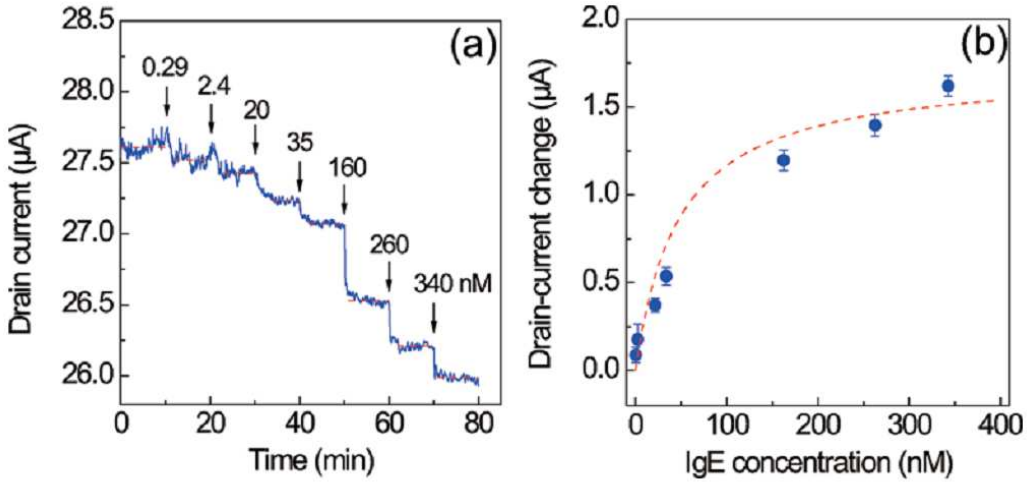

Figure B.3: (a) Time course of I_D for an aptamer-modified SG-FET. At 10 min intervals, various concentrations of IgE were injected. (b) Change in drain current versus IgE concentration. The red dashed curve shows a fit to the Langmuir adsorption isotherm with K_D = 47 nM [61]. Adapted with permission from (J. Am. Chem. Soc., vol. 132, pp. 18012–3, Dec. 2010. Copyright (2010) American Chemical Society).

APPENDIX C

ADDITIONAL INFORMATION

C.1 Additional Information for Section 6.2.2

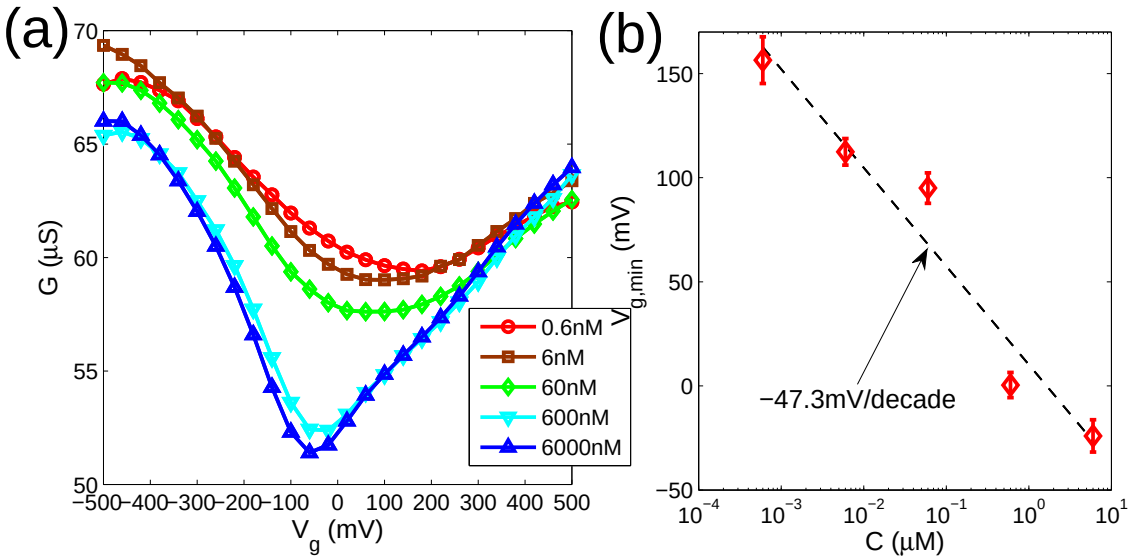

Figure C.1: (a) Conductance versus V_g for several BSA concentrations for another device (b) Dirac voltage for data in (a)

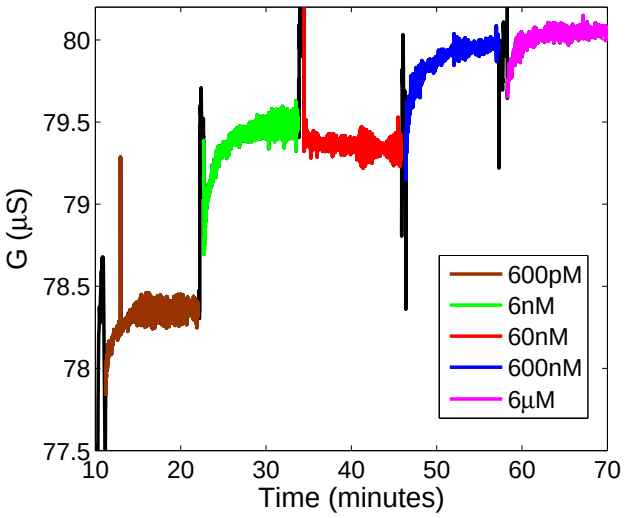

Figure C.2: Conductance time evolution with changing BSA concentration

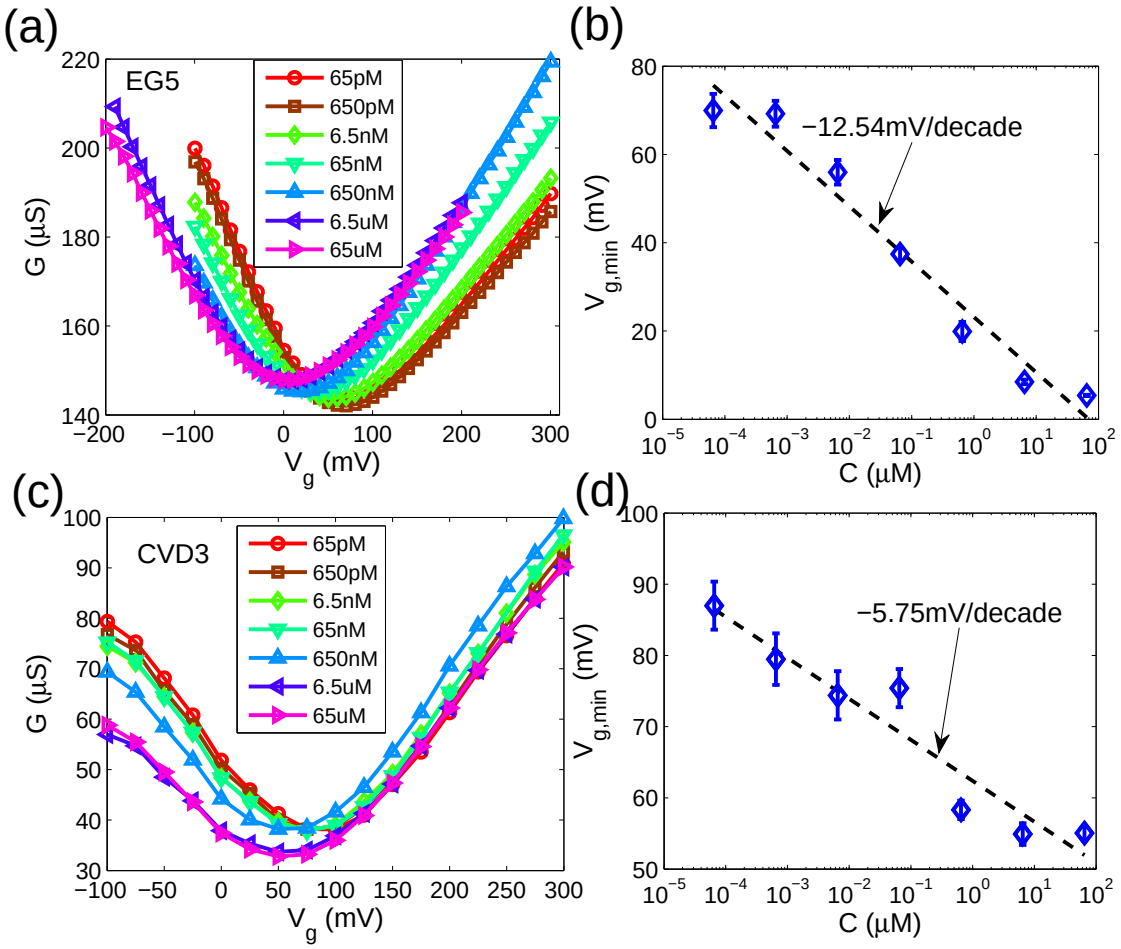

Figure C.3: (a,c) Conductance versus V_g at several histone concentrations for two samples, (b,d) Dirac voltages versus histone concentration for the plots in (a,c,e)

REFERENCES

[1] Adam, S., Hwang, E. H., Galitski, V. M., and Das Sarma, S., "A self-consistent theory for graphene transport.," *Proc. Natl. Acad. Sci. U. S. A.*, 2007.

[2] Ang, P. K., Chen, W., Wee, A. T. S., and Loh, K. P., "Solution-Gated Epitaxial Graphene as pH Sensor," *J. Am. Chem. Soc.*, 2008.

[3] Avouris, P. and Dimitrakopoulos, C., "Graphene: Synthesis and applications," *Mater. Today*, 2012.

[4] Back, J. H. and Shim, M., "pH-dependent electron-transport properties of carbon nanotubes.," *J. Phys. Chem. B*, 2006.

[5] Bae, S., Kim, H., Lee, Y., Xu, X., Park, J.-S., Zheng, Y., Balakrishnan, J., Lei, T., Kim, H. R., Song, Y. I., Kim, Y.-J., Kim, K. S., Ozyilmaz, B., Ahn, J.-H., Hong, B. H., and Iijima, S., "Roll-to-roll production of 30-inch graphene films for transparent electrodes.," *Nat. Nanotechnol.*, 2010.

[6] Behrens, S. H. and Grier, D. G., "The charge of glass and silica surfaces," *J. Chem. Phys.*, 2001.

[7] Berger, C., Song, Z., Li, T., Li, X., Ogbazghi, A. Y., Feng, R., Dai, Z., Alexei, N., Conrad, M. E. H., First, P. N., and De Heer, W. a., "Ultrathin epitaxial graphite: 2D electron gas properties and a route toward graphene-based nanoelectronics," *J. Phys. Chem. B*, 2004.

[8] Berger, C., Song, Z., Li, X., Wu, X., Brown, N., Naud, C., Mayou, D., Li, T., Hass, J., Marchenkov, A. N., Conrad, E. H., First, P. N., and de Heer, W. a., "Electronic confinement and coherence in patterned epitaxial graphene.," *Science*, 2006.

[9] Bolotin, K. I., Sikes, K. J., Jiang, Z., Klima, M., Fudenberg, G., Hone, J., Kim, P., and Stormer, H. L., "Ultrahigh electron mobility in suspended graphene," *Solid State Commun.*, 2008.

[10] Castro Neto, a. H., Guinea, F., Peres, N. M. R., Novoselov, K. S., and Geim, a. K., "The electronic properties of graphene," *Rev. Mod. Phys.*, 2009.

[11] Che, G., Che, G., Lakshmi, B. B., Lakshmi, B. B., Martin, C. R., Martin, C. R., Fisher, E. R., Fisher, E. R., Ruoff, R. S., and Ruoff, R. S., "Chemical Vapor Deposition Based Synthesis of Carbon Nanotubes and Nanofibers Using a Template Method," *Carbon Nanotub.*, 1998.

[12] Chen, F., Qing, Q., Xia, J., Li, J., and Tao, N., "Electrochemical Gate-Controlled Charge Transport in Graphene in Ionic Liquid and Aqueous Solution," *J. Am. Chem. Soc.*, 2009.

[13] Chen, F., Xia, J., Ferry, D. K., and Tao, N., "Dielectric Screening Enhanced Performance in Graphene FET," *Nano Lett.*, 2009.

[14] Chen, J.-H., Jang, C., Adam, S., Fuhrer, M. S., Williams, E. D., and Ishigami, M., "Charged-impurity scattering in graphene," *Nat. Phys.*, 2008.

[15] Chen, R. J., Bangsaruntip, S., Drouvalakis, K. A., Wong Shi Kam, N., Shim, M., Li, Y., Kim, W., Utz, P. J., and Dai, H., "Noncovalent functionalization of carbon nanotubes for highly specific electronic biosensors," *Proc. Natl. Acad. Sci. U. S. A.*, 2003.

[16] Chen, T.-Y., Loan, P. T. K., Hsu, C.-L., Lee, Y.-H., Tse-Wei Wang, J., Wei, K.-H., Lin, C.-T., and Li, L.-J., "Label-free detection of DNA hybridization using transistors based on CVD grown graphene.," *Biosens. Bioelectron.*, 2013.

[17] Cheng, Z., Li, Q., Li, Z., Zhou, Q., and Fang, Y., "Suspended graphene sensors with improved signal and reduced noise.," *Nano Lett.*, 2010.

[18] Cohen-Karni, T., Qing, Q., Li, Q., Fang, Y., and Lieber, C. M., "Graphene and nanowire transistors for cellular interfaces and electrical recording.," *Nano Lett.*, 2010.

[19] Das, Pisana, Chakraborty, Piscanec, Saha, Waghmare, Novoselov, Krishnamurthy, Geim, Ferrari, and Sood, "Monitoring dopants by Raman scattering in an electrochemically top-gated graphene transistor," *Nat Nano*, 2008.

[20] de Heer, W. a., Berger, C., Ruan, M., Sprinkle, M., Li, X., Hu, Y., Zhang, B., Hankinson, J., and Conrad, E., "Large area and structured epitaxial graphene produced by confinement controlled sublimation of silicon carbide.," *Proc. Natl. Acad. Sci. U. S. A.*, 2011.

[21] de Heer, W. a., Berger, C., Wu, X., First, P. N., Conrad, E. H., Li, X., Li, T., Sprinkle, M., Hass, J., Sadowski, M. L., Potemski, M., and Martinez, G., "Epitaxial graphene," *Solid State Commun.*, 2007.

[22] Dong, X., Shi, Y., Huang, W., Chen, P., and Li, L.-J., "Electrical detection of DNA hybridization with single-base specificity using transistors based on CVD-grown graphene sheets.," *Adv. Mater.*, 2010.

[23] Emtsev, K. V., Bostwick, A., Horn, K., Jobst, J., Kellogg, G. L., Ley, L., McChesney, J. L., Ohta, T., Reshanov, S. a., Röhrl, J., Rotenberg, E., Schmid, A. K., Waldmann, D., Weber, H. B., and Seyller, T., "Towards wafer-size graphene layers by atmospheric pressure graphitization of silicon carbide.," *Nat. Mater.*, 2009.

[24] Fu, W., Nef, C., Knopfmacher, O., Tarasov, A., Weiss, M., Calame, M., and Schönenberger, C., "Graphene transistors are insensitive to pH changes in solution.," *Nano Lett.*, 2011.

[25] Geim, A. K. and Kim, P., "Carbon wonderland.," *Sci. Am.*, 2008.

[26] Grundmann, M., *The Physics of Semiconductors*. 2010.

[27] Guo, X., "Surface plasmon resonance based biosensor technique: A review," *J. Biophotonics*, 2012.

[28] Hass, J., Varchon, F., Millán-Otoya, J. E., Sprinkle, M., Sharma, N., De Heer, W. a., Berger, C., First, P. N., Magaud, L., and Conrad, E. H., "Why multilayer graphene on 4H-SiC(0001) behaves like a single sheet of graphene," *Phys. Rev. Lett.*, 2008.

[29] Heller, I., Chatoor, S., Mannik, J., Zevenbergen, M. A. G., Dekker, C., and Lemay, S. G., "Influence of Electrolyte Composition on Liquid-Gated Carbon Nanotube and Graphene Transistors," *J. Am. Chem. Soc.*, 2010.

[30] Hernandez, Y., Nicolosi, V., Lotya, M., Blighe, F. M., Sun, Z., De, S., McGovern, I. T., Holland, B., Byrne, M., Gun'Ko, Y. K., Boland, J. J., Niraj, P., Duesberg, G., Krishnamurthy, S., Goodhue, R., Hutchison, J., Scardaci, V., Ferrari, A. C., and Coleman, J. N., "High-yield production of graphene by liquid-phase exfoliation of graphite.," *Nat. Nanotechnol.*, 2008.

[31] Hess, L. H., Jansen, M., Maybeck, V., Hauf, M. V., Seifert, M., Stutzmann, M., Sharp, I. D., Offenhäusser, A., and Garrido, J. a., "Graphene transistor arrays for recording action potentials from electrogenic cells.," *Adv. Mater.*, 2011.

[32] Hibino, H., Kageshima, H., and Nagase, M., "Epitaxial few-layer graphene: towards single crystal growth," *J. Phys. D. Appl. Phys.*, 2010.

[33] Hu, Y., Ruan, M., Guo, Z., Dong, R., Palmer, J., Hankinson, J., Berger, C., and Heer, W. a. D., "Structured epitaxial graphene: growth and properties," *J. Phys. D. Appl. Phys.*, 2012.

[34] Huang, Y., Dong, X., Liu, Y., Li, L.-J., and Chen, P., "Graphene-based biosensors for detection of bacteria and their metabolic activities," *J. Mater. Chem.*, 2011.

[35] Huang, Y., Dong, X., Shi, Y., Li, C. M., Li, L.-J., and Chen, P., "Nanoelectronic biosensors based on CVD grown graphene.," *Nanoscale*, 2010.

[36] Katsnelson, M. I., Novoselov, K. S., and Geim, a. K., "Chiral tunnelling and the Klein paradox ingraphene," *Nat. Phys.*, 2006.

[37] Kim, D.-J., Sohn, I. Y., Jung, J.-H., Yoon, O. J., Lee, N.-E., and Park, J.-S., "Reduced graphene oxide field-effect transistor for label-free femtomolar protein detection.," *Biosens. Bioelectron.*, 2013.

[38] Kim, D.-J., Sohn, I. Y., Jung, J.-H., Yoon, O. J., Lee, N.-E., and Park, J.-S., "Reduced graphene oxide field-effect transistor for label-free femtomolar protein detection.," *Biosens. Bioelectron.*, 2013.

[39] Kim, K. S., Zhao, Y., Jang, H., Lee, S. Y., Kim, J. M., Kim, K. S., Ahn, J.-H., Kim, P., Choi, J.-Y., and Hong, B. H., "Large-scale pattern growth of graphene films for stretchable transparent electrodes.," *Nature*, 2009.

[40] Kodali, V. K., Scrimgeour, J., Kim, S., Hankinson, J. H., Carroll, K. M., de Heer, W. a., Berger, C., and Curtis, J. E., "Nonperturbative chemical modification of graphene for protein micropatterning.," *Langmuir*, 2011.

[41] Kuila, T., Bose, S., Khanra, P., Mishra, A. K., Kim, N. H., and Lee, J. H., "Recent advances in graphene-based biosensors.," *Biosens. Bioelectron.*, 2011.

[42] Kwak, Y. H., Choi, D. S., Kim, Y. N., Kim, H., Yoon, D. H., Ahn, S.-S., Yang, J.-W., Yang, W. S., and Seo, S., "Flexible glucose sensor using CVD-grown graphene-based field effect transistor.," *Biosens. Bioelectron.*, 2012.

[43] Larrimore, L., Nad, S., Zhou, X., Abruña, H., and McEuen, P. L., "Probing electrostatic potentials in solution with carbon nanotube transistors.," *Nano Lett.*, 2006.

[44] Lee, C., Wei, X., Kysar, J. W., and Hone, J., "Measurement of the elastic properties and intrinsic strength of monolayer graphene.," *Science*, 2008.

[45] Li, X., Zhang, G., Bai, X., Sun, X., Wang, X., Wang, E., and Dai, H., "Highly conducting graphene sheets and Langmuir-Blodgett films.," *Nat. Nanotechnol.*, 2008.

[46] Li, X., Cai, W., An, J., Kim, S., Nah, J., Yang, D., Piner, R., Velamakanni, A., Jung, I., Tutuc, E., Banerjee, S. K., Colombo, L., and Ruoff, R. S., "Large-area synthesis of high-quality and uniform graphene films on copper foils.," *Science*, 2009.

[47] Liu, H., Liu, Y., and Zhu, D., "Chemical doping of graphene," *J. Mater. Chem.*, 2011.

[48] Liu, Y., Dong, X., and Chen, P., "Biological and chemical sensors based on graphene materials," *Chem. Soc. Rev.*, 2012.

[49] Mahan, G. D., *Condensed Matter in a Nutshell*. 2010.

[50] Mailly-Giacchetti, B., Hsu, A., Wang, H., Kim, K. K., Kong, J., and Palacios, T., "CVD-Grown Graphene Solution-gated Field Effect Transistors for pH Sensing," *MRS Proc.*, 2011.

[51] Mailly-Giacchetti, B., Hsu, A., Wang, H., Vinciguerra, V., Pappalardo, F., Occhipinti, L., Guidetti, E., Coffa, S., Kong, J., and Palacios, T., "pH sensing properties of graphene solution-gated field-effect transistors," *J. Appl. Phys.*, 2013.

[52] Mao, S., Yu, K., Lu, G., and Chen, J., "Highly sensitive protein sensor based on thermally-reduced graphene oxide field-effect transistor," *Nano Res.*, 2011.

[53] Minot, E. D., Janssens, A. M., Heller, I., Heering, H. A., Dekker, C., and Lemay, S. G., "Carbon nanotube biosensors: The critical role of the reference electrode," *Appl. Phys. Lett.*, 2007.

[54] Mo, Z., Wang, H., Liang, Y., Liu, F., and Xue, Y., "Highly reproducible hybridization assay of zeptomole DNA based on adsorption of nanoparticle-bioconjugate," *Analyst*, 2005.

[55] N'Diaye, A. T., Bleikamp, S., Feibelman, P. J., and Michely, T., "Two-dimensional Ir cluster lattice on a graphene moire on Ir(111)," *Phys. Rev. Lett.*, 2006.

[56] Nomura, K. and MacDonald, a. H., "Quantum Transport of Massless Dirac Fermions," *Phys. Rev. Lett.*, 2007.

[57] Novoselov, K. S., Geim, a. K., Morozov, S. V., Jiang, D., Zhang, Y., Dubonos, S. V., Grigorieva, I. V., and Firsov, a. a., "Electric field effect in atomically thin carbon films.," *Science*, 2004.

[58] Novoselov, K. S., Jiang, D., Schedin, F., Booth, T. J., Khotkevich, V. V., Morozov, S. V., and Geim, a. K., "Two-dimensional atomic crystals.," *Proc. Natl. Acad. Sci. U. S. A.*, 2005.

[59] Ohno, Y., Maehashi, K., Inoue, K., and Matsumoto, K., "Label-Free Aptamer-Based Immunoglobulin Sensors Using Graphene Field-Effect Transistors," *Jpn. J. Appl. Phys.*, 2011.

[60] Ohno, Y., Maehashi, K., and Matsumoto, K., "Chemical and biological sensing applications based on graphene field-effect transistors.," *Biosens. Bioelectron.*, 2010.

[61] Ohno, Y., Maehashi, K., and Matsumoto, K., "Label-free biosensors based on aptamer-modified graphene field-effect transistors.," *J. Am. Chem. Soc.*, 2010.

[62] Ohno, Y., Maehashi, K., Yamashiro, Y., and Matsumoto, K., "Electrolyte-Gated Graphene Field-Effect Transistors for Detecting pH and Protein Adsorption," *Nano Lett.*, 2009.

[63] Ohno, Y., Okamoto, S., Maehashi, K., and Matsumoto, K., "Direct electrical detection of DNA hybridization based on electrolyte-gated graphene field-effect transistor," *Jpn. J. Appl. Phys.*, 2013.

[64] Raza, H., *Graphene Nanoelectronics: Metrology, Synthesis, Properties and Applications*. 2012.

[65] Ristein, J., Zhang, W., Speck, F., Ostler, M., Ley, L., and Seyller, T., "Characteristics of solution gated field effect transistors on the basis of epitaxial graphene on silicon carbide," *J. Phys. D. Appl. Phys.*, 2010.

[66] Ruan, M., Hu, Y., Guo, Z., Dong, R., Palmer, J., Hankinson, J., Berger, C., and de Heer, W. a., "Epitaxial graphene on silicon carbide: Introduction to structured graphene," *MRS Bull.*, 2012.

[67] Sohn, I.-Y., Kim, D.-J., Jung, J.-H., Yoon, O. J., Thanh, T. N., Quang, T. T., and Lee, N.-E., "pH sensing characteristics and biosensing application of solution-gated reduced graphene oxide field-effect transistors.," *Biosens. Bioelectron.*, 2013.

[68] Stankovich, S., Piner, R. D., Chen, X., Wu, N., Nguyen, S. T., and Ruoff, R. S., "Stable aqueous dispersions of graphitic nanoplatelets via the reduction of exfoliated graphite oxide in the presence of poly(sodium 4-styrenesulfonate)," *J. Mater. Chem.*, 2006.

[69] Stine, R., Robinson, J. T., Sheehan, P. E., and Tamanaha, C. R., "Real-time DNA detection using reduced graphene oxide field effect transistors.," *Adv. Mater.*, 2010.

[70] Sutter, P. W., Flege, J.-I., and Sutter, E. a., "Epitaxial graphene on ruthenium.," *Nat. Mater.*, 2008.

[71] Tan, Y.-W., Zhang, Y., Bolotin, K., Zhao, Y., Adam, S., Hwang, E. H., Das Sarma, S., Stormer, H. L., and Kim, P., "Measurement of Scattering Rate and Minimum Conductivity in Graphene," *Phys. Rev. Lett.*, 2007.

[72] Tehrani, Z., Burwell, G., Azmi, M. a. M., Castaing, a., Rickman, R., Almarashi, J., Dunstan, P., Beigi, a. M., Doak, S. H., and Guy, O. J., "Generic epitaxial graphene biosensors for ultrasensitive detection of cancer risk biomarker," *2D Mater.*, 2014.

[73] Wallace, P. R., "The band theory of graphite," *Phys. Rev.*, 1947.

[74] William, S. H. J. and Offeman, R. E., "Preparation of Graphitic Oxide," *J. Am. Chem. Soc*, 1958.

[75] Wu, Z. S., Ren, W., Gao, L., Zhao, J., Chen, Z., Liu, B., Tang, D., Yu, B., Jiang, C., and Cheng, H. M., "Synthesis of graphene sheets with high electrical conductivity and good thermal stability by hydrogen arc discharge exfoliation," *ACS Nano*, 2009.

[76] Xu, X., Pereira, L. F. C., Wang, Y., Wu, J., Zhang, K., Zhao, X., Bae, S., Tinh Bui, C., Xie, R., Thong, J. T. L., Hong, B. H., Loh, K. P., Donadio, D., Li, B., and Özyilmaz, B., "Length-dependent thermal conductivity in suspended single-layer graphene.," *Nat. Commun.*, 2014.

VITA

Mauricio David Bedoya Saavedra was born in 1974 in Barranquilla, Colombia, where he grew up until finishing high school (Liceo de Cervantes '90). Then he lived in Bogotá, Colombia, where he went to college (Pontificia Universidad Javeriana, B.Sc. ECE, '97), and twice to grad school for serendipitous reasons (Universidad de los Andes, M.Sc. in CS '00 and Physics '04). He moved to Atlanta GA, in the fall of 2006 to start his doctorate in the School of Physics at Georgia Tech. His interests include, but are not limited to: technology, science, history, philosophy, cinema, languages, and literature. He spends a lot of time thinking about what can be done to make the human experience better in a world currently limited in growth by irrational fears, myopic views, and other traps of the mind. He also likes social dancing, playing soccer, volunteering, hiking, and most social events.

Men with traditional costumes in the *Carnaval de Barranquilla*